Development of a Female-based Musculoskeletal Model of the Lower Extremity

Y. Gouka

MSc. Mechanical Engineering

June 2025

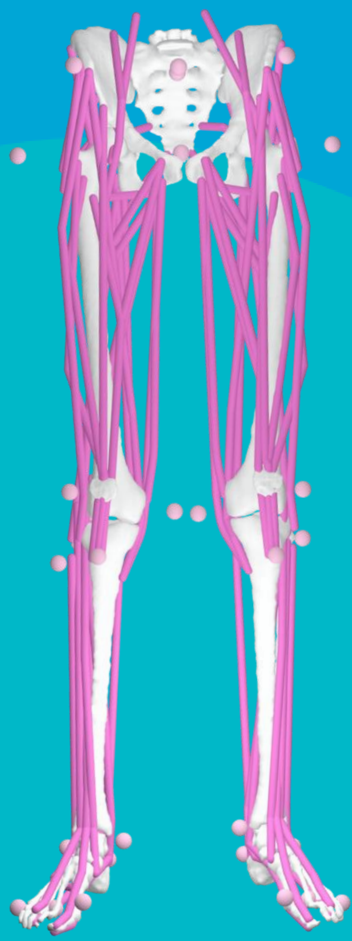

TU Delft

Development of a Female-based Musculoskeletal Model of the Lower Extremity

By

Y. Gouka

To obtain the degree of Master of Science

Mechanical Engineering

at the Delft University of Technology

Student number:	5177065
Committee members:	Dr. ir. E. van der Kruk (Chair)
	ir. J. Cueto Fernandez
	Prof. Dr. ir. F.C.T. van der Helm
Institution:	University of Technology, Delft
Faculty	Faculty of Mechanical Engineering (ME), Delft
Degree:	Master of Science in Mechanical Engineering
Track:	Biomechanical Design
Defense:	18 June 2025, 14:00-16:00u

Abstract - ***Background*** **Most widely used musculoskeletal models are predominantly based on male anatomy. This limits accurate biomechanical analysis in women, despite notable sex differences in occurrence of musculoskeletal pathologies.** ***Aim*** **This study aimed to develop a female musculoskeletal model of the lower extremity (YONI). The YONI is compared to the generic (male-based) model in simulation with a female participant.** ***Methods*** **The YONI model was developed in OpenSim Creator based on MR images. Comparisons were done between the YONI model and a scaled RAJAG model and a personalized model of using motion capture data in simulations.** ***Results*** **For comparison between YONI and RAJAG with another female subject, mean RMS error for the personalized model was 0.0096 m (SD = 0.0013), for the scaled RAJAG model 0.0247 m (SD = 0.0268) and for the scaled YONI model 0.0097 m (SD = 0.0010). Although SPM paired t-test showed significant differences for both YONI and RAJAG compared to the personalized model for all joint angles, the YONI model showed lower t-values compared to RAJAG. Joint moments reveal larger differences between YONI and scaled RAJAG models in the hip angles during the swing phase. Reserve moments were low in hip flexion and hip adduction, but higher in knee flexion and ankle flexion.** ***Conclusion*** **While observed kinematic and dynamic differences require cautious interpretation due to model limitations and data constraints, this work represents a crucial step toward the development of a female musculoskeletal model, essential for advancing biomechanical research and clinical applications for women.**

1. INTRODUCTION

The human musculoskeletal system plays a critical role in facilitating movement and providing support (Brotto & Bonewald, 2016; Peate, 2018; Valdez, 2019). A thorough understanding of this system is important for advancing fields such as biomechanics, rehabilitation and sport science (Anderson, 2020). A notable challenge within these domains is the presence of sex-based differences in musculoskeletal disorders. For example, Anterior Cruciate Ligament (ACL) injuries occur much more frequently in women compared to men (Bram et al., 2021; Griffin et al., 2006; Renstrom et al., 2008; Mancino et al., 2024).

To understand whether there are (bio)mechanic underlying causes due to sex differences in the anatomy, detailed information about internal muscle forces and joint dynamics in vivo is required, which remains a challenge. Although surface electromyography (EMG) can assess the excitations of superficial muscles (Savoji, Soleimani, & Moshayedi, 2024), it does not offer a direct measurement of actual muscle forces (Schwartz, 2012). Musculoskeletal modelling has emerged as a powerful tool for analyzing human movement, providing a non-invasive way to investigate joint dynamics and muscle forces during movement (Andersen, 2020; Maarleveld et al., 2024; Smith, Coppack, Van Den Bogert, Bennet, & Bull, 2021; Valente, 2013), which provides insights that are often inaccessible through traditional experimental research.

Currently, most widely used musculoskeletal models, including those implemented in the open-source software tool OpenSim 4.5 (Delp et al., 2007), are predominantly based on male anatomy (Abdullah, Hulleck, Katmah, Khalaf, & El-Rich, 2024; Delp et al., 1990; Firouzabadi, Arjmand, Pan, Zander & Schmidt, 2021; Maarleveld et al., 2024). For example, the *RajagopalLaiUhlrich2023* (RAJAG) is widely used within the OpenSim environment (Rajagopal et al., 2016, Lai, Arnold & Wakeling, 2017; Uhlrich, Jackson, Seth, Kolesar, & Delp, 2022). These models incorporate inertial parameters (segment masses and inertias), geometrical parameters (muscle paths) and muscle parameters. However, significant anatomical and physiological differences exist between men and women. For example, women generally have wider hips than men (Hewett et al., 2006), leading to a greater Q-angle, the angle between the line of force of the m. quadriceps and the patellar tendon (Brattström, 1964) and therefore influencing lower limb mechanics. Furthermore, (relative) muscle mass differs between sexes (Maarleveld et al., 2024; Smith & Smith, 2002; Smith & Mittendorfer, 2015). Muscle parameters such as Optimal Fiber Length (OFL), Tendon slack length, Pennation Angle at OFL (PA_{ofl}), and maximum isometric force ($F_{iso,max}$) are crucial for defining muscle behavior (Chen & Franklin, 2023; Lieber, 2010), but are difficult to determine (Chen, & Franklin, 2023; Manal, & Buchanan, 2004; Nam, & Uhm, 2011). Son et al. (2024) stated significant sex differences in OFL for various lower limb muscles. Linearly scaling is still implemented to determine these muscle parameters.

These factors suggest that, while current male-based generic models provide a fundamental understanding of human movement, their applicability to females might be limited. Therefore, it is impossible to answer the question if underlying (bio)mechanical factors causes differences in pathologies. Developing and validating a female musculoskeletal model that incorporates these sex-specific differences is therefore essential. Such models would provide researchers with a more accurate understanding of human movement in both sexes, paving the way for enhanced, sex-specific approaches in treatment planning, rehabilitation protocols, injury prevention strategies, and performance optimization.

Therefore, to understand the differences, this study aimed to (i) develop a female based lower extremity musculoskeletal model (YONI) based on magnetic resonance (MR) images and to (ii) compare the YONI model with the generic RAJAG model in simulations for female subject(s).

2. METHODS

2.1 Development of the model

The model was developed using the software OpenSim Creator (Kewley, Beesel & Seth, 2025), producing an OpenSim model that can be used within the OpenSim environment. Its development process consisted of three main steps: inertial parameters, geometric parameters and muscle parameters. An overview of the development of the model is presented in Figure I.

2.1.1 Experimental data

The available dataset, collected as part of a PhD project within the BODIESlab research group at TU Delft, consisted of MR images from nine young adult female subjects (age: 28.1 ± 2.6 years, height: 172.4 ± 4.3 cm, weight: 63.8 ± 5.7 kg, body fat percentage: 29.2 ± 4.8 %). Bone geometry meshes of the lower extremity and a skin surface mesh, segmented from the MR images, were available as STL files (Van de Meerakker, 2025).

In line with the development of the RAJAG model, one participant was selected for the development of the current model. This subject was carefully selected based on anthropometric characteristics (weight, height, and body fat percentage) that were representative of a predefined target population (Stein et al., 2024).

In addition to MR images, the dataset included motion capture data collected during static position and a sit-to-walk motion, which included marker positions and force plate data. This motion involved a structured sequence: the participant initiated from a seated position, performed a walking segment followed

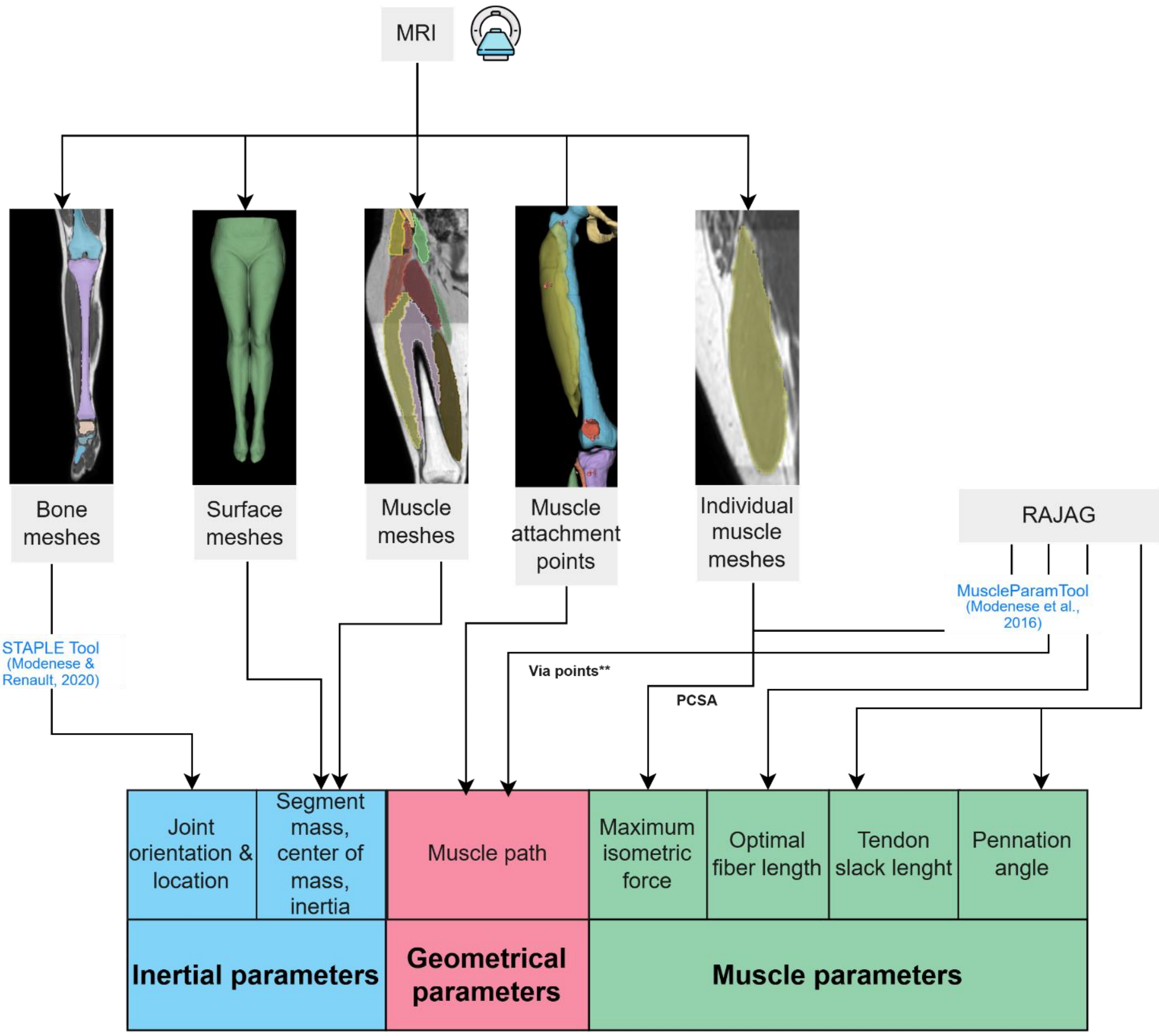

Figure I: Overview of methodology of the development of the model. **: Via points based on the scaled RAJAG model.

by a turn, then another walking segment, before returning to the seated position. This pattern was executed three times consecutively, starting and ending with a sit. Furthermore, a 3D scan was available which provided precise marker locations on the skin surface.

2.1.2 Inertial parameters

2.1.2.1 Skeletal model

The skeletal structure of the lower extremity was generated using the STAPLE toolbox, which is a set of MATLAB functions that create a subject-specific lower extremity model from bone geometry meshes (Modenese, & Renault, 2020). The bone geometry meshes required further processing to be compatible with STAPLE. The STAPLE toolbox was selected instead of manual methods to ensure minimal effort and computational time (Modenese, & Renault, 2020). Initially, separate models were generated for the left and right limbs and subsequently combined into a full skeletal model of the lower extremity. The sacrum geometry mesh was manually added to the pelvis body, establishing a rigid connection between sacrum and pelvis. The patella geometry meshes were manually added as independent bodies. The patellofemoral joint kinematics were adopted from a scaled RAJAG model, where values of the spline functions defining rotations and translations in these joints were adjusted to ensure accuracy within the current model. The RAJAG model was scaled to the subject's static marker data using the scaling tool of OpenSim.

2.1.2.2 Segment mass, Center of Mass and Inertia tensor

Segment-specific mass, center of mass (COM), and inertia tensors were computed directly from bone geometry meshes, the skin surface mesh and muscle meshes. This approach was preferred over using the function in STAPLE, to ensure subject specificity for the YONI model.

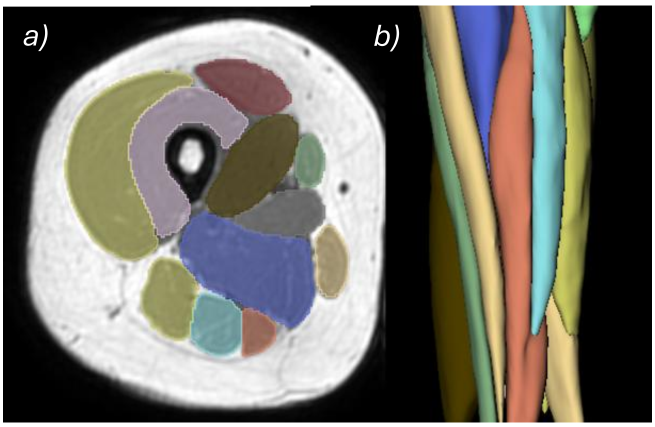

Figure II: Muscle segmentation using 3D slicer. *a)* Muscle segmentation of one MR image slice, with different colours representing different muscles. *b)* 3D reconstruction of the segmented muscles.

The muscle meshes were manually obtained from MR images using the software 3D Slicer (Fedorov et al., 2012). An example is shown in Figure II. To optimize the manual segmentation process, which is a time-consuming process, the MR images were resampled from 0.5729x0.75x0.5729 to 1x1x3 mm voxel size using MATLAB (The MathWorks Inc., 2023). The segmentation process was guided with relevant literature to ensure the highest possible fidelity (Freitas, n.d.; Lieber, 2010; Paulsen, & Waschke, 2018).

Each body segment was assumed to consist of three components: bone, muscle and fat/skin. The total mass of the segment was determined by:

$$M_{segment} = V_{bone} \cdot \rho_{bone} + V_{muscle} \cdot \rho_{muscle} + V_{fat/skin} \cdot \rho_{fat/skin} \quad [1]$$

where V represents the volume of each component and ρ the density of each tissue type. The fat/skin muscle volume was determined by:

$$V_{fat/skin} = V_{total} - V_{bone} - V_{muscle} \quad [2]$$

A brief literature search was conducted to determine the values of the densities, which are presented in Appendix C.1.

To determine the COM for each segment, the mass distribution of the segment was necessary. Therefore, a mass matrix was constructed (Müftü, 2022). First, a binary volume matrix was generated from the segmented meshes, where 1 represents a voxel inside the mesh, and 0 a voxel outside the mesh (Zhang & Chen, 2001). Each voxel was then multiplied by the respective density, resulting in a segment-specific mass matrix. The total mass matrix was obtained by summing the three component mass matrices.

The COM was computed using the following equations (Vallery & Schwab, 2020):

$$COM_x = \frac{\sum(x_i \cdot m_i)}{m_{total,segment}} \quad [3]$$

$$COM_y = \frac{\sum(y \cdot m_i)}{m_{total,segment}} \quad [4]$$

$$COM_z = \frac{\sum(z_i \cdot m_i)}{m_{total,segment}} \quad [5]$$

To ensure accuracy, the COM of each segment was plotted, as shown in Appendix D.3.

The inertia tensor was calculated relative to the COM, following the standard equations (Paluszek, 2023; Vallery & Schwab, 2020):

$$I_{xx} = \sum m_i \cdot (y^2 + z^2) \quad [6]$$

$$I_{yy} = \sum m_i \cdot (x^2 + z^2) \quad [7]$$

$$I_{zz} = \sum m_i \cdot (x^2 + y^2) \quad [8]$$

$$I_{xy} = I_{yx} = -\sum m_i \cdot (x \cdot y) \quad [9]$$

$$I_{xz} = I_{zx} = -\sum m_i \cdot (x \cdot z) \quad [10]$$

$$I_{yz} = I_{zy} = -\sum m_i \cdot (y \cdot z) \quad [11]$$

Further details on the computation of inertial parameters are provided in Appendix D.

2.1.3 Geometrical parameters

Various methods exist for representing muscle paths, ranging from simplified origin-insertion lines to more complex approaches (Garner, & Pandy, 2000; Hainisch et al., 2012; Modenese and Kohout, 2020). Given the anatomical complexity of muscle geometry, the simplest representation, a straight line between origin and insertion, was deemed inadequate. A more anatomically realistic complex approach, such as that proposed by Modenese and Kohout (2020), was considered. However, this tool was not available yet for OpenSim at the time of this study (SimTK, n.d.). An overview of different muscle path representations is shown in Figure III.

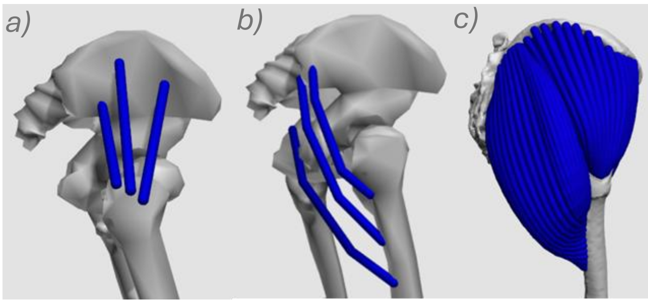

Figure III: Muscle path representations. *a)* origin-insertion representation of the m. gluteus medius *b)* muscle path representations using via points of m. gluteus maximus *c)* complex representation of the m. gluteus maximus and m. gluteus medius. Figure *a)* and *b)* were obtained from the RAJAG model and Figure *c)* was obtained using the model provided by Modenese & Kohout (2020).

The methodology described by Wesseling et al. (2016ab) was adopted to determine muscle paths. This method implemented muscle points, which involves attachment points (origo and insertion) and via-points to determine the muscle path (Figure IIIb). While the focus of Wesseling et al. (2016ab) was primarily on the hip region, in this study muscle points of the whole leg were defined in MR images, to the best possible accuracy (Lieber, 2010; Paulsen, & Waschke, 2018). The number and relative position of the muscle points were based on the scaled RAJAG. An example is presented in Figure IV. Due to asymmetries in the segmented bone geometries, the resulting muscle paths were not bilaterally symmetrical. Therefore, muscle points were not mirrored but individually defined for each side. Wrapping objects from this scaled model were adopted, except the wrapping cylinders for the *m. iliacus* and *m. psoas*. For these specific muscles, wrapping spheres were defined, following the methodology of Wesseling et al. (2016a). More details are presented in Appendix E.

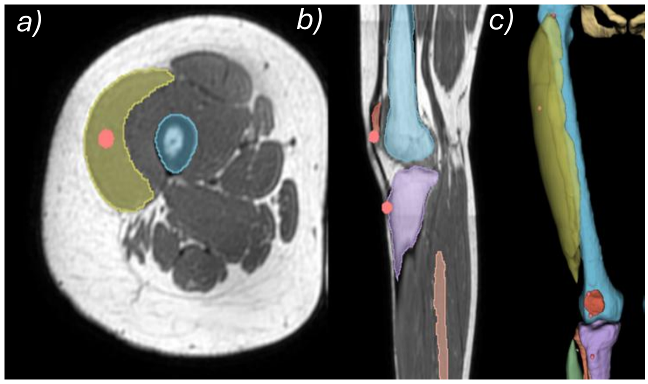

Figure IV: Example of determining muscle attachments and via points from MR images, in this case from the m. vastus lateralis. *a)* Axial view of MR image with muscle via point. *b)* Sagittal view of MR image with muscle points. *c)* Muscle points shown with segmented muscle and bones in 3D view.

2.1.4 Muscle parameters

To estimate OFL and tendon slack length, the MATLAB script developed by Modenese, Ceseracciu, Reggiani and Lloyd (2016) was initially applied. This script maps the normalized muscle operating conditions of an existing 'reference' model to the 'target' model. However, the initial output required further refinement. In particular, tendon slack length was adjusted to achieve a normalized fiber length of one at the corresponding joint angle as the Rajagopal model (Hainisch et al., 2012; Winby, Lloyd & Kirk, 2018). In this study, PA_{ofl} was adopted from the linearly scaled Rajagopal model.

$F_{iso,max}$ was calculated using the following equation, incorperating specific tension (σ_0^m) and Physiological Cross-Sectional Area (PCSA).

$$F_{iso,max} = \sigma_0^m \cdot PCSA \quad [12]$$

(Chen, & Franklin, 2023; Hainisch et al., 2012)

PCSA is the area of the cross section perpendicular to the fiber (Chen, & Franklin, 2023):

$$PCSA = \frac{V_{muscle}}{OFL} \quad [13]$$

Individual muscle volumes were determined by the individual mesh volumes obtained from MR images. Literature reports a range of values for σ_0^m, mostly between 30-90 N/cm^2

(Fukunaga, Roy, Shellock, Hodgson, & Edgerton, 1996; Hainisch et al., 2012; Hansfield et al., 2013; Yoganandan, Arun, Dickman & Benzel, 2017). A value of 60 N/cm^2 was adopted from Rajagopal et al. (2016) in this study. Further details on the computation of muscle parameters are provided in Appendix F.

2.2 Generic model

The scaled RAJAG model served as the generic male-based model utilized in this study. As the YONI model was a lower extremity model, the upper body of the scaled RAJAG model was removed.

2.3 Marker positions for simulations

To minimize marker errors during simulation, marker positions were updated using the marker positions obtained from the 3D scan for all models in this study. The model was posed in the A-pose using the static marker data and overlaid with the 3D scan in Blender (Blender Development Team, 2022). A vector was calculated between the corresponding markers on the A-pose model and the 3D scan to calculate the marker position in the original pose of the model (pose obtained from STAPLE).

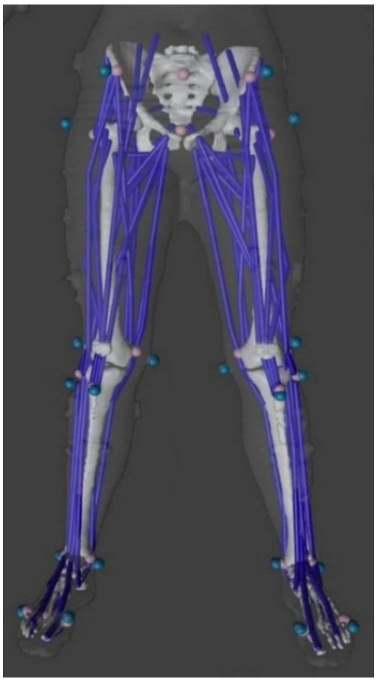

Figure V: YONI model posed in A-pose, overlayed with the 3D body scan. Pink markers are the original STAPLE bony landmarks and blue are the markers from the 3D body scan.

2.4 Model comparisons

To evaluate the validity of the developed YONI model and compare it to the scaled RAJAG model, a two-part analysis was conducted. Analysis I involved a comparison of the YONI model to the RAJAG model in simulation for the subject that YONI model was based on (individualized vs scaled generic model). Analysis II involved a comparison of the YONI model to the RAJAG model in simulation of a different female subject. Since the skeletal part of the YONI model is semi-automated process, a new subject specific skeletal model was created following the same procedure discussed in this method. This female subject was randomly chosen from the dataset. The new personalized model was compared to a scaled YONI model and a scaled RAJAG model. An overview is presented in Figure VIa. For both analyses, a series of simulations were conducted using OpenSim 4.5 (Delp et al., 2007).

First, an Inverse Kinematics (IK) analysis was performed to evaluate root mean square (RMS) marker error and joint angles. Then, an Inverse Dynamics (ID) was performed to compute joint moments. Finally, a Static Optimization (SO) analysis was used to estimate joint reaction forces. An overview is presented in Figure VIb. RMS marker errors were evaluated across the entire sit-to-walk motion as well as specifically during walking phases. Joint angles were analysed during walking phases, which was normalized to a full gait cycle (0-100%). For the ID and SO analyses, only gait cycles with valid forces plate data were included. Gait cycles for which the optimization failed at certain time steps, were excluded from further analysis.

2.4.1 Statistical tests

The RMS marker error was quantified using the mean and standard deviation (SD). To evaluate the agreement between the mean joint angle profiles of the models, Pearson's Correlation Coefficient (*r*) was calculated, provided that the data was normally distributed as assessed by a Shapiro-Wilk test. A statistical parametric mapping (SPM) paired sample t-test was conducted for the joint angles. For both the ID and SO outcomes, mean and SD were plotted. A *p*-value of 0.05 was considered statistically significant. All analyses were conducted using MATLAB (The MathWorks Inc., 2023).

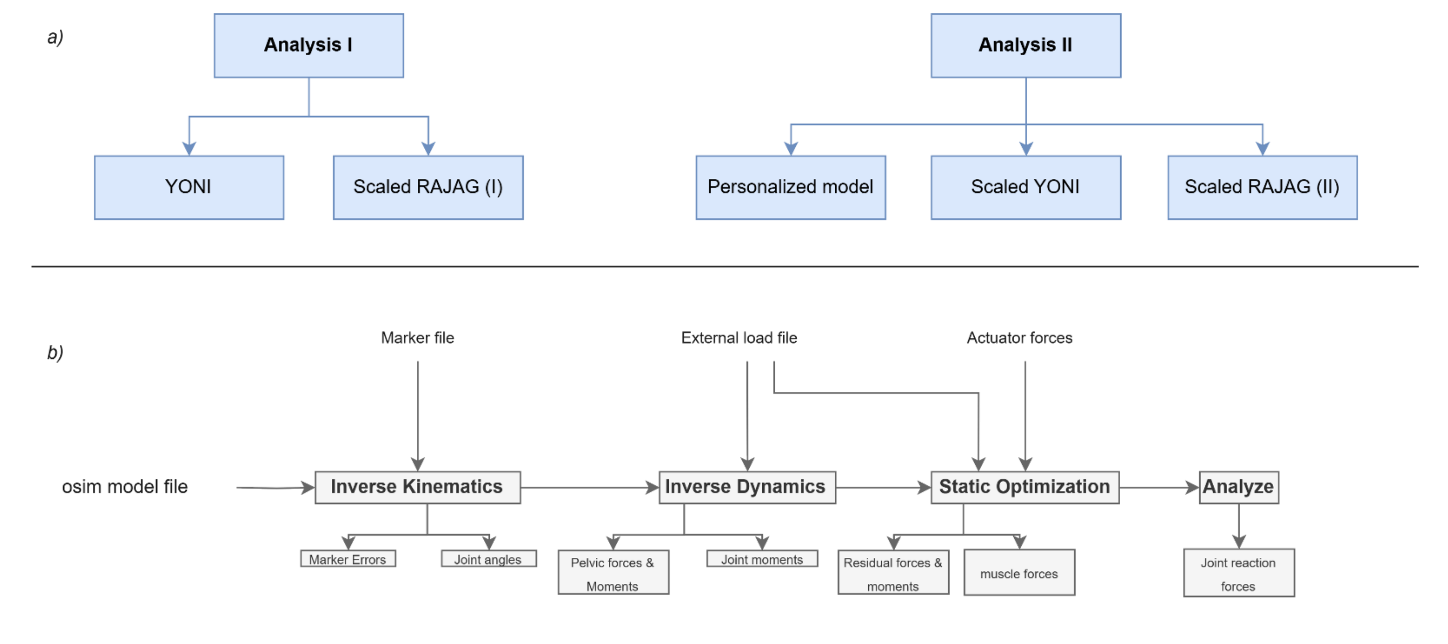

Figure VI: *a)* Overview of Analysis I and II, with model used. *b)* Overview of the used OpenSim analysis, with their inputs and outputs.

3. RESULTS

Following the method described in Section 2, the YONI model was developed, which is presented in Figure VII, together with the scaled RAJAG model.

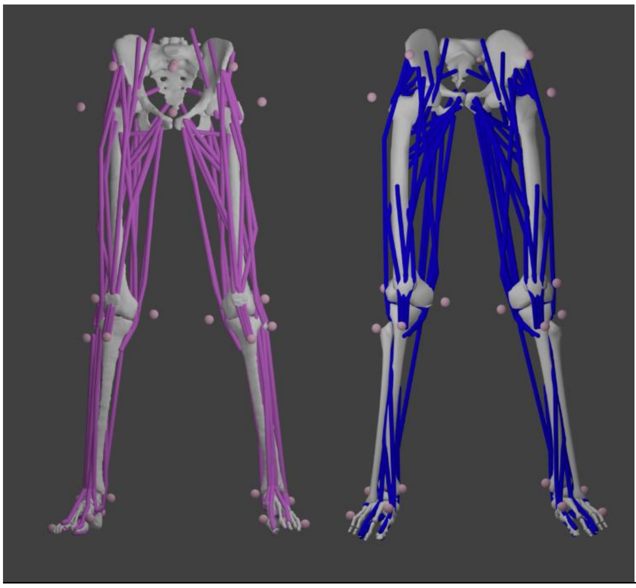

Figure VII: The developed YONI model (left) and a scaled RAJAG model (right) of the same subject, both posed in the A-pose based on the subject's static marker data.

3.1 Results analysis 1

3.1.1 Marker errors

The mean RMS error for the YONI model was 0.0146 m (SD = 0.0045) and for the scaled RAJAG model 0.0163 m (SD = 0.0200). Focusing specifically on walking of the sit-to-walk motion, the mean RMS value for the YONI model was 0.0112 m (SD = 0.0019) and for the scaled RAJAG model 0.0078 m (SD = 0.0007).

3.1.2 Joint angles

In Figure VIII, mean joint angles and SD intervals are presented. Shapiro-Wilk test revealed a *p*-value higher than 0.05 for all joint angles, which indicates normality of the data. Significant differences were generally observed across all joint angles throughout the entire gait cycle as indicated by the SPM paired-t-test, except for right knee angle. Pearson's Correlation Coefficients are presented in Table I, which is low for hip rotation.

Table I: Pearson's correlation coefficient of the joint angles of analysis I between YONI and the scaled RAJAG model.

	Hip flexion r/l	***Hip adduction r/l***	***Hip rotation r/l***	***Knee flexion r/l***	***Ankle flexion r/l***
r	*0.9604/ 0.9989*	*0.9307/ 0.9961*	*0.4755/ 0.5935*	*0.9993/ 0.9998*	*0.9635/ 0.09880*

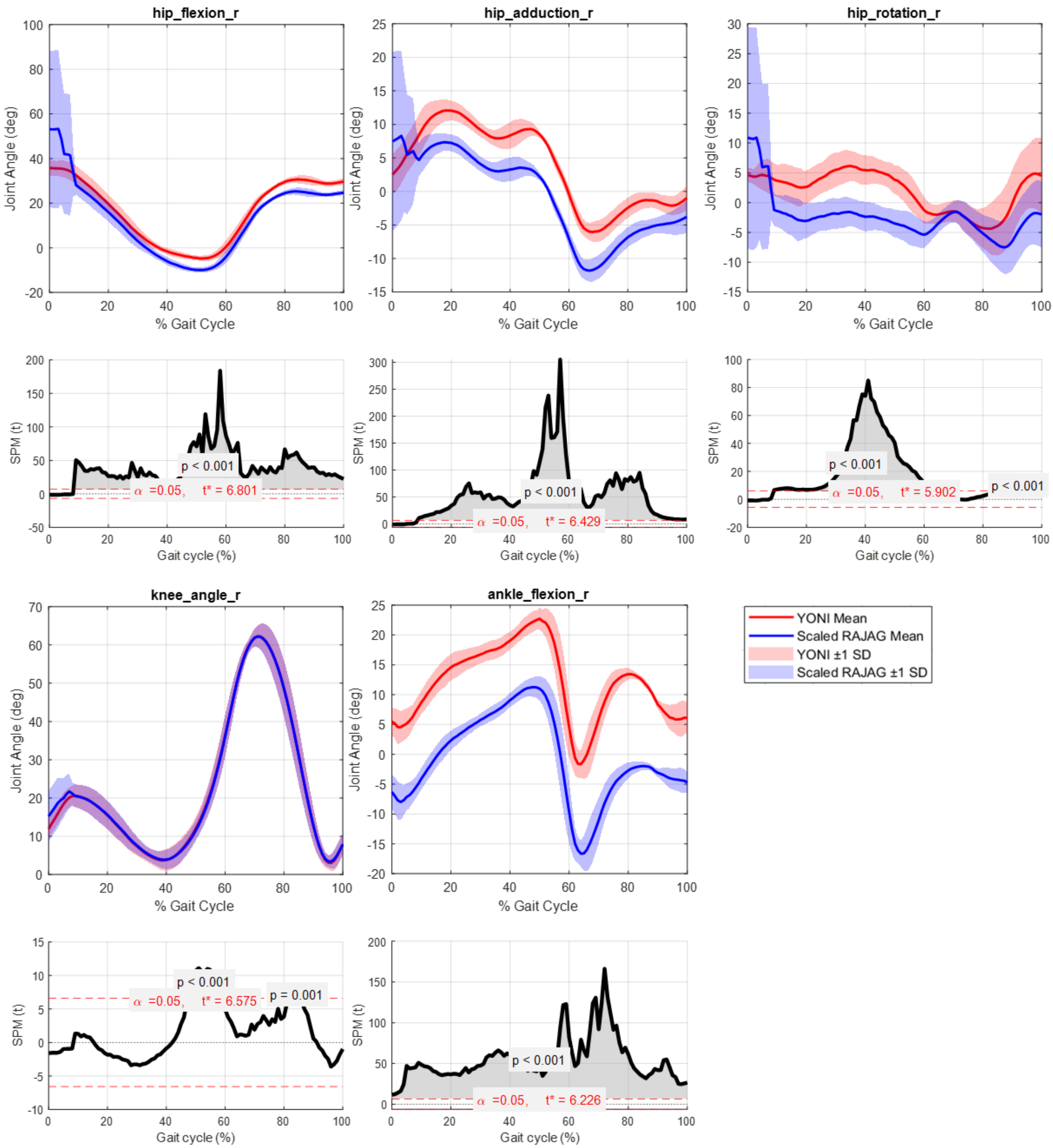
hip_flexion_r
hip_adduction_r
hip_rotation_r
Joint Angle (deg)
% Gait Cycle
SPM (t)
Gait cycle (%)
p < 0.001
α =0.05, t* = 6.801
α =0.05, t* = 6.429
α =0.05, t* = 5.902
knee_angle_r
ankle_flexion_r
α =0.05, t* = 6.575
p = 0.001
α =0.05, t* = 6.226
YONI Mean
Scaled RAJAG Mean
YONI ±1 SD
Scaled RAJAG ±1 SD

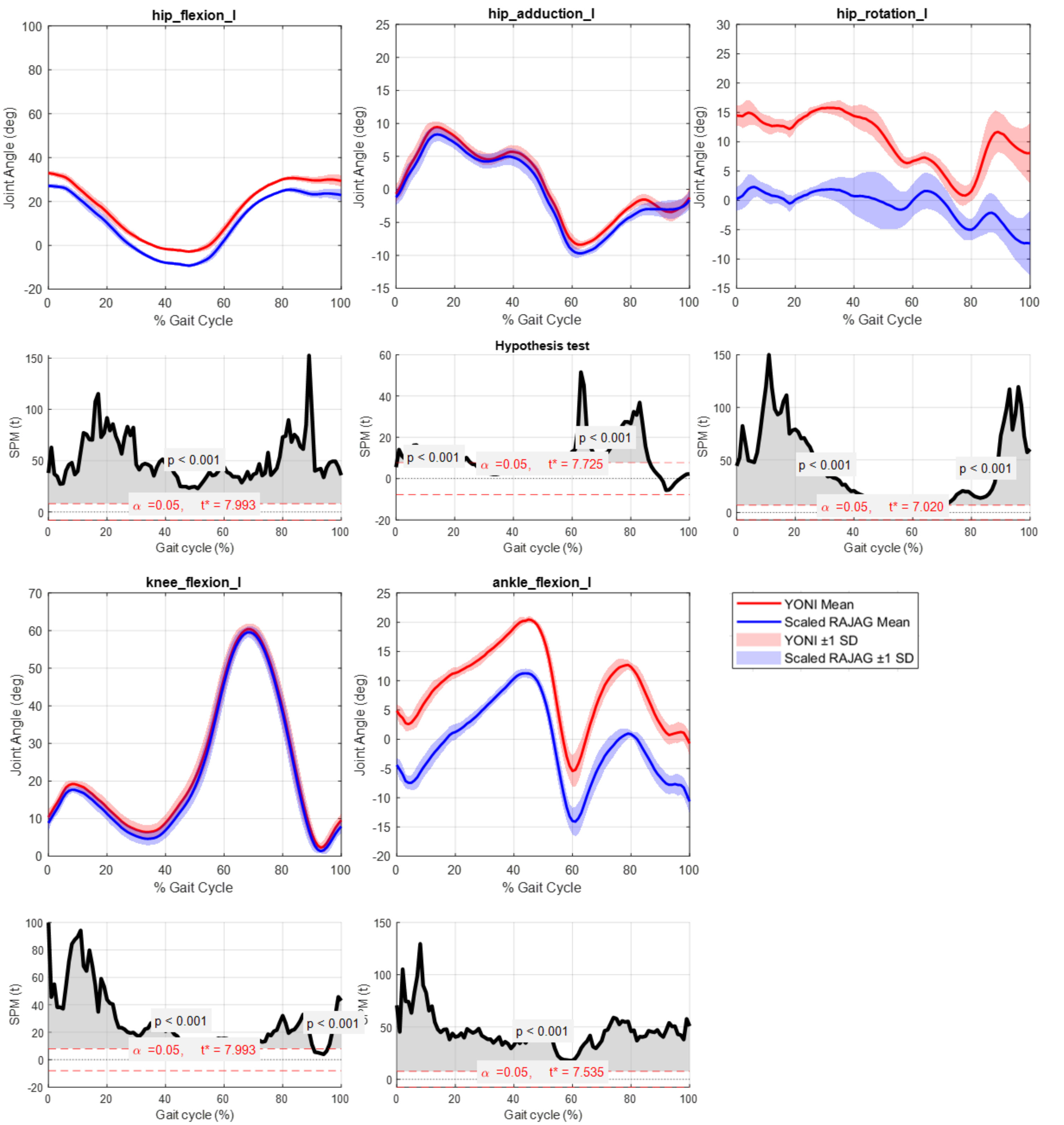

Figure VIII: *upper:* Mean joint angles with their ±1 SD intervals, calculated over multiple gait cycles and plotted against % gait cycle. Hip flexion angle: (+) flexion, (-) extension; Hip adduction: (+) adduction, (-) abduction; Hip rotation: (+) internal, (-) external; Knee flexion: (+) flexion, (-) extension; Ankle flexion: (+) dorsiflexion, (-) plantarflexion. *Lower*: SPM paired t-test plots.

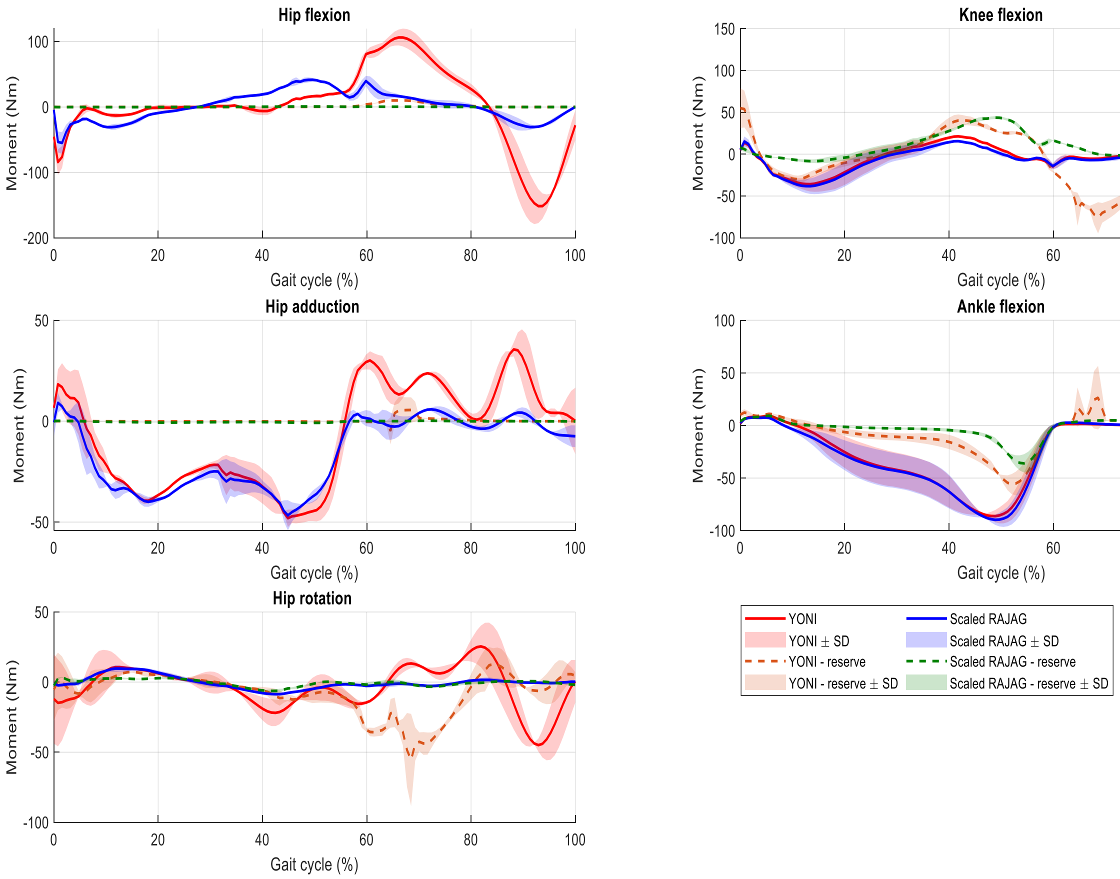

Figure IX: Mean results of ID and SO with their ±1 SD intervals. Mean over two gait cycles. Resulting moments from the ID shown as solid line, from the SO shown as a dashed line. Hip flexion: (+) flexion, (-) extension; Hip adduction: (+) adduction, (-) abduction; Hip rotation: (+) internal, (-) external; Knee flexion: (+) flexion, (-) extension; Ankle flexion: (+) dorsiflexion, (-) plantarflexion. Mean over two gait cycles.

Results of ID moments and SO reserve moments for the hip, knee and ankle are presented in Figure IX. Joint moments reveal larger differences between YONI and scaled RAJAG models in the hip angles during the swing phase. Reserve moments were low in hip flexion and hip adduction, but higher in knee flexion and ankle flexion.

The RAJAG model showed lower contribution of reserve moments in hip rotation compared to the YONI model. The pelvic forces and moments are shown in Appendix H.1.

3.1.4 Joint Reaction forces

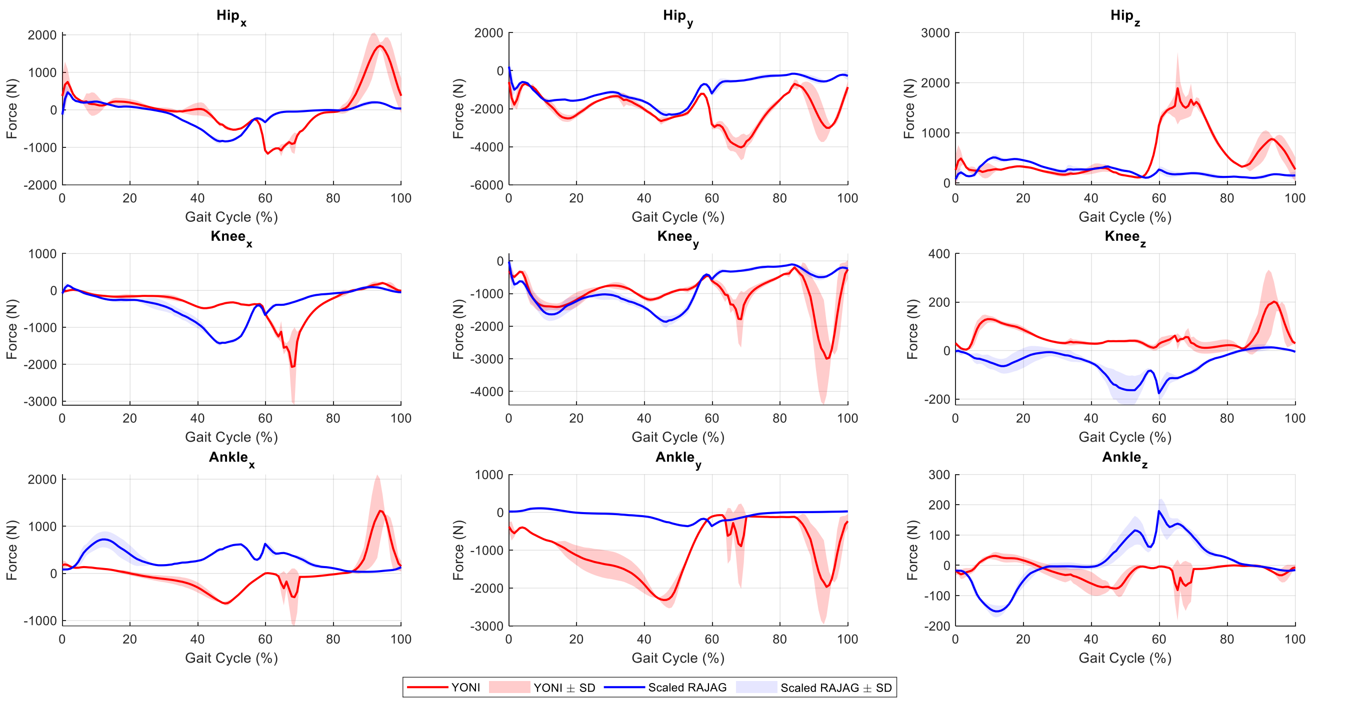

Figure X: Joints reaction forces for the scaled YONI model and the scaled RAJAG model. X-axis represents the anterior(+)/posterior(-) direction, Y-axis the vertical direction and Z-axis represents the medial/lateral direction.

The joint reaction forces (JRF) for the hip, knee and ankle joint throughout the gait cycle obtained from the YONI and scaled RAJAG model are shown in Figure X. Visual inspection reveals differences across all joint angles, with the ankle reaction forces appearing the most similar between the two models. Notably, peaks at the end of the gait cycle are evident in the YONI model that are not apparent in the scaled RAJAG model.

3.2 Results analysis II

3.2.1 Marker errors

The mean RMS error for the personalized model was 0.0138 m (SD = 0.0054), for the scaled RAJAG model 0.0259 m (SD = 0.0237) and for the scaled YONI model 0.0134 m (SD = 0.0048). Focusing specifically on the walking phases, the mean RMS value for the personalized model was 0.0096 m (SD = 0.0013), for the scaled RAJAG model 0.0247 m (SD = 0.0268) and for the scaled YONI model 0.0097 m (SD = 0.0010).

3.2.2 Joint angles

In Figure XI, mean joint angles and SD intervals are presented. SPM paired-t-test for each joint angle is presented in the same figure. Shapiro-Wilk test revealed a p-value higher than 0.05 for all joint angles, which indicates normality of the data. SPM paired t-test showed significant differences for all joint angles for both the YONI and the scaled RAJAG model compared to the personalized model. Pearson's Correlation Coefficients are presented in Table II.

Table II: Pearson's correlation coefficient of the joint angles of analysis II.

	Hip flexion r/l	*Hip adduction r/l*	*Hip rotation r/l*	*Knee flexion r/l*	*Ankle flexion r/l*
r personalized vs YONI	0.9993/ 0.9994	0.9975/ 0.9967	0.5814/ 0.9169	0.9999/ 1.0000	0.9965/ 0.9813
r personalized vs RAJAG	0.9646/ 0.9988	0.9798/ 0.9936	0.5493/ 0.8665	0.9982/ 0.9997	0.9323/ 0.9554

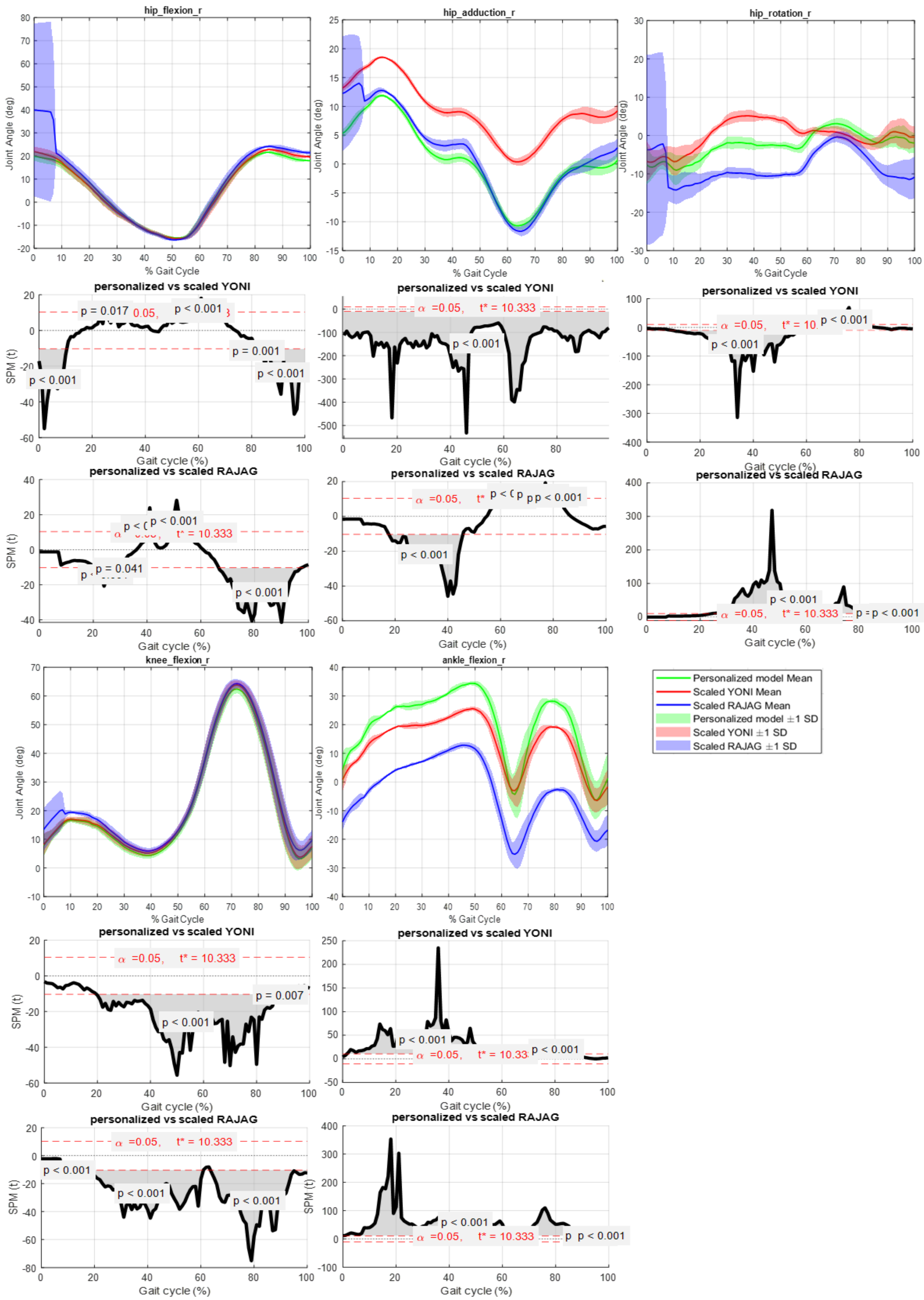

hip_flexion_r
hip_adduction_r
hip_rotation_r
Joint Angle (deg)
% Gait Cycle
personalized vs scaled YONI
personalized vs scaled RAJAG
SPM (t)
Gait cycle (%)
knee_flexion_r
ankle_flexion_r
Personalized model Mean
Scaled YONI Mean
Scaled RAJAG Mean
Personalized model ±1 SD
Scaled YONI ±1 SD
Scaled RAJAG ±1 SD

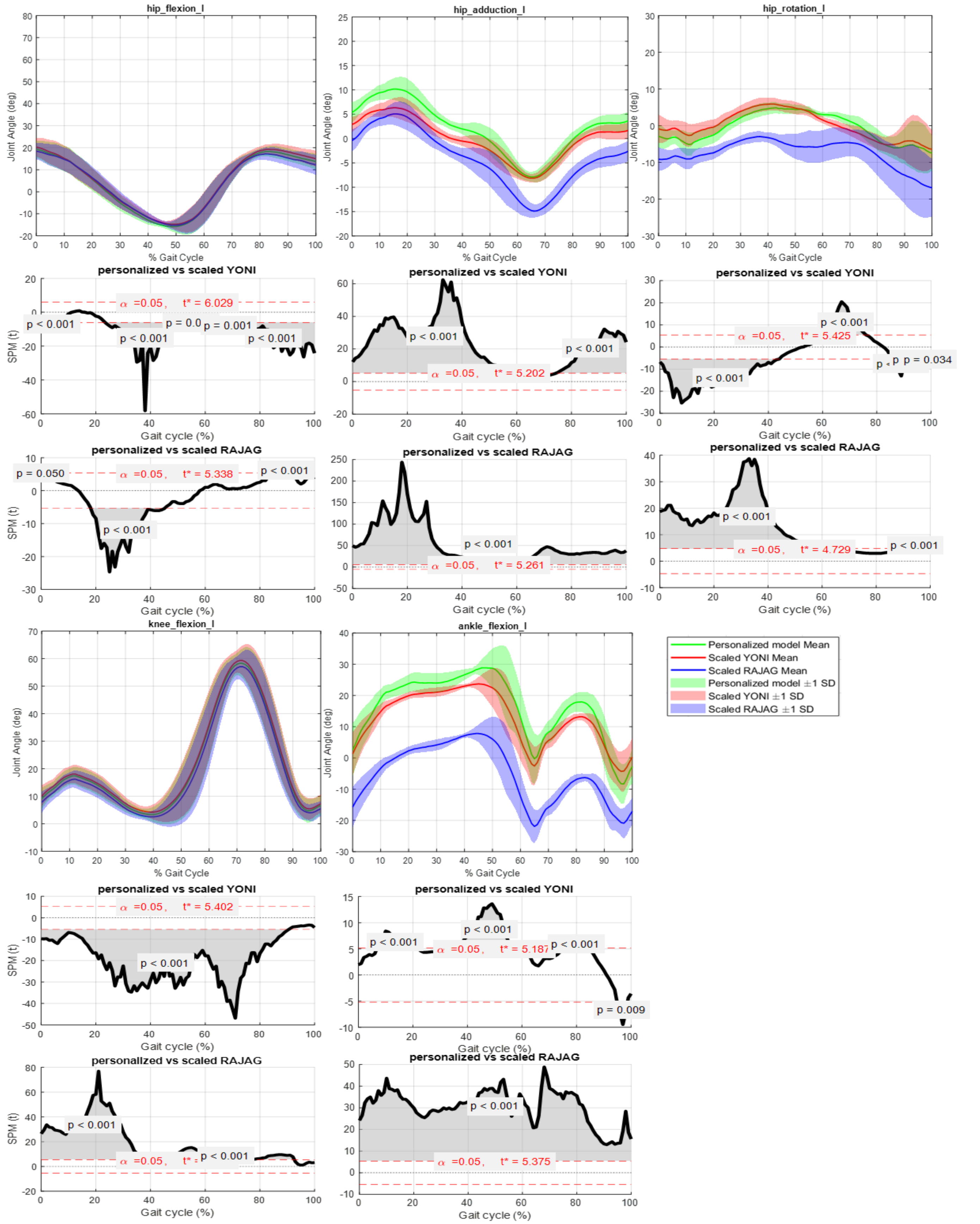

Figure XI: *upper:* Mean joint angles with their ±1 SD intervals, calculated over multiple gait cycles and plotted against % gait cycle. Hip flexion angle: (+) flexion, (-) extension; Hip adduction: (+) adduction, (-) abduction; Hip rotation: (+) internal, (-) external; Knee flexion: (+) flexion, (-) extension; Ankle flexion: (+) dorsiflexion, (-) plantarflexion. *Lower*: SPM paired t-test plots

3.2.3 Inverse Dynamics and Static Optimization

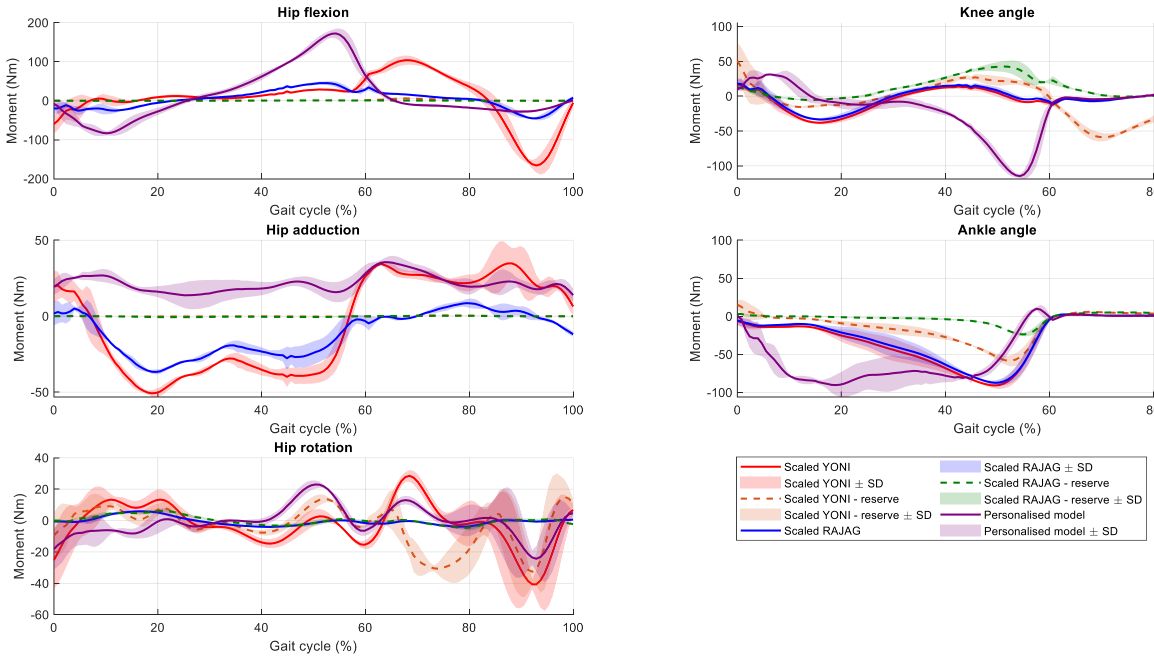

Figure XII: Mean results of ID and SO with their ±1 SD intervals. Resulting moments from the ID shown as solid line, from the SO shown as a dashed line. Hip flexion: (+) flexion, (-) extension; Hip adduction: (+) adduction, (-) abduction; Hip rotation: (+) internal, (-) external; Knee flexion: (+) flexion, (-) extension; Ankle flexion: (+) dorsiflexion, (-) plantarflexion.

Results of ID moments and SO reserve moments for the hip, knee and ankle are presented in Figure XII. Joint moments vary across all three models. Notably, for hip adduction in swing phase, the YONI model closely approximates the personalized model, whereas the RAJAG model does not. Similarly, the YONI model appears to perform better than the RAJAG model for hip rotation. Reserve moments were low in hip flexion and hip adduction, but higher in knee flexion and ankle flexion. The RAJAG model showed lower contribution of reserve moments in hip rotation compared to the YONI model.

The pelvic forces and moments are shown in Appendix H.2.

3.2.4 Joint reaction forces

Figure XIII presents hip, knee, and ankle joint reaction forces. Visual inspection reveals differences across all joints, with the ankle reaction forces appearing the most similar between the two models. Notably, peaks at the end of the gait cycle are evident in the scaled YONI model that are not apparent in the scaled RAJAG model.

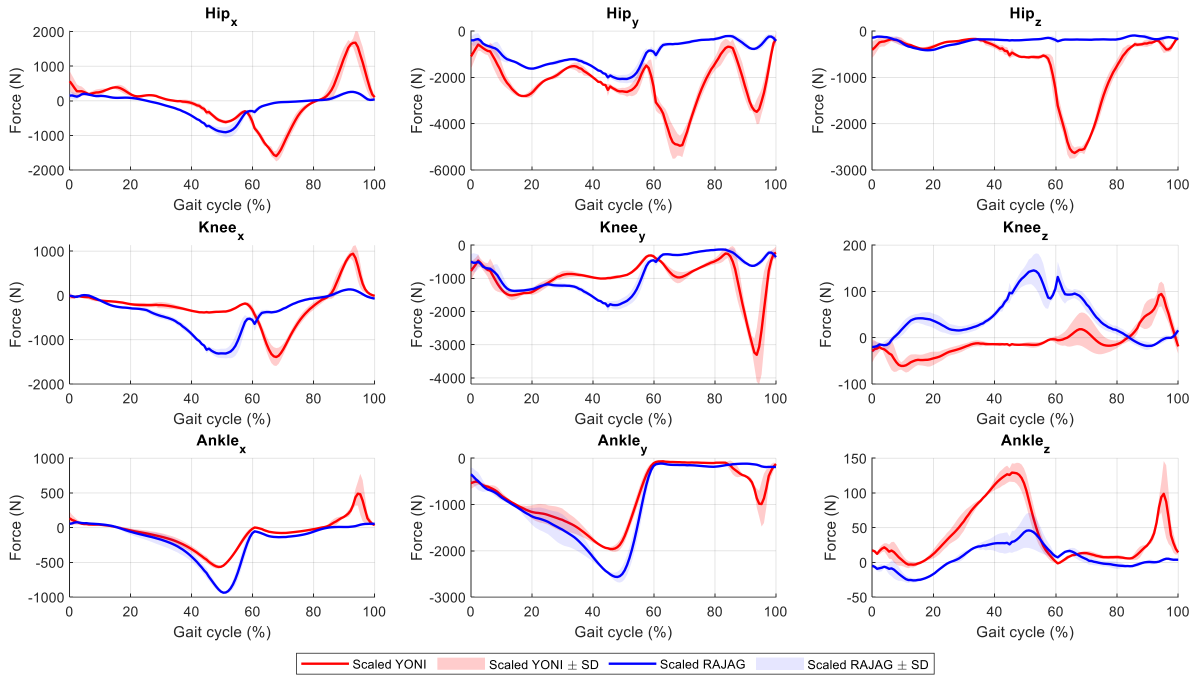

Figure XIII: Joints load forces for the scaled YONI model and the scaled RAJAG model, with their +- SD intervals. X-axis represents the anterior(+)/posterior(-) direction, Y-axis the vertical direction and Z-axis represents the medial/lateral direction. Mean is over three gait cycles.

4. DISCUSSION

The aim of this study was to develop a female based lower extremity musculoskeletal model based on MR images (YONI) and to compare the YONI model to the scaled generic RAJAG model in simulations for female subjects(s).

4.1 Kinematic results

4.1.1 RMS marker error

Although the YONI model showed a lower mean RMS marker error compared the scaled RAJAG model for the whole sit-to-walk motion in analysis I, the scaled RAJAG exhibited a lower mean RMS error compared to the YONI model during walking. This finding was unexpected, as the YONI model incorporates bone geometries derived from the same subject from whom motion data were collected, and efforts were made to minimize RMS marker error by utilizing markers derived from a 3D scan. Several factors might contribute to this observation during walking. First, differences exist in joint definitions between the YONI model and the generic (scaled) RAJAG model. While the YONI model benefits from subject-specific bone geometry, the joint definitions might be more optimally suited for human gait in the RAJAG model. Secondly, a potential source of error lies in the acquisition of the 3D-scan based marker positions. This said, some degree of error is unavoidable, as skin markers move relative to their underlying bone structure throughout motion (Cappozzo, Catani, Leardini, Benedetti & Della Croce, 1996). Despite these factors, the RMS marker error for both models remained below the generally accepted threshold of 2 cm (Hicks et al., 2014). For analysis II, the scaled YONI model outperformed the scaled RAJAG model in terms of RMS marker error. An interesting finding was that the YONI model even showed slightly better performance than the fully personalized model during the whole sit-to-walk motion, although this difference was not substantial. The scaled RAJAG model performed poorly, with RMS marker errors exceeding the accepted threshold proposed by Hicks et al. (2014). This suggests a benefit in using the scaled female-based YONI model when subject-specific bone geometries are not available for female subjects compared to a scaled RAJAG model. However, to fully validate these and further results, further research across larger cohort of subjects, and potentially exploring alternative marker placement strategies, is crucial.

4.1.2 Joint angles

Investigation of the calculated joint angle profiles provided insights into the kinematic output of the model. For analysis I, SPM revealed significant differences for all joint angles throughout the whole gait and Pearson correlations revealed differences were evident in the hip rotation angle profiles between the YONI and scaled RAJAG model. These differences in hip rotation angle patterns could be a consequence of the fundamental differences in pelvic geometry between sexes. In analysis II, the scaled YONI model provided joint angle magnitudes that visually aligned more closely with the personalized model compared to the scaled RAJAG model. This finding was further supported by the paired t-test SPM, where overall lower t-values were observed for the YONI model compared to the scaled RAJAG model and that Pearson's Correlation Coefficient were consistently higher when comparing the scaled YONI model to the personalized model than when comparing the scaled RAJAG model to the personalized model. These findings suggests that the YONI model achieved a more accurate prediction of joint angles than the RAJAG model for female subjects. Furthermore, the observed mean joint angle patterns in both analysis I and II aligned well with data reported in previous studies on healthy gait (Modenese et al., 2018; Pizzolato, Reggiani, Modenese & Lloyd, 2016; Sylvester, Lautzenheiser & Kramer, 2021;), which supports the overall validity of the model's kinematic output. A notable observation across both analyses was the significantly higher variability in the scaled RAJAG models during the initial 10% of the gait cycle, particularly pronounced in the hip joint. This might indicate limitations in the ability of accurately represent the early stance phase kinematics of a female subject, although its unilateral occurrence on the right side warrants further investigation.

4.2 Dynamic results

Analysis of the dynamic outputs, which involves joint moments, reserve actuator moments and joint loads, revealed key differences between the models. It is crucial to preface the interpretation of these dynamic results with an important limitation: the number of gait cycles available for analysis was severely restricted due to optimization failures in the static optimization process, which indicated the models' inability to reproduce the muscle strength needed. This limited sample size inherently reduced statistical power, making robust statistical comparisons and definitive claims of significance impossible. Consequently, statistical tests were not performed on these dynamic outcomes. Had more gait cycles been available, SPM would have been used to assess significance. Therefore, the findings related to joint moments, reserve actuator moments and joint loads represent preliminary observations indicating potential trends and differences, rather than conclusive evidence.

4.2.1 Reserve actuator moments

Elevated reserve actuator moments indicate the model's inability to fully reproduce the motion solely through muscular action. When examining reserve moments for both analysis I and II, values were consistently low for hip flexion and hip adduction, but higher for the knee and ankle angle in the YONI model compared to the (scaled) YONI model. In the (scaled) YONI model, these higher reserve moments at the knee and ankle were more pronounced compared to the scaled Rajagopal models. While efforts were made to minimize the contribution of reserve actuators, further reduction resulted in OpenSim warnings, indicating the model could not generate sufficient force. The higher reserve moments for the knee and ankle in the Yoni model might be caused by the influence of ground reaction forces (GRF) acting on these joints, highlighting potential limitations in the muscle strength representations or muscle path definitions around these specific joints (Maarleveld et al., 2024). Future work should investigate the impact of increasing muscle strength to reduce this dependence on reserve actuators.

4.2.2 Joint Reaction forces

Both results from analysis I and II for all models aligned with ranges reported in existing healthy gait (Kumar, Manal & Rudolph, 2012; Lace & Blażkiewicz, 2021; Modenese et al., 2018; Sylvester et al., 2021). A critical finding emerging from both analysis I and II was the YONI model's consistent exhibition of larger peak joint reaction forces during the end of the gait cycle. To further investigate these discrepancies in joint loads and associated higher reserve moments, muscle forces and activations were analysed. Interestingly, the female model exhibited distinct peaks in muscle forces and activation towards the end of the gait cycle for most muscles, which is not observed in the scaled RAJAG model. These late-swing phase peaks correlated with the peaks of joint reaction forces. If certain muscles in the YONI model are operating at less efficient points on their force-length-velocity curves during the swing phase, a greater activation level might be required to produce the same functional output, consequently increasing joint loads. Alternatively, if the YONI model's muscle parameters are calibrated to produce inherently higher forces at specific instances to fulfil a functional role, this would directly translate to higher joint kinetics. Therefore, it is crucial that future research focuses on updating the muscle parameters, in particular OFL.

4.3 Limitations and future recommendations

Beyond the statistical limitations discussed in Section 4.2, the development of the YONI model in this study had several limitations.

First, the muscle segmentation was not performed by an MRI expert. Despite dedicated efforts to ensure accuracy, some degree of variability within the muscles is still present. It is believed that this variability did not significantly impact the calculation of the inertia parameters (COM, Inertia, Mass) as the total volume of the muscles for a specific segment was used. However, since the calculation of PCSA required the total volume of each individual muscle, the influence on

PCSA might be more substantial, which results in an altered $F_{iso,max}$, thereby influencing overall muscle behavior and strength of the model. Comparing the PCSA values of the YONI model with the experimental PCSA values provided in Maarleveld et al. (2024), most muscles in the YONI model exhibited similar PCSA values. Where differences were observed, muscles more frequently showed lower PCSA values compared to Maarleveld et al. (2024) rather than higher values. This suggests that the muscle segmentation affected the predicted muscle strength capabilities of the model. Therefore, in future work, segmentation should be done manually by a MRI expert, or with the use of automatic segmentation models to ensure the highest accuracy.

Despite efforts to optimize the accuracy of the inertial parameters, certain limitations prevent complete accuracy. Firstly, tendons were not segmented separately and are included within the skin/fat segmentation. While the literature lacks a definitive density value for tendons (Hashemi, Chandrashekar & Slauterbeck, 2005), it is plausible that their density differs from that of skin/fat. Similarly, nerves and blood vessels were also included in the skin/fat segment and not calculated as separate components.

Despite dedicated efforts to align muscle paths with the MR images, the muscle geometry of the female model is not yet entirely refined. Specifically, the functionality of wrapping objects, which is crucial for the realistic muscle path definition, remains a challenge. Some muscles did not correctly wrap around the wrapping surface taken from the scaled RAJAG model, at the end range of motion (ROM). While this limitation has minimal impact during normal gait given that the joints do not typically reach their end ROM, this needs to be improved in the future. In addition, the wrapping spheres of the *m. psoas* and *m. iliacus*, which were based on the methodology of Wesseling et al. (2016a), do not consistently function optimally within the current model. This is evident in the muscle moment arm graph (Appendix G.3) for the *m. psoas*, where an abrupt jump is observed. Future work will focus on refining these wrapping surfaces, to improve the model's accuracy.

It is important to note that the current female model does not incorporate sex-specific differences in muscle parameters. However, this highlights a broader limitation in existing musculoskeletal modelling, as no validated scaling approach currently exists that incorporates sex-based differences in muscle parameters. Further research is needed to characterize potential sex-based differences of the muscle parameters. Until such data is available, interpreting results from this female model should be done with care.

Although the patellofemoral joint was updated to allow patellar movement, further refinement is recommended in future work. Since the current analysis did not specifically focus on the patellofemoral joint, any potential limitations in its modelling are not expected to have influenced the results significantly. However, this is important to consider for studies that do focus on the patellofemoral joint.

Lastly, a potential limitation concerns the positioning of the foot during MRI acquisition. Since the images were obtained while the subject was lying down, the anatomy of the foot appears slightly curved compared to the position while standing. This supports the finding of Shelton et al. (2018), which suggests that such posture-related variations within the foot can affect joint movements of the hindfoot (Hirschmann, Pfirrmann, Klammer, Espinosa & Buck, 2013; Shelton et al., 2018). Given that the standing posture is likely the most representative for musculoskeletal modelling, future refinements should involve segmenting bone meshes from MRI images obtained in a weight-bearing position. Although foot joint mechanics were not a primary focus in this particular study, this limitation is important to mention for studies where this is of interest.

5. CONCLUSION

This study successfully developed a female based lower extremity musculoskeletal model, named YONI, based on MR images, aiming to compare kinematic and dynamic results between the YONI model and the RAJAG model in simulations for female subject(s). The findings suggest that the YONI model may offer superior performance in kinematic and dynamic outputs compared to the scaled RAJAG model for female subjects. However, while kinematic and dynamic differences were evident, it does not allow for definitive conclusions regarding fundamental sex differences due to model limitations and data constraints, highlighting the need for further improvements. Nevertheless, this work represents a crucial step toward the development of a female musculoskeletal model, essential for advancing biomechanical research and clinical applications for women.

ACKNOWLEGDEMENT

First and foremost, I would like to thank my supervisor Dr. ir. E. van der Kruk for her guidance, insightful feedback and continuously challenging me to achieve my best. I also want to thank ir. J. Cueto Fernandez. Her knowledge of this project was incredibly helpful.

REFERENCES

Abdullah, M., Hulleck, A. A., Katmah, R., Khalaf, K., & El-Rich, M. (2024). Multibody dynamics-based musculoskeletal modeling for gait analysis: a systematic review. *Journal Of NeuroEngineering And Rehabilitation*, *21*(1). https://doi.org/10.1186/s12984-024-01458-y

Andersen, M. S. (2020). Introduction to musculoskeletal modelling. *Computational Modelling of Biomechanics and Biotribology in the Musculoskeletal System* (pp. 41–80). https://doi.org/10.1016/b978-0-12-819531-4.00004-3

Blender Development Team. (2022). Blender (Version 4.2.3) [Computer software]. Blender Foundation. https://blender.org

Bram JT, Magee LC, Mehta NN, Patel NM, Ganley TJ. Anterior Cruciate Ligament Injury Incidence in Adolescent Athletes: A Systematic Review and Meta-analysis. *The American Journal of Sports Medicine.* 2021;49(7):1962-1972. DOI:10.1177/0363546520959619

Brattström, H. (1964). Shape of the Intercondylar Groove Normally and in Recurrent Dislocation of Patella: A Clinical and X-Ray Anatomical Investigation. Acta Orthopaedica Scandinavica, https://doi.org/10.3109/ort.1964.35.suppl-68.01

Brotto, M., & Bonewald, L. (2015). Bone and muscle: Interactions beyond mechanical. *Bone*, *80*, 109–114. https://doi.org/10.1016/j.bone.2015.02.010

Cappozzo, A., Catani, F., Leardini, A., Benedetti, M., & Della Croce, U. (1996). Position and orientation in space of bones during movement: experimental artefacts. *Clinical Biomechanics*, *11*(2), 90–100. https://doi.org/10.1016/0268-0033(95)00046-1

Chen, Z., & Franklin, D. W. (2023). Musculotendon Parameters in Lower Limb Models: Simplifications, Uncertainties, and Muscle Force Estimation Sensitivity. *Annals Of Biomedical Engineering*, *51*(6), 1147–1164. https://doi.org/10.1007/s10439-023-03166-5

Delp, S. L., Anderson, F. C., Arnold, A. S., Loan, P., Habib, A., John, C. T., … Thelen, D. G. (2007). *OpenSim: Open-Source Software to Create and Analyze Dynamic Simulations of Movement. IEEE Transactions on Biomedical Engineering, 54(11), 1940–1950.* doi:10.1109/tbme.2007.901024

Delp, S.L., Loan, J.P., Hoy, M.G., Zajac, F.E., Topp, E.L., & Rosen, J.M. (1990). An interactive graphics-based model of the lower extremity to study orthopaedic surgical procedures. *IEEE Transactions on Biomedical Engineering, 37(8), 757-767. https://doi.org/10.1109/10.102791*

Fedorov A., Beichel R., Kalpathy-Cramer J., Finet J., Fillion-Robin J-C., Pujol S., Bauer C., Jennings D., Fennessy F.M., Sonka M., Buatti J., Aylward S.R., Miller J.V., Pieper S., Kikinis R. (2012). 3D Slicer as an Image Computing Platform for the Quantitative Imaging Network. *Magnetic Resonance Imaging. 2012 Nov;30(9):1323-41.* PMID: 22770690. PMCID: PMC3466397

.Firouzabadi, A., Arjmand, N., Pan, F., Zander, T., & Schmidt, H. (2021). Sex-Dependent Estimation of Spinal Loads During Static Manual Material Handling Activities—Combined in vivo and in silico Analyses. *Frontiers in Bioengineering And Biotechnology*, *9*. https://doi.org/10.3389/fbioe.2021.750862Freitas A. (n.d.). *Musculoskeletal MRI.* Retrieved April 2nd, 2025 from https://www.freitasrad.net/pages/Basic_MSK_MRI/basic-msk-mri.php

Fukunaga, T., Roy, R. R., Shellock, F. G., Hodgson, J. A., & Edgerton, V. R. (1996). *Specific tension of human plantar flexors and dorsiflexors. Journal of Applied Physiology, 80(1), 158–165.* doi:10.1152/jappl.1996.80.1.158

Garner, B.A., & Pandy, M.G. (2000). The Obstacle-Set Method for Representing Muscle Paths in Musculoskeletal Models. *Computer Methods in Biomechanics and Biomedical Engineering, 3(1), 1–30.* doi:10.1080/10255840008915251

Griffin, L. Y., Albohm, M. J., Arendt, E. A., et al. (2006). Understanding and preventing noncontact anterior cruciate ligament injuries: a review of the Hunt Valley II meeting, January 2005. American Journal of Sports Medicine, 34(9), 1512-1532.

Hainisch, R., Gfoehler, M., Zubayer-Ul-Karim, M., & Pandy, M. G. (2012). Method for determining musculotendon parameters in subject-specific musculoskeletal models of children developed from MRI data. *Multibody System Dynamics*, *28*(1–2), 143–156. https://doi.org/10.1007/s11044-011-9289-0

Handsfield, G. G., Meyer, C. H., Hart, J. M., Abel, M. F., & Blemker, S. S. (2013). Relationships of 35 lower limb muscles to height and body mass quantified using MRI. *Journal of Biomechanics*, *47*(3), 631–638. https://doi.org/10.1016/j.jbiomech.2013.12.002

Hashemi, J., Chandrashekar, N., & Slauterbeck, J. (2005). The mechanical properties of the human patellar tendon are correlated to its mass density and are independent of sex. *Clinical Biomechanics*, *20*(6), 645–652. https://doi.org/10.1016/j.clinbiomech.2005.02.008

Hewett, T. E., Myer, G. D., & Ford, K. R. (2006). Anterior cruciate ligament injuries in female athletes. *The American Journal Of Sports Medicine*, 34(2), 299–311. https://doi.org/10.1177/0363546505284183

Hicks J. (2012, August 17). *Checklist – Evaluating your Simulation.* Opensim. https://opensimconfluence.atlassian.net/wiki/spaces/OpenSim/pages/53114566/Checklist+-+Evaluating+your+Simulation

Hicks, J. L., Uchida, T. K., Seth, A., Rajagopal, A., & Delp, S. L. (2014). Is My Model Good Enough? Best Practices for Verification and Validation of Musculoskeletal Models and Simulations of Movement. *Journal Of Biomechanical Engineering*, *137*(2). https://doi.org/10.1115/1.4029304

Hirschmann, A., Pfirrmann, C. W. A., Klammer, G., Espinosa, N., & Buck, F. M. (2013). Upright Cone CT of the hindfoot: Comparison of the non-weight-bearing with the upright weight-bearing position. *European Radiology*, *24*(3), 553–558. https://doi.org/10.1007/s00330-013-3028-2

Kewley, A., Beesel, J., & Seth, A. (2025). OpenSim Creator. Zenodo 0.5.23. **https://doi.org/10.5281/zenodo.15525321**

Kumar, D., Manal, K., & Rudolph, K. (2012). Knee joint loading during gait in healthy controls and individuals with knee osteoarthritis. *Osteoarthritis And Cartilage*, *21*(2), 298–305. https://doi.org/10.1016/j.joca.2012.11.008

Lace, K. L. V., & Błażkiewicz, M. (2021). How does the ski boot affect human gait and joint loading? *Biomedical Human Kinetics*, *13*(1), 163–169. https://doi.org/10.2478/bhk-2021-0020

Lai, A. K. M., Arnold, A. S., & Wakeling, J. M. (2017). Why are Antagonist Muscles Co-activated in My Simulation? A Musculoskeletal Model for Analysing Human Locomotor Tasks. *Annals Of Biomedical Engineering*, *45*(12), 2762–2774. https://doi.org/10.1007/s10439-017-1920-7

Lieber, R. L. (2010). *Skeletal muscle structure, function, and plasticity: The physiological basis of rehabilitation* (3rd ed.). Lippincott Williams & Wilkins.

Maarleveld, R., Veeger, H. E. J., van der Helm, F.C.T., Son, J., Lieber, R. L., & van der Kruk E. (2024). What the %PCSA? Addressing diversity in Lower-Limb Musculoskeletal models: age- and sex-related differences in PCSA and muscle mass. *arXiv (Cornell University)*. https://doi.org/10.48550/arxiv.2411.00071

Manal, K., & Buchanan, T. S. (2004). *Subject-Specific Estimates of Tendon Slack Length: A Numerical Method. Journal of Applied Biomechanics, 20(2), 195–203.* doi:10.1123/jab.20.2.195

Mancino, F., Kayani, B., Gabr, A., Fontalis, A., Plastow, R., & Haddad, F. S. (2024). Anterior cruciate ligament injuries in female athletes: risk factors and strategies for prevention. Bone & Joint Open, 5(2), 94–100. https://doi.org/10.1302/2633-1462.52.bjo-2023-0166

Modenese, L., & Kohout, J. (2020). Automated generation of Three-Dimensional complex muscle geometries for use in personalised musculoskeletal models. *Annals of Biomedical Engineering*, *48*(6), 1793–1804. https://doi.org/10.1007/s10439-020-02490-4

Modenese, L., & Renault, J. (2020). Automatic generation of personalised skeletal models of the lower limb from three-dimensional bone geometries. *Journal of Biomechanics, 116, 110186.* https://doi.org/10.1016/j.jbiomech.2020.110186

Modenese, L., Ceseracciu, E., Reggiani, M., & Lloyd, D. G. (2015). Estimation of musculotendon parameters for scaled and subject specific musculoskeletal models using an optimization technique. *Journal of Biomechanics*, *49*(2), 141–148. https://doi.org/10.1016/j.jbiomech.2015.11.006

Modenese, L., Montefiori, E., Wang, A., Wesarg, S., Viceconti, M., & Mazzà, C. (2018). Investigation of the dependence of joint contact forces on musculotendon parameters using a codified workflow for image-based modelling. *Journal Of Biomechanics*, *73*, 108–118. https://doi.org/10.1016/j.jbiomech.2018.03.039

Müftü, S. (2022). Transient analysis of solids and structures. *Finite Element Method: Physics and Solution Methods* (pp. 377–445). https://doi.org/10.1016/b978-0-12-821127-4.00007-4

Nam, Y., & Uhm, H.W. (2011). Tendon Slack Length and its Effect on Muscle Force-Generation Characteristics. *Journal of Mechanics in Medicine and Biology*, 11(02), 445–456. doi:10.1142/s0219519410003770

Paluszek, M. (2023). Attitude dynamics. *ADCS - Spacecraft Attitude Determination and Control* (pp. 65–101). Princeton Satellite Systems https://doi.org/10.1016/b978-0-32-399915-1.00017-6

Paulsen F., & Waschke J. (2018). *Sobotta: Altas van de menselijke anatomie, deel 1* (5th ed.) Bohn Stafleu van Loghum.

Peate, I. (2018). Anatomy and physiology, 5. The musculoskeletal system. *British Journal of Healthcare Assistants, 12(1), 6–9.* doi:10.12968/bjha.2018.12.1.6

Pizzolato, C., Reggiani, M., Modenese, L., & Lloyd, D. G. (2016). Real-time inverse kinematics and inverse dynamics for lower limb applications using OpenSim. *Computer Methods in Biomechanics & Biomedical Engineering*, *20*(4), 436–445. https://doi.org/10.1080/10255842.2016.1240789

Rajagopal, A., Dembia, C. L., DeMers, M. S., Delp, D. D., Hicks, J. L., & Delp, S. L. (2016). Full-Body musculoskeletal model for Muscle-Driven simulation of human GaIT. *IEEE Transactions on Biomedical Engineering,* 63(10), 2068–2079. https://doi.org/10.1109/tbme.2016.2586891

Renstrom, P., Ljungqvist, A., Arendt, E., et al. (2008). Non-contact ACL injuries in female athletes: An International Olympic Committee current concepts statement. British Journal of Sports Medicine, 42(6), 394-412.

Savoji, K., Soleimani, M., & Moshayedi, A. J. (2024). A Comprehensive Review of Electromyography in Rehabilitation: Detecting Interrupted Wrist and Hand Movements with a Robotic Arm Approach. *EAI Endorsed Transactions On AI And Robotics*, 3. https://doi.org/10.4108/airo.7377

Schwartz, M. (2012). EMG Methods for Evaluating Muscle and Nerve Function. In *InTech eBooks*. https://doi.org/10.5772/1465

Shelton, T. J., Singh, S., Robinson, E. B., Nardo, L., Escobedo, E., Jackson, L., Kreulen, C. D., & Giza, E. (2018). The Influence of Percentage Weight-Bearing on Foot Radiographs. *Foot & Ankle Specialist*, *12*(4), 363–369. https://doi.org/10.1177/1938640018810412SimTK (n.d.). Three-dimensional muscle geometries for subject-specific models. Retrieved February 27, 2025 from https://simtk.org/projects/3d-muscles

Smith, F. W., & Smith, P. A. (2002). Musculoskeletal Differences Between Males and Females. *Sports Medicine And Arthroscopy Review*, *10*(1), 98–100. https://doi.org/10.1097/00132585-200210010-00014

Smith, G. I., & Mittendorfer, B. (2015). Sexual dimorphism in skeletal muscle protein turnover. *Journal Of Applied Physiology*, *120*(6), 674–682. https://doi.org/10.1152/japplphysiol.00625.2015

Smith, S. H., Coppack, R. J., Van Den Bogert, A. J., Bennett, A. N., & Bull, A. M. (2021). Review of musculoskeletal modelling in a clinical setting: Current use in rehabilitation design, surgical decision making and healthcare interventions. *Clinical Biomechanics*, *83*, 105292. https://doi.org/10.1016/j.clinbiomech.2021.105292

Son, J., Ward, S. R., & Lieber, R. L. (2024). Scaling relationships between human leg muscle architectural properties and body size. *Journal Of Experimental Biology*, *227*(6). https://doi.org/10.1242/jeb.246567

Stein, M. J., Fischer, B., Bohmann, P., Ahrens, W., Berger, K., Brenner, H., Günther, K., Harth, V., Heise, J., Karch, A., Klett-Tammen, C. J., Koch-Gallenkamp, L., Krist, L., Lieb, W., Meinke-Franze, C., Michels, K. B., Mikolajczyk, R., Nimptsch, K., Obi, N., . . . Sedlmeier, A. M. (2024). Differences in anthropometric measures based on sex, age, and health status: Findings from the German National Cohort (NAKO). *Deutsches Ärzteblatt International*. https://doi.org/10.3238/arztebl.m2024.0016

Sylvester, A. D., Lautzenheiser, S. G., & Kramer, P. A. (2021). A review of musculoskeletal modelling of human locomotion. *Interface Focus*, *11*(5), 20200060. https://doi.org/10.1098/rsfs.2020.0060The MathWorks Inc. (2023). MATLAB version: 9.13.0 (R2023b), Natick, Massachusetts: The MathWorks Inc. https://www.mathworks.com

Uhlrich, S. D., Jackson, R. W., Seth, A., Kolesar, J. A., & Delp, S. L. (2022). Muscle coordination retraining inspired by musculoskeletal simulations reduces knee contact force. *Scientific Reports*, *12*(1). https://doi.org/10.1038/s41598-022-13386-9

Valdez, G. (2019). Effects of disease-afflicted and aging neurons on the musculoskeletal system. *Bone*, *122*, 31–37. https://doi.org/10.1016/j.bone.2019.01.023

Valente, G. (2013). Subject-specific musculoskeletal models of the lower limbs for the prediction of skeletal loads during motion. https://doi.org/10.6092/unibo/amsdottorato/5561

Vallery, H., & Schwab, A. (2020). *Advanced Dynamics* (3rd ed). Stichting Newton-Euler, Delft

Van de Meerakker, W. F. (2025). Development of an Automatic MRI-based Segmentation Model to analyze Sex-related Differences in the Lower Extremity Musculoskeletal System. [Published master's thesis, TU Delft]. Repository TU Delft. Development of an MRI-based Automatic Segmentation Model to analyze Sex-Related Differences in the Lower-extremity Musculoskeletal System | TU Delft Repository

Wesseling, M., De Groote, F., Bosmans, L., Bartels, W., Meyer, C., Desloovere, K., & Jonkers, I. (2016a). *Subject-specific geometrical detail rather than cost function formulation affects hip loading calculation. Computer Methods in Biomechanics and Biomedical Engineering, 19(14), 1475–1488.* doi:10.1080/10255842.2016.1154547

Wesseling, M., De Groote, F., Meyer, C., Corten, K., Simon, J.-P., Desloovere, K., & Jonkers, I. (2016b). *Subject-specific musculoskeletal modelling in patients before and after total hip arthroplasty. Computer Methods in Biomechanics and Biomedical Engineering, 19(15), 1683–1691.* doi:10.1080/10255842.2016.1181174

Winby, C., Lloyd, D., & Kirk, T. (2008). Evaluation of different analytical methods for subject-specific scaling of musculotendon parameters. *Journal of Biomechanics*, *41*(8), 1682–1688. https://doi.org/10.1016/j.jbiomech.2008.03.008

Yoganandan, N., Arun, M. W., Dickman, C. A., & Benzel, E. C. (2017). Practical Anatomy and Fundamental Biomechanics. Benzel's Spine Surgery, 2_Volume Set: Techniques, *Complication Avoidance and Management (pp. 58-82.e2).* https://doi.org/10.1016/b978-0-323-40030-5.00007-1

Zhang C., & Chen T. (2001). Efficient feature extraction for 2D/3D objects in mesh representation. *Proceedings 2001 International Conference on Image Processing (Cat. No.01CH37205)*, pp. 935-938 vol.3, doi: 10.1109/ICIP.2001.958278.

Appendix

Appendix A: Nomenclature

Abbreviation	Definition
ACL	Anterior Cruciate Ligament
COM	Center of Mass
$F_{iso,max}$	Maximum Isometric Force
ID	Inverse Dynamics
IK	Inverse Kinematics
JRF	Joint Reaction Force
MR	Magnetic Resonance
OFL	Optimal fiber length
PA_{ofl}	Pennation Angle at optimal fiber length
PCSA	Physiological Cross-Sectional Area
RMS	Root Mean Square
RAJAG	Rajagopal model
SD	Standard Deviation
SO	Static Optimization
SPM	Statistical Parametric Mapping
YONI	Female model named YONI

Appendix B: Euclidean distance analysis

Table A: Euclidean Distance Analysis

Participant	Age	Height (cm)	Z-score height	Weight (kg)	Z-score weight	Body fat (%)	Z-score body fat %	Euclidean Distance
002	29	171	-0.442091663	64.5	0.174913	34.3	1.094151	1.245306
003	26	174	0.289646262	57.9	-0.99412	22.5	-1.37685	3.023484
004	27	180	1.753122111	68.3	0.847995	33.3	0.884744	3.127129
005	30	169	-0.807960625	72.5	1.591928	36.2	1.492024	1.426137
006	31	165.5	-1.783611811	55.5	-0.51828	26.6	-1.41923	2.430637
013	24	172	-0.198179021	63.4	-0.01993	25.4	-0.76957	1.856898
0.16	26	174	0.41	6.20	0.83	30	0.193701	1.778557
017	32	176.00	0.78	57.80	-1.01	324.30	-0.999992	.128763
Std		4.099828503		5.64567		4.775393		
Gem		172.8125		63.5125		29.075		
Reference		167.3		67.8		31.3		
Reference z score		-1.344568437		0.759432		0.46593		

The z-scores were calculated with: $Z_{score} = \frac{x-\bar{x}}{std}$

where std is the standard deviation.

The Euclidean distance (ED) was calculated as:

$$ED = \sqrt{(z_{score,1} - z_{score,ref,1})^2 + (z_{score,2} - z_{score,ref,2})^2 + (z_{score,3} - z_{score,ref,3})^2}$$

The subject with the smallest ED was chosen as the basis for the model.

Appendix C: Preprocessing data

Figure C.1: Planes used to define segments using planes based on joints.

Appendix D: Inertial Parameters

Appendix D.1: STAPLE graphs

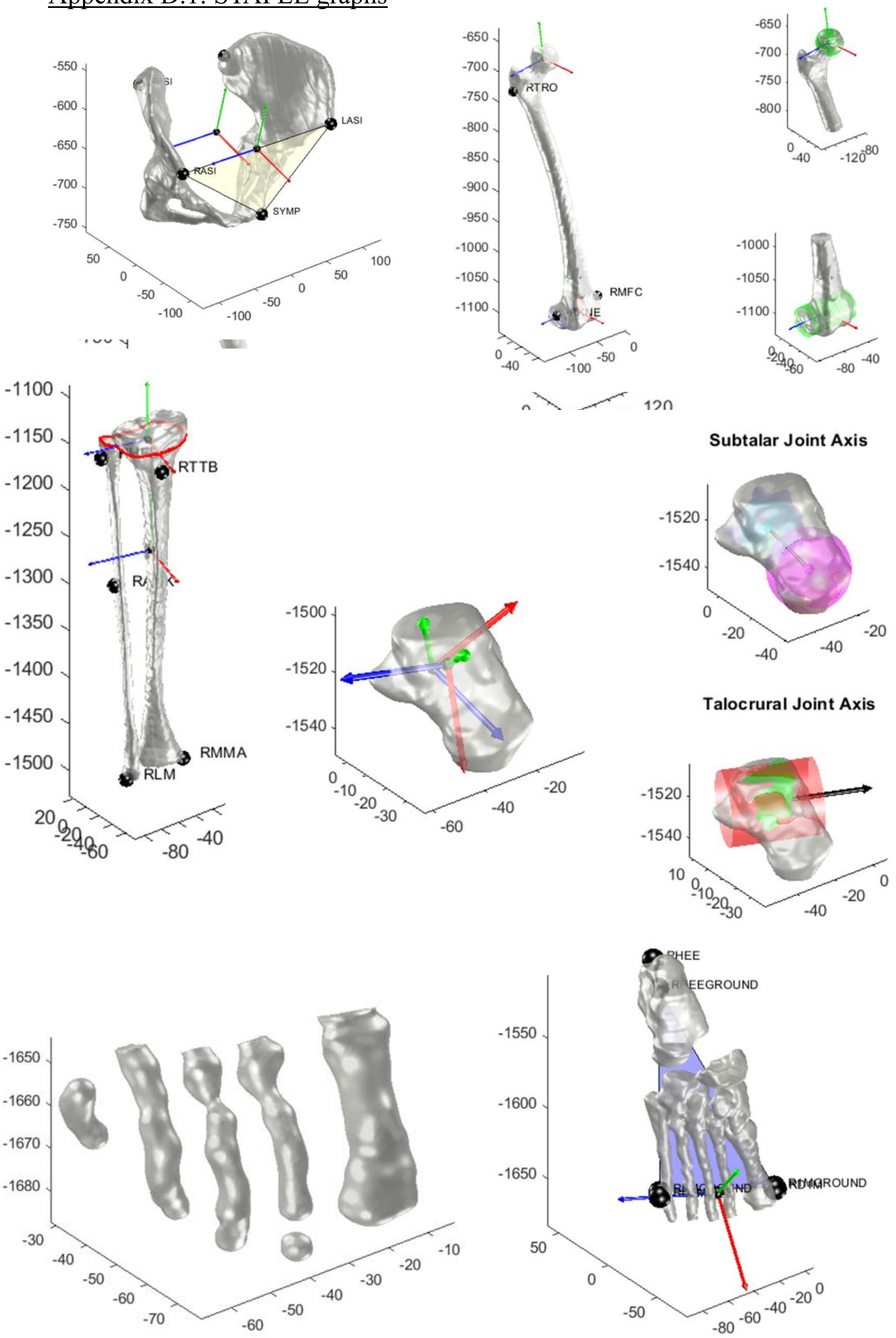

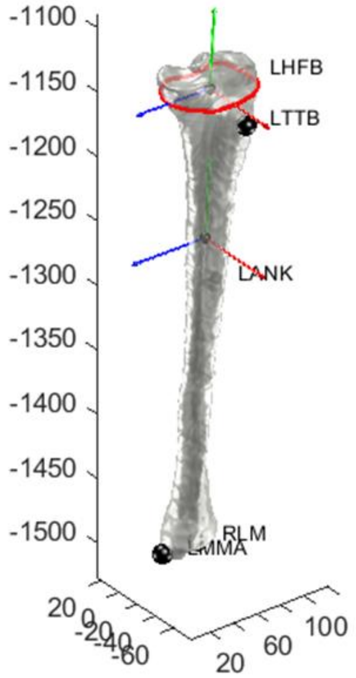
LHFB
LTTB
LANK
RLM
LMMA

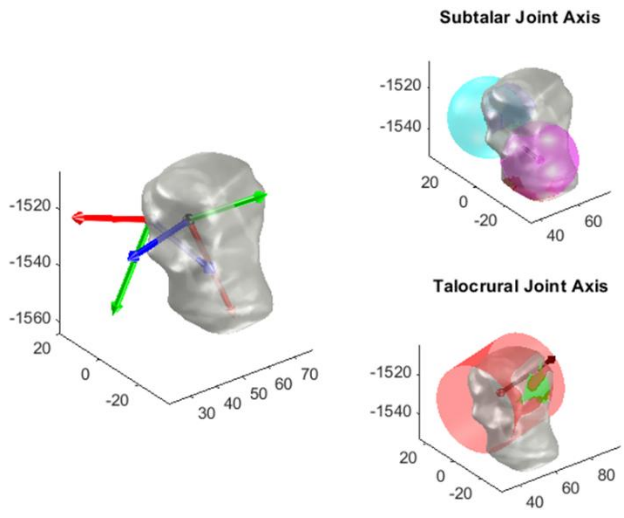
Subtalar Joint Axis
Talocrural Joint Axis

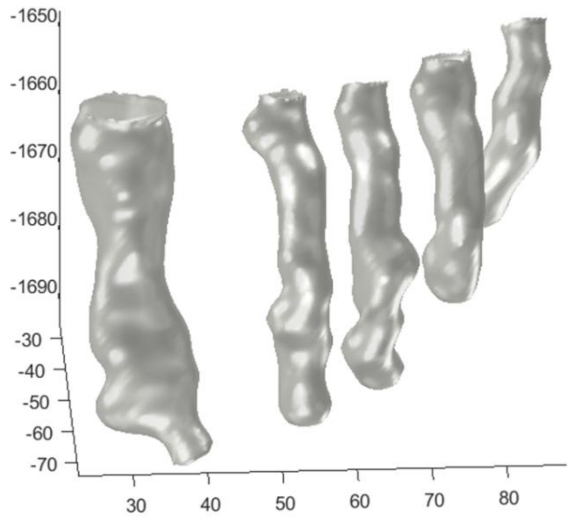

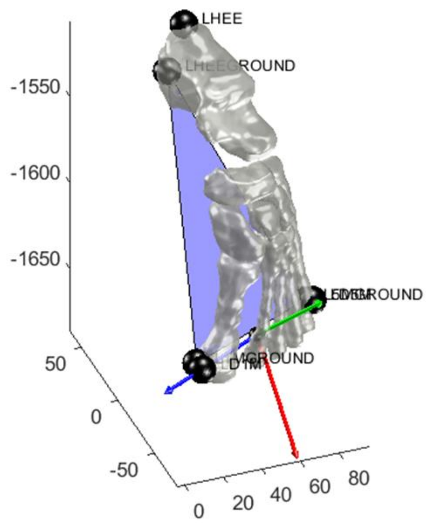
LHEE

Appendix D.2: Density

Table D.2.1: Overview density literature

Publication	**Sex**	**Number of participants**	**Age**	**Bone density (g/cm^3)**	**Muscle density (g/cm^3)**	**Skin density (g/cm^3)**	**Fat density (g/cm^3)**	**Segment density (g/cm^3)**
Martin, Mungiole, Marzke, & Longhill (1989)	Baboons (not humans)	-	-	1.705	1.067	-	-	1.124
Clauser, McConville & Young (1969)	Men (cadaver)	135	39-55yr	1.800 (compact), 1.105 (cancellous)	1.087	1.102	0.961	-
Meema & Meema (1978)	Women	56 58	20-29 30-39	1.186 (cortical) 1.179 (cortical)	-	-	-	-
Novak et al. (2020)	Women	23	19.2-27.6 yr	1.152 (cortical)	0.0771	-	-	-
Dempster & Gaughran (1967)	Men (cadaver)	61	52-83 yr	-	-	-	-	Whole body: 1.003 Thigh: 1.0401 Shank: 1.0789 Foot: 1.0664
Erdmann & Gos (1990)	Men and women (cadaver)	50	20-40 yr	-	1.178	1.125	0.938 (subcutaneous)	-
Baker et al. (2014)	Men and women	239 M and 261 W	21-78 yr	-	0.0746	-	-	-
Ward & Lieber (2005)	-	3 living, 6 cadaver	Living: 59 gem, cadaver: 78 gem.	-	1.055-1.112	-	-	-
Drillis, Contini & Bluestein (1964)	Female	2 cadavers	-	-	-	-	-	Thigh: 1.0686 Shank: 1.1102 Foot: 1.0893
Erdmann (1997)	Men	15	20-40 yr	-	-	-	-	Pelvis: 1.077 Muscle, fat, skin pelvis: 1.035

Mendez & Keys (1960) [1]	Canine and Rabbit	-	-	-	1.0597	-	-	-
Drillis & Continni (1966) [2]	Men	12	'young'	-	-	-	-	Thigh: 1.089 Calf: 1.095 Foot: 1.107

[1]: Mentioned in Ward & Lieber (2005), but no access (and hard to find). Mendez, J. and Keys, A. (1960) Density and Composition of Mammalian Muscle. Metabolism, 9, 184-188.

[2]: Mentioned in Clauser et al. (1969), but no access (and hard to find). Drillis, Rudolfs and Renato Contini. 1966.Body Segment Parameters, Office of Vocational Rehabilitation, Department of Health, E

A short literature search was done to determine which density values should be used for different tissue types in this study. The results can be shown in Table I.

For bone density 1.186 g/cm^3 was chosen (Meema & Meema, 1978), because this study looked at only women and in the same age category as the chosen subject.

For muscle density, the preferred value of the study of Novak et al. (2020) was preferred, as this study looked at only women, with an age category matching the most to the selected subject in this study. However, it was believed that the value of 0.0771 g/cm^3 was too low, and should be at least bigger than the fat density value. The mean value of the muscle densities of the remaining studies was taken (excluding Novak et al., and Baker et al. (2014) and was 1.095 g/cm3 (only humans).

Only two studies looked at both fat and skin densities. One of the two studies looked at both female and male (cadaver) subjects and was therefore chosen for this study. As the bigger part of this part of the segment (fat/skin) will be fat, the density of fat was taken. The specific value of 0.938 g/cm3 was taken from Erdmann & Gos (1990), because this study also included women.

Baker, J. F., Von Feldt, J., Mostoufi-Moab, S., Noaiseh, G., Taratuta, E., Kim, W., & Leonard, M. B. (2014). Deficits in muscle mass, muscle density, and modified associations with fat in rheumatoid arthritis. *Arthritis Care & Research*, *66*(11), 1612–1618. https://doi.org/10.1002/acr.22328

Clauser C.E., McConville J.T., & Young J.W. (1969). Weight, volume, and center of mass of segments of the human body. Aerospace Medical Research Labs, NASA. https://ntrs.nasa.gov/citations/19700027497 (at page 96)

Dempster, W. T., & Gaughran, G. R. L. (1967). Properties of body segments based on size and weight. *American Journal of Anatomy*, *120*(1), 33–54. https://doi.org/10.1002/aja.1001200104

Drillis, Contini, & Bluestein (1964). Body segment parameters: a survey of measurements techniques. *Artificial limbs*.

Erdmann (1997). Geometric and inertial data of the trunk in adult males. *Journal of Biomechanics, 30(17), 679-688.* https://doi.org/10.1016/S0021-9290(97)00013-4

Erdmann W.S., & Gos T. (1990). Density of trunk tissues of young and medium age people. *Journal of Biomechanics, 23(9), 945-947.* https://doi.org/10.1016/0021-9290(90)90360-F

Martin P.E., Mungiole M., Marzke M.W, & Longhill J.M. (1989). The use of magnetic resonance imaging for measuring segment inertial properties. *Journal of Biomechanics, 22(4), 367-369, 371-376.* https://www.sciencedirect.com/science/article/pii/0021929089900511

Meema, H. E., & Meema, S. (1978). Compact bone mineral density of the normal human radius. *Acta Radiologica Oncology Radiation Physics Biology*, *17*(4), 342–352. https://doi.org/10.3109/02841867809127938

Novak, D., Forsander, G., Kristiansen, E., Svedlund, A., Magnusson, P., & Swolin-Eide, D. (2020). Altered cortical bone strength and lean mass in young women with long-duration (19 years) type 1 diabetes. *Scientific Reports*, *10*(1). https://doi.org/10.1038/s41598-020-78853-7

Ward S.R., & Lieber R.L., (2005). Density and hydration of fresh and fixed human skeletal muscle. *Journal of Biomechanics, 38(11), 2317-2320.* https://doi.org/10.1016/j.jbiomech.2004.10.001

Appendix D.3: Plots of COM

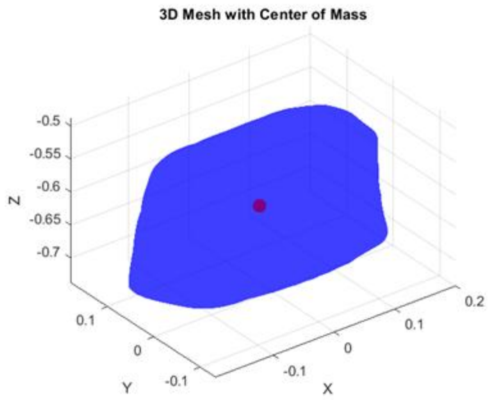

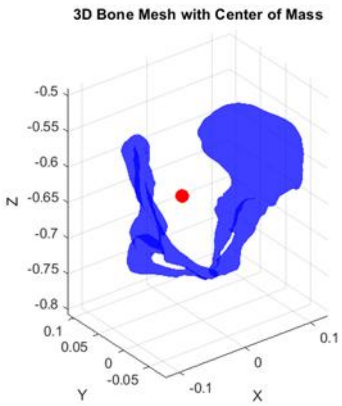

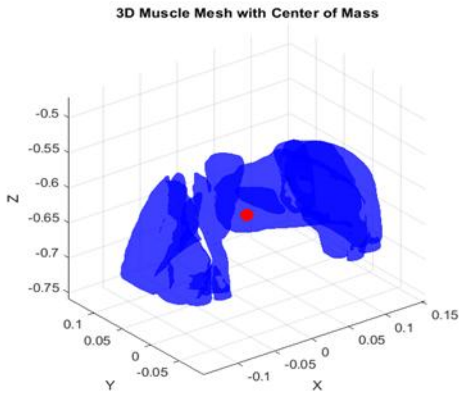

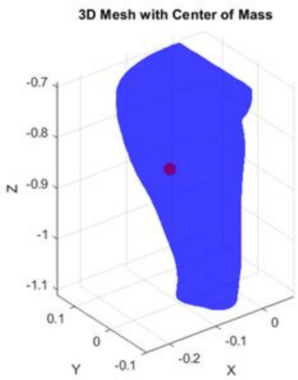

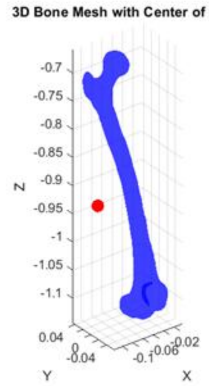

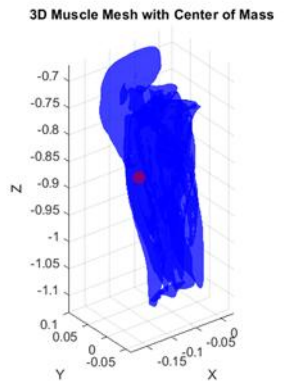

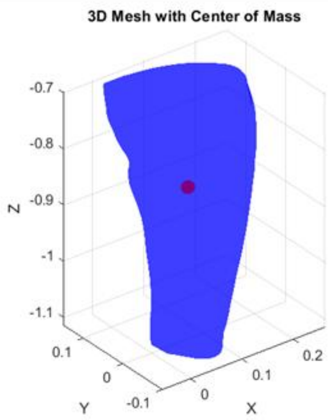

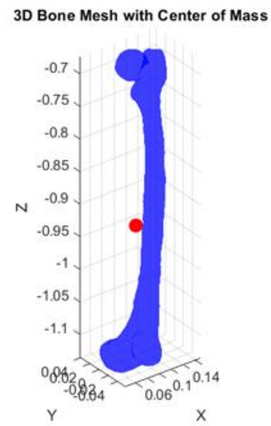

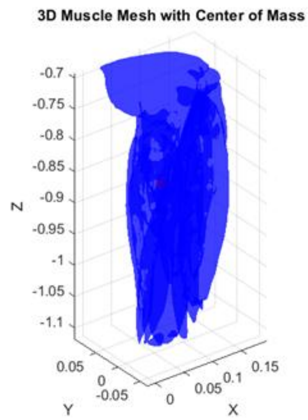

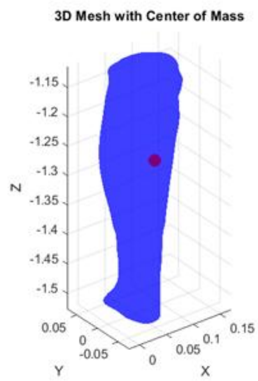

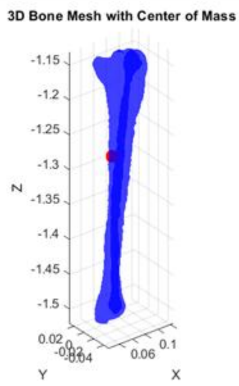

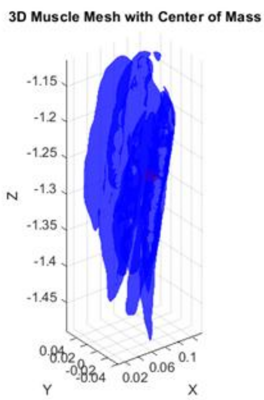

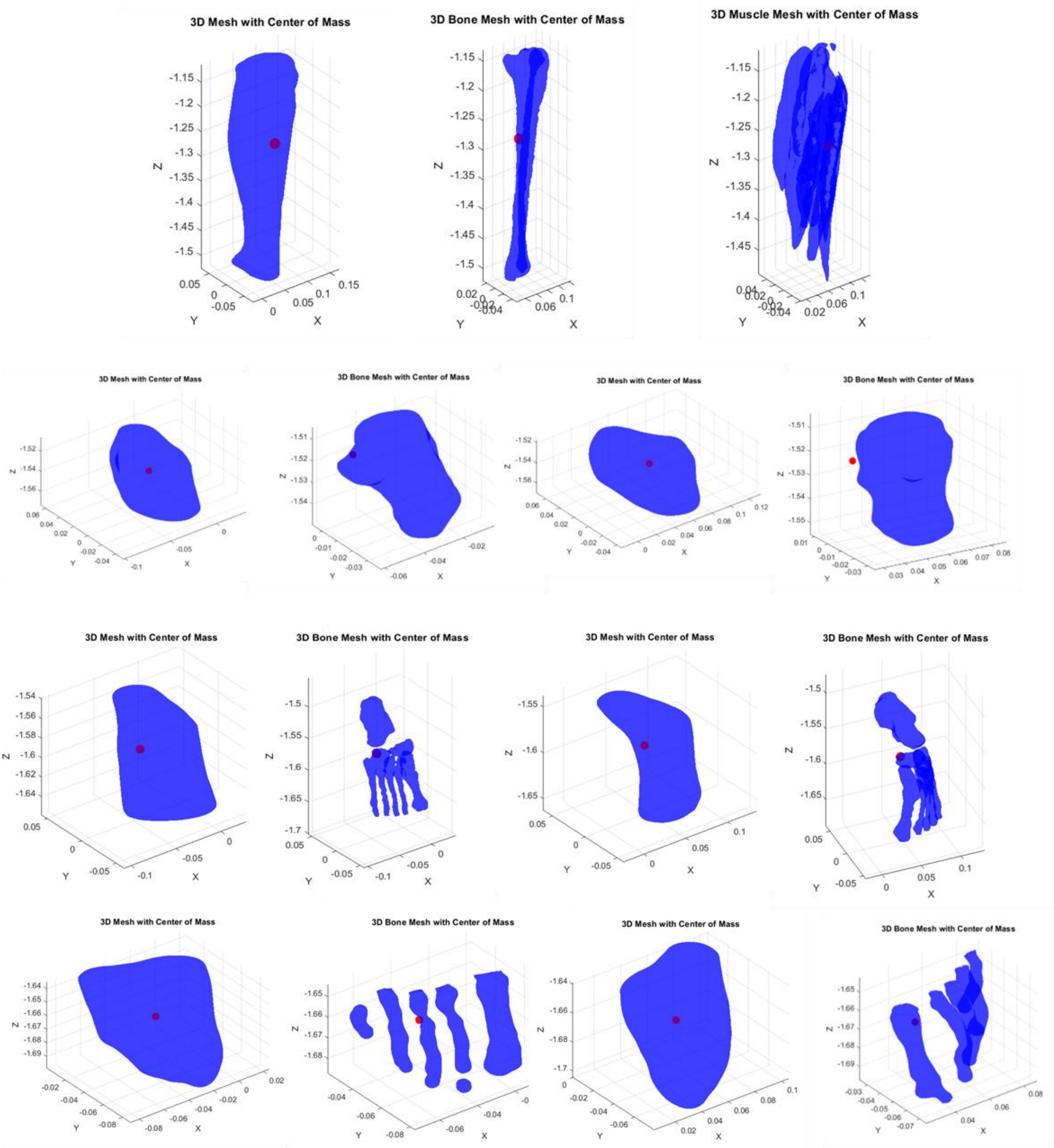
3D Mesh with Center of Mass
3D Bone Mesh with Center of Mass
3D Muscle Mesh with Center of Mass
3D Mesh with Center of Mass
3D Bone Mesh with Center of Mass
3D Mesh with Center of Mass
3D Bone Mesh with Center of Mass
3D Mesh with Center of Mass
3D Bone Mesh with Center of Mass
3D Mesh with Center of Mass
3D Bone Mesh with Center of Mass
3D Mesh with Center of Mass
3D Bone Mesh with Center of Mass
3D Mesh with Center of Mass
3D Bone Mesh with Center of Mass
X
Y
Z

Appendix E: Geometrical Parameters

Appendix E.1: Wrapping spheres

The method of Wesseling et al. (2016) was adopted. Muscle points were annotated in the MRI images. For the wrapping spheres nine points were annotated for the line of action of the m. iliacus and m. psoas major. which are shown in Figure D.1.1 (left) Figure D.1.2, and Figure D.1.3 respectively. The muscle points for the right iliacus sphere were changed to visualize the muscle path better in the model, which is seen on the right side of Figure D.1.1.

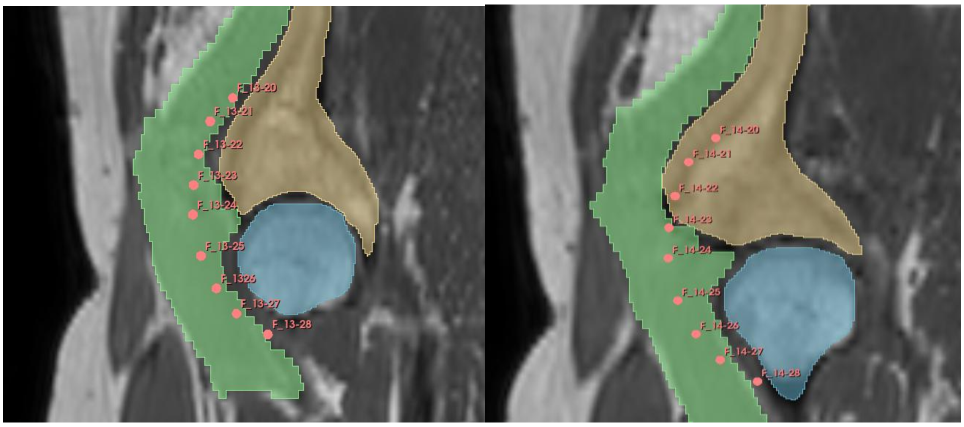

Figure E.1.1: Muscle points for the left m. iliacus.

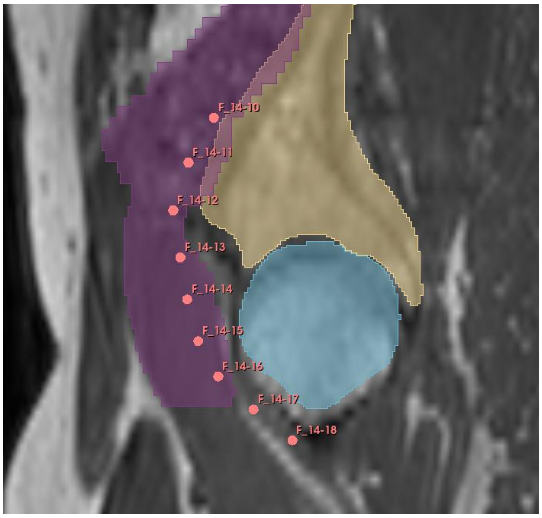

Figure E.1.2: Muscle points of the right m. iliacus

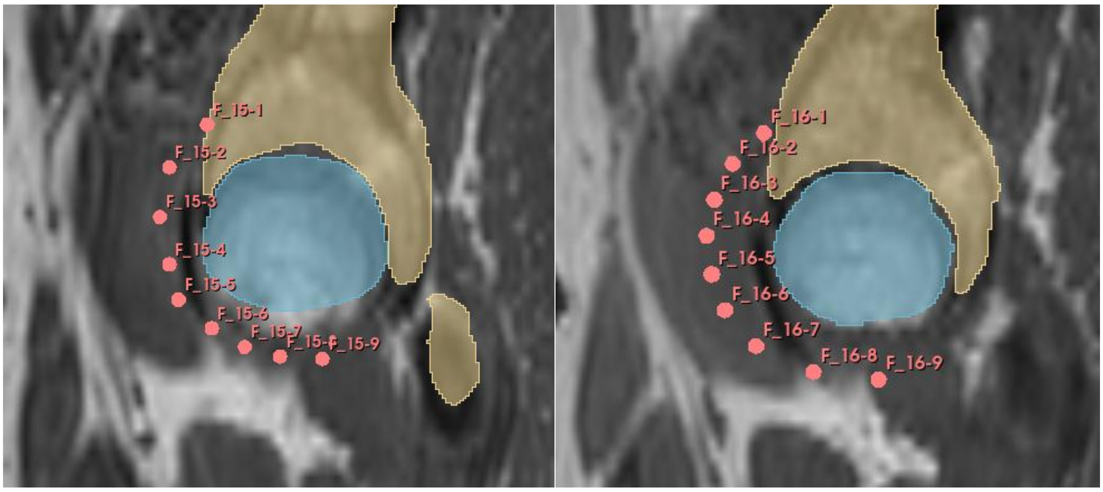

Figure E.1.3: Muscle points for the left and right m. psoas major.

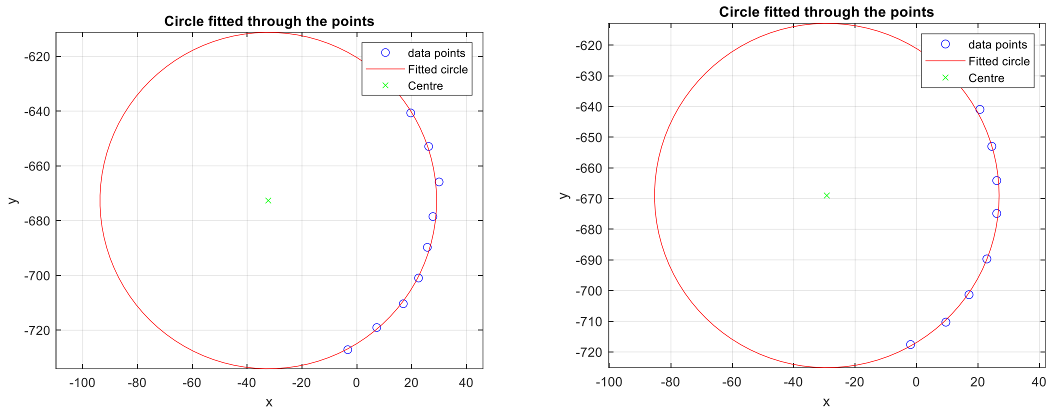

Figure E.1.4: Circle fitted through points of iliacus. Left: Iliacus left. Right: Iliacus right.

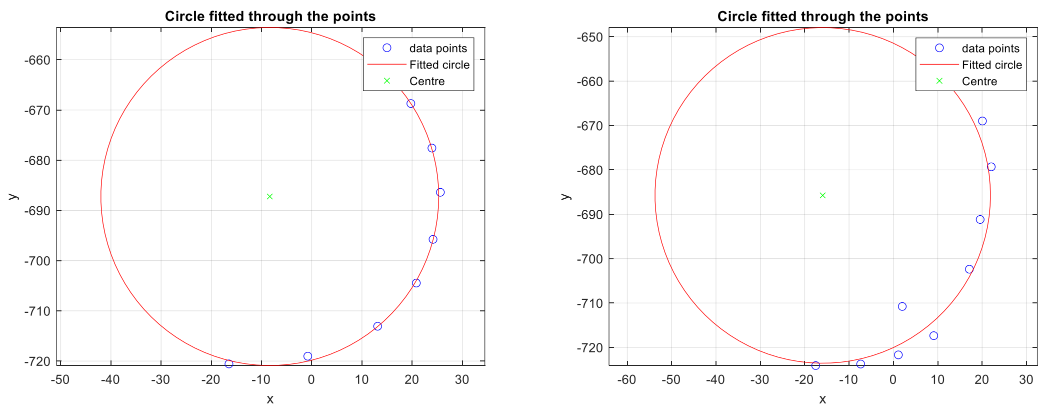

Figure E.1.5: Circles fitted through points of psoas. Left: Psoas right. Right: Psoas left

Appendix E.2: Toe marker

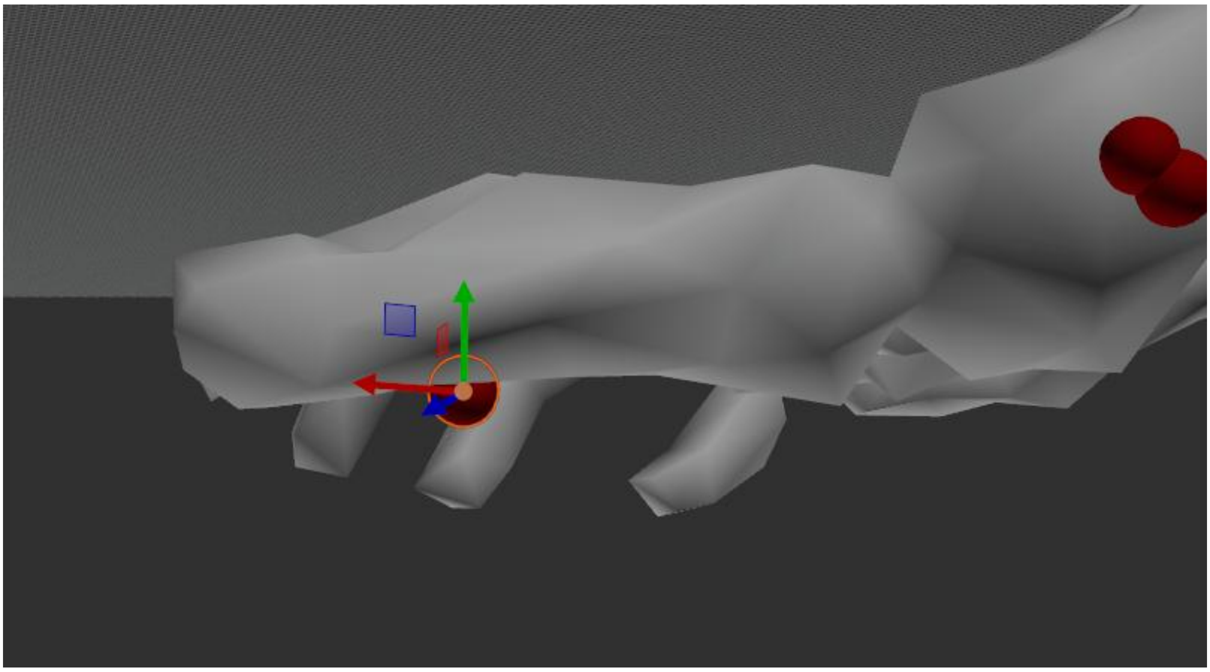

Appendix F: Muscle parameters

Appendix F.1: Muscle parameters

Table F.1.1: Muscle parameters in the female model

Muscles	Abbriaviation	Volume	PCSA	Fiso,max	OFL	TSL	PA,ofl
m. adductor brevis	addbrev_r	86,955687500	7,232685734	433,9611	0,120226	0,032	0,114781
	addbrev_l	86,955687500	9,998814192	599,9289	0,086966	0,0642	0,114781
m. adductor longus	addlong_r	100,144640625	9,750897308	585,0538	0,102703	0,1641	0,13777
	addlong_l	79,248968750	7,559327783	453,5597	0,104836	0,1631	0,13777
m. adductor magnusDist.	addmagDist_r	328,680312500	17,49378939	1049,627	0,187884	0,1177	0,194705
	addmagDist_l	309,354375000	125, 9073565	7554,441	0,02457	0,279	0,194705
m. adductor magnusIsch.	addmagIsch_r	328,680312500	24,96735989	1498,042	0,131644	0,2754	0,168044
	addmagIsch_l	309,354375000	86,09918592	5165,951	0,03593	0,3721	0,168044
m. adductor magnusMid	addmagMid_r	328,680312500	18,61399347	1116,84	0,176577	0,006	0,207308
	addmagMid_l	309,354375000	27,60613734	1656,368	0,11206	0,071	0,207308
m. adductor magnusProx	addmagProx_r	328,680312500	36,85335282	2211,201	0,089186	0,0183	0,311483
	addmagProx_l	309,354375000	50,98379534	3059,028	0,060677	0,054	0,311483
m. biceps femoris longus	bflh_r	155,235359375	28,07149356	1684,29	0,0553	0,367268	0,175918
	bflh_l	161,750343750	26,65672535	1599,404	0,060679	0,3693	0,175918
m. biceps femoris brevis	bfsh_r	73,346898438	6,168685004	370,1211	0,118902	0,1181	0,264223
	bfsh_l	59,092289062	5,061524742	303,6915	0,116748	0,1131	0,264223
m. extensor digitorum longus	edl_r	37,695113281	12,12958564	727,7751	0,031077	0,501	0,218258
	edl_l	32,955078125	6,913749449	414,825	0,047666	0,4838	0,218258
m. extensor hallucis longus	ehl_r	42,708390625	7,801046747	468,0628	0,054747	0,3641	0,197268
	ehl_l	41,530839844	13,03378102	782,0269	0,031864	0,3814	0,197268
m. flexor digitorum longus	fdl_r	29,649605469	4,826803436	289,6082	0,061427	0,45657	0,224839
	fdl_l	31,575128906	5,789246421	347,3548	0,054541	0,4566	0,224839
m. flexor hallucis longus	fhl_r	62,910832031	12,52629911	751,5779	0,050223	0,4985	0,258025
	fhl_l	33,925597656	4,957128738	297,4277	0,068438	0,4613	0,258025
m. gastrocnemius lateralis	gaslat_r	101,517906250	14,74779276	884,8676	0,068836	0,4065	0,210227
	gaslat_l	119,737796875	17,50117615	1050,071	0,068417	0,4079	0,210227
m. gastrocnemius medialis	gasmed_l	235,251812500	39,59268446	2375,561	0,059418	0,4257	0,165682
	gasmed_r	228,455375000	38,28839643	2297,304	0,059667	0,4214	0,165682
m. gluteus maximus 1	glmax1_r	816,235062500	52,2326925	3133,962	0,156269	0,028	0,354012
	glmax1_l	788,937312500	116,4655023	6987,93	0,06774	0,1157	0,354012
m. gluteus maximus 2	glmax2_r	816,235062500	56,41112019	3384,667	0,144694	0,0524	0,367382
	glmax2_l	788,937312500	53,62214876	3217,329	0,147129	0,0809	0,367382
m. gluteus maximus 3	glmax3_r	816,235062500	58,38841885	3503,305	0,139794	0,11665	0,382416
	glmax3_l	788,937312500	68,77068624	4126,241	0,11472	0,1353	0,382416
m. gluteus medius 1	glmed1_r	279,294281250	41,8788564	2512,731	0,066691	0,0634	0,316556
	glmed1_l	285,767468750	56,00209076	3360,125	0,051028	0,0671	0,316556
m. gluteus medius 2	glmed2_r	279,294281250	96,81917747	5809,151	0,028847	0,0815	0,316556
	glmed2_l	285,767468750	49,12964081	2947,778	0,058166	0,0556	0,316556
m. gluteus medius 3	glmed3_r	279,294281250	121,4587003	7287,522	0,022995	0,0792	0,316556
	glmed3_l	285,767468750	57,51815888	3451,09	0,049683	0,0376	0,316556

m. gluteus minimus 1	glmin1_r	84,637164062	9,220839541	553,2504	0,091789	0,057	0,174533
	glmin1_l	84,503132812	9,89312691	593,5876	0,085416	0,055	0,174533
m. gluteus minimus 2	glmin2_r	84,637164062	12,73773652	764,2642	0,066446	0,0168	0
	glmin2_l	84,503132812	15,39331332	923,5988	0,054896	0,0353	0
m. gluteus minimus 3	glmin3_r	84,637164062	41,42585486	2485,551	0,020431	0,0331	0,017453
	glmin3_l	84,503132812	36,60679813	2196,408	0,023084	0,03539	0,017453
m. gracilis	grac_r	92,337578125	8,476625613	508,5975	0,108932	0,347	0,172002
	grac_l	95,678382812	3,958019088	237,4811	0,241733	0,2142	0,172002
m. iliacus	iliacus_r	120,358968750	12,72414593	763,4488	0,094591	0,129	0,279914
	iliacus_l	117,224523438	12,93140985	775,8846	0,090651	0,090651	0,133
m. peroneus brevis	perbrev_r	16,759062500	4,425652926	265,5392	0,037868	0,29259	0,205236
	perbrev_l	21,461802734	2,888028035	173,2817	0,074313	0,074313	0,25046
m. peroneus longus	perlong_r	86,642421875	21,41698724	1285,019	0,040455	0,42189	0,247952
	perlong_l	75,618148438	13,02840207	781,7041	0,058041	0,38559	0,247952
m. piriformis	piri_r	22,016896484	34,75986183	2085,592	0,006334	0,084	0,174533
	piri_l	19,128160156	16,33628846	980,1773	0,011709	0,08817	0,174533
m. psoas	psoas_r	78,642820312	7,293357969	437,6015	0,107828	0,0702	0,215525
	psoas_l	59,881097656	7,42370604	445,4224	0,080662	0,107	0,215525
m. rectus femoris	recfem_r	179,474250000	68,67461927	4120,477	0,026134	0,51435	0,217015
	recfem_l	163,555218750	50,60808799	3036,485	0,032318	0,5166	0,217015
m. sartorius	sar_r	109,683421875	3,232409788	193,9446	0,339324	0,2358	0,052578
	sar_l	113,468632812	4,417270377	265,0362	0,256875	0,2928	0,052578
m. semimembranosus	semimem_r	162,411703125	218,7363005	13124,18	0,007425	0,43002	0,254561
	semimem_l	172,150687500	64,7134379	3882,806	0,026602	0,3841	0,254561
m. semitendinosus	semiten_r	124,149070312	15,6463471	938,7808	0,079347	0,3185	0,241295
	semiten_l	112,346484375	15,67618072	940,5708	0,071667	0,3277	0,241295
m. soleus	soleus_r	373,124031250	84,77586878	5086,552	0,044013	0,33855	0,381429
	soleus_l	332,033437500	84,52344207	5071,407	0,039283	0,3509	0,381429
m. tensor fascia latae	tfl_r	56,764414062	6,783510285	407,0106	0,08368	0,4484	0,05236
	tfl_l	43,525066406	15,35492359	921,2954	0,028346	0,5049	0,05236
m. tibialis anterior	tibant_r	114,863281250	26,48877643	1589,327	0,043363	0,3941	0,195183
	tibant_l	89,729734375	15,49254711	929,5528	0,057918	0,3755	0,195183
m. tibialis posterior	tibpost_r	43,060031250	8,758981967	525,5389	0,049161	0,34581	0,226489
	tibpost_l	67,589023438	14,72848626	883,7092	0,04589	0,34363	0,226489
m. vastus intermedius	vasint_r	57,105570312	3,343906913	200,6344	0,170775	0,3226	0,0631
	vasint_l	332,950718750	19,78751827	1187,251	0,168263	0,328	0,0631
m. vastus lateralis	vaslat_r	567,244625000	35,88951965	2153,371	0,158053	0,344	0,252867
	vaslat_l	537,405875000	29,36644126	1761,986	0,183	0,34	0,252867
m. vastus medialis	vasmed_r	389,966343750	22,75806923	1365,484	0,171353	0,3232	0,422223
	vasmed_l	358,639437500	21,73572348	1304,143	0,165	0,322	0,422223

Appendix F.2: Plots normalized fiber lengths

Green: Rajagopal model White: Yoni model

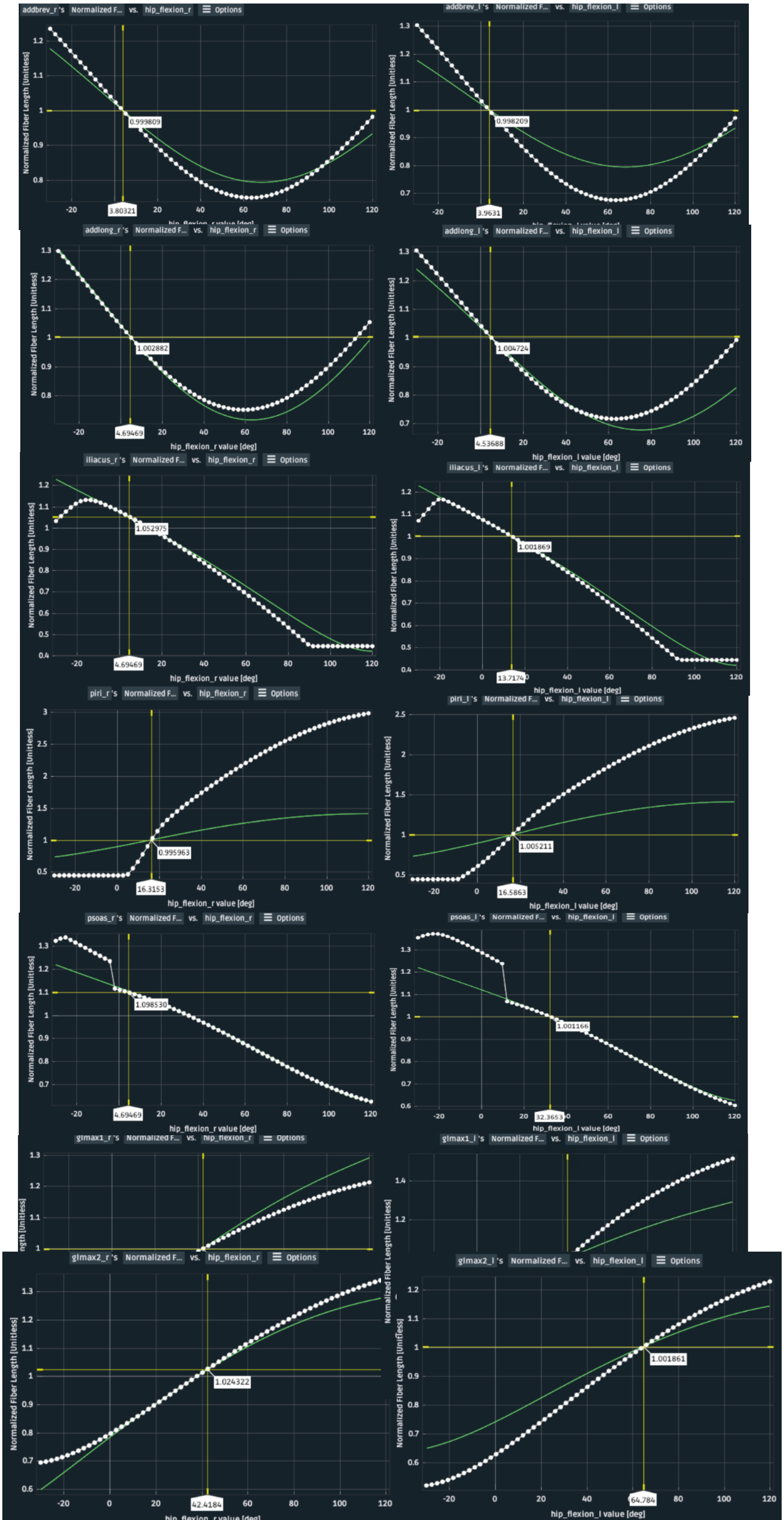

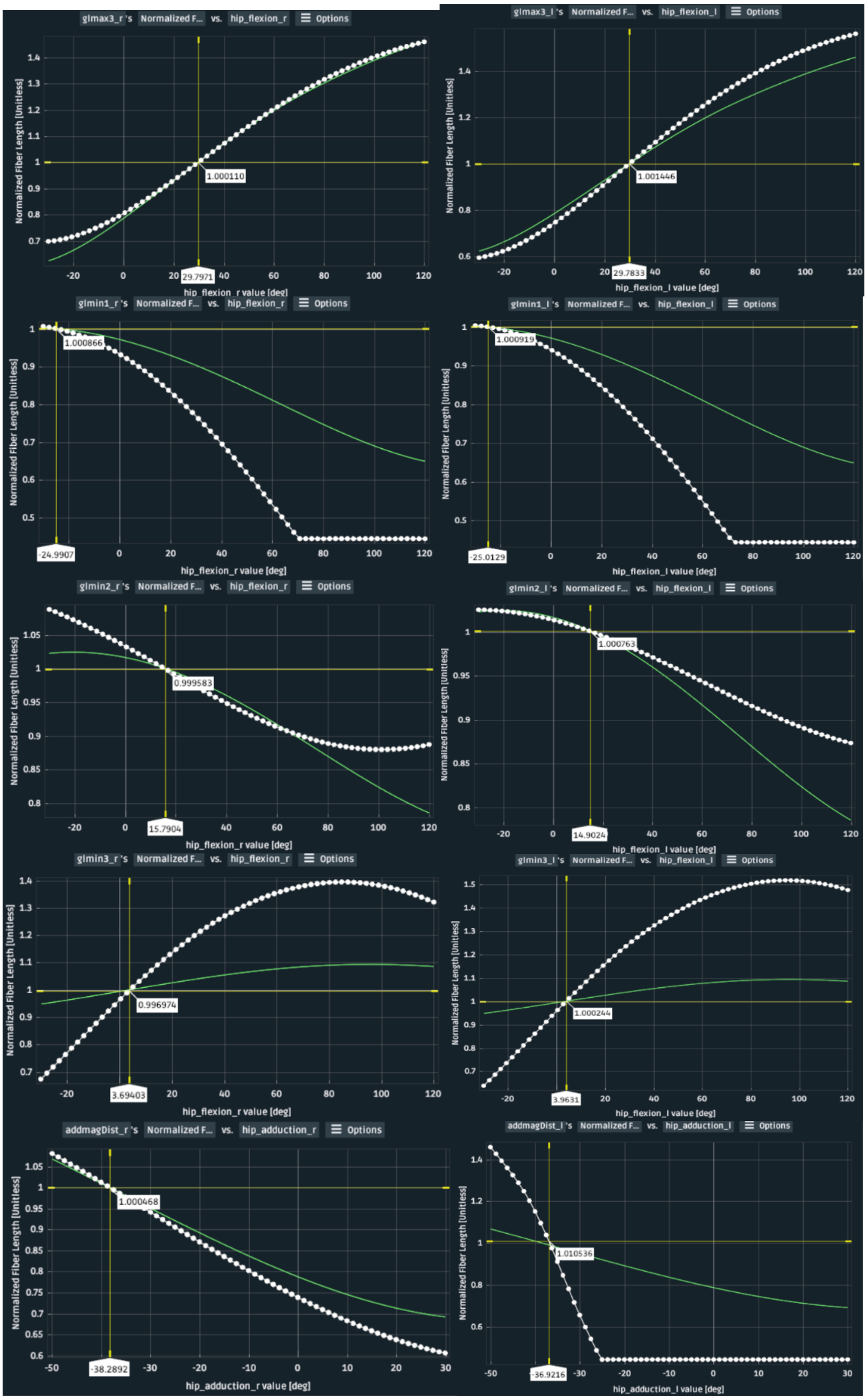
glmax3_r's Normalized F... vs. hip_flexion_r Options
Normalized Fiber Length [Unitless]
1.000110
29.7971
hip_flexion_r value [deg]
glmax3_l's Normalized F... vs. hip_flexion_l Options
1.001446
29.7833
hip_flexion_l value [deg]
glmin1_r's Normalized F... vs. hip_flexion_r Options
1.000866
-24.9907
hip_flexion_r value [deg]
glmin1_l's Normalized F... vs. hip_flexion_l Options
1.000919
-25.0129
hip_flexion_l value [deg]
glmin2_r's Normalized F... vs. hip_flexion_r Options
0.999583
15.7904
hip_flexion_r value [deg]
glmin2_l's Normalized F... vs. hip_flexion_l Options
1.000763
14.9024
hip_flexion_l value [deg]
glmin3_r's Normalized F... vs. hip_flexion_r Options
0.996974
3.69403
hip_flexion_r value [deg]
glmin3_l's Normalized F... vs. hip_flexion_l Options
1.000244
3.9631
hip_flexion_l value [deg]
addmagDist_r's Normalized F... vs. hip_adduction_r Options
1.000468
-38.2892
hip_adduction_r value [deg]
addmagDist_l's Normalized F... vs. hip_adduction_l Options
1.010536
-36.9216
hip_adduction_l value [deg]

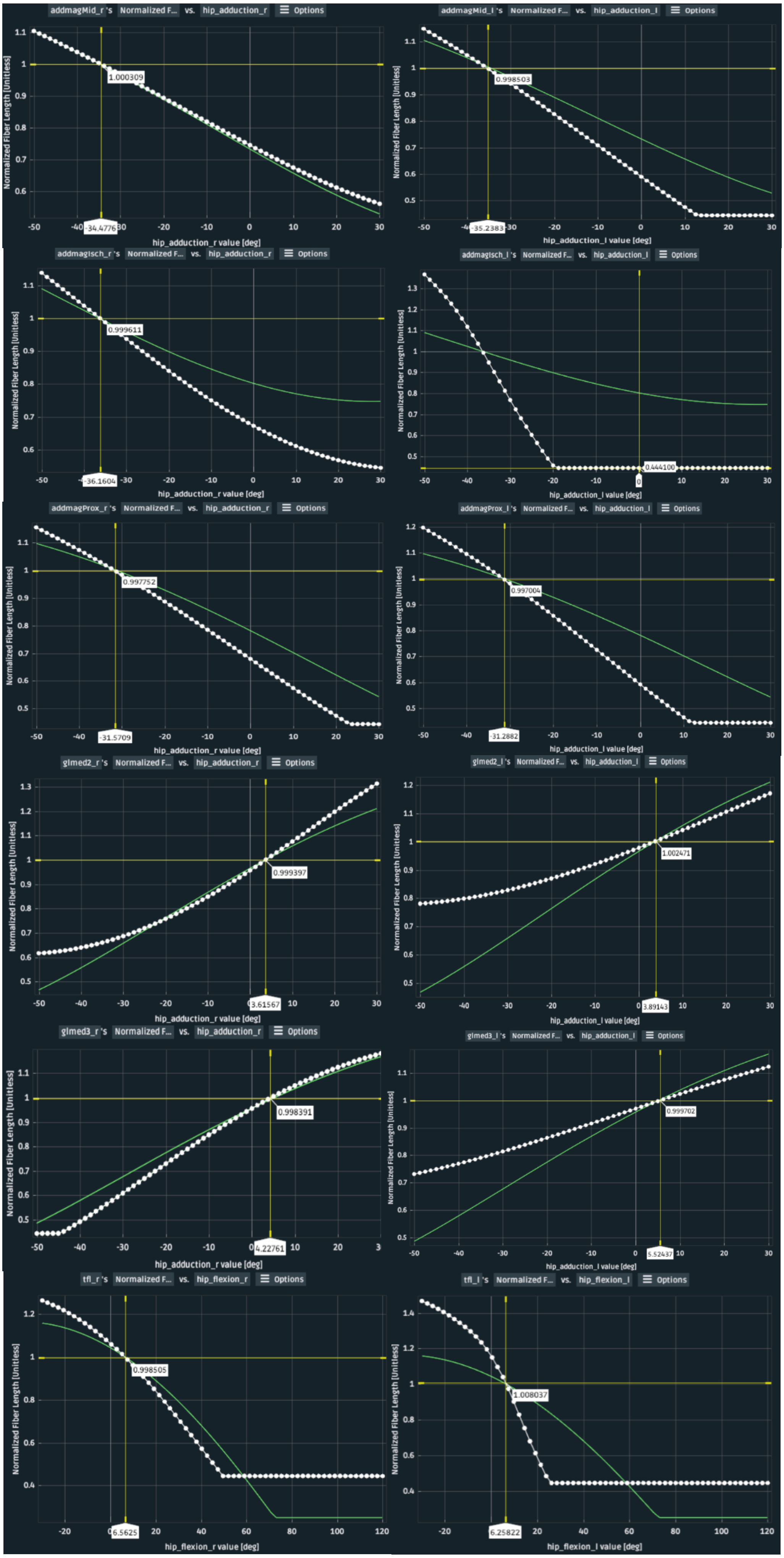
addmagMid_r's Normalized F... vs. hip_adduction_r Options
Normalized Fiber Length [Unitless]
1.000309
-34.4776
hip_adduction_r value [deg]
addmagMid_l's Normalized F... vs. hip_adduction_l Options
0.998503
-35.2383
hip_adduction_l value [deg]
addmagIsch_r's Normalized F... vs. hip_adduction_r Options
0.999611
-36.1604
addmagIsch_l's Normalized F... vs. hip_adduction_l Options
0.444100
addmagProx_r's Normalized F... vs. hip_adduction_r Options
0.997752
-31.5709
addmagProx_l's Normalized F... vs. hip_adduction_l Options
0.997004
-31.2882
glmed2_r's Normalized F... vs. hip_adduction_r Options
0.999397
3.61567
glmed2_l's Normalized F... vs. hip_adduction_l Options
1.002471
3.89143
glmed3_r's Normalized F... vs. hip_adduction_r Options
0.998391
4.22761
glmed3_l's Normalized F... vs. hip_adduction_l Options
0.999702
5.52437
tfl_r's Normalized F... vs. hip_flexion_r Options
0.998505
6.5625
hip_flexion_r value [deg]
tfl_l's Normalized F... vs. hip_flexion_l Options
1.008037
6.25822
hip_flexion_l value [deg]

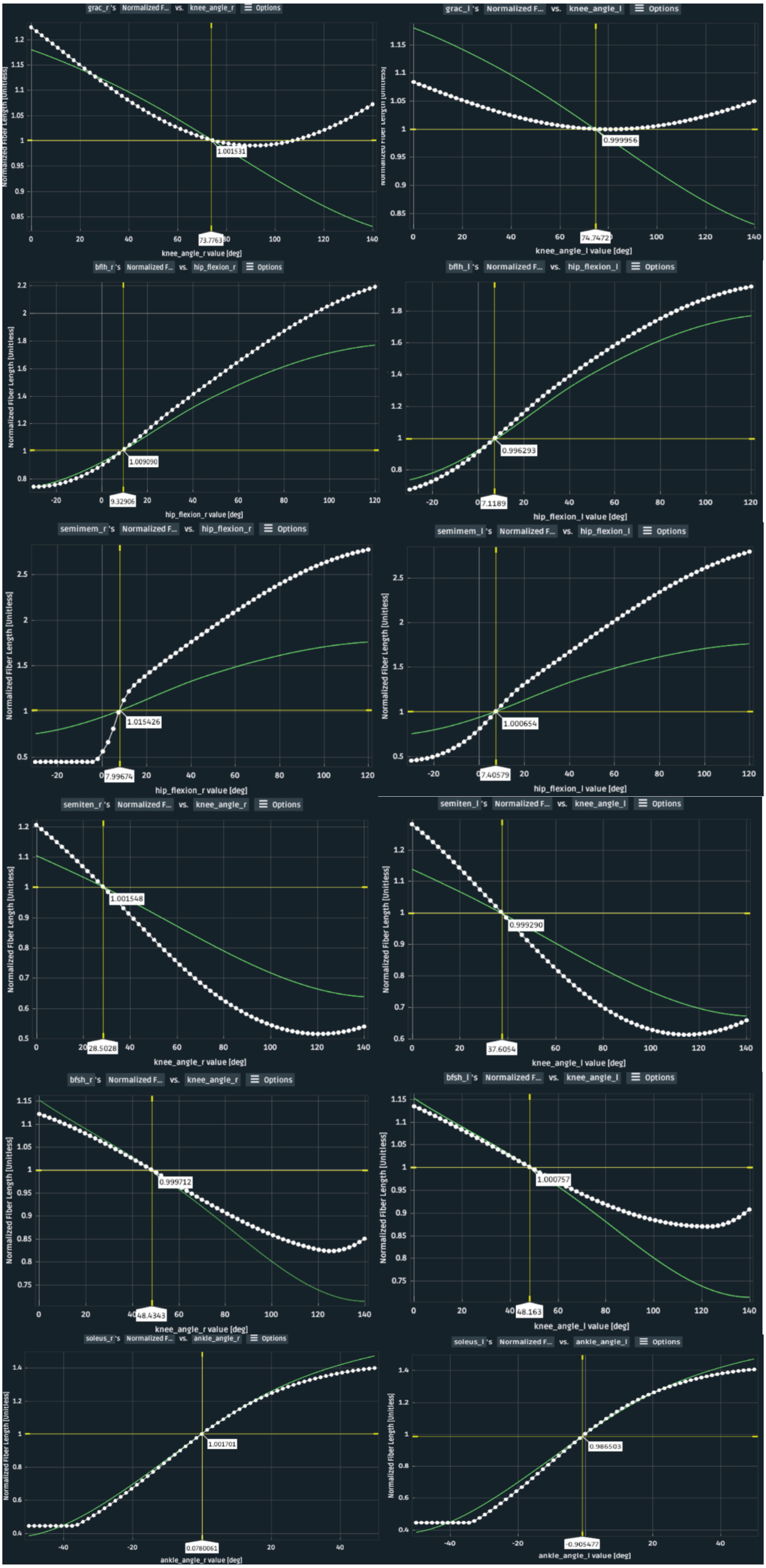
grac_r 's Normalized F... vs. knee_angle_r Options
Normalized Fiber Length [Unitless]
1.001531
73.77633
knee_angle_r value [deg]
grac_l 's Normalized F... vs. knee_angle_l Options
0.999956
74.7472
knee_angle_l value [deg]
bflh_r 's Normalized F... vs. hip_flexion_r Options
1.009090
9.32906
hip_flexion_r value [deg]
bflh_l 's Normalized F... vs. hip_flexion_l Options
0.996293
7.1189
hip_flexion_l value [deg]
semimem_r 's Normalized F... vs. hip_flexion_r Options
1.015426
7.99674
hip_flexion_r value [deg]
semimem_l 's Normalized F... vs. hip_flexion_l Options
1.000654
7.40579
hip_flexion_l value [deg]
semiten_r 's Normalized F... vs. knee_angle_r Options
1.001548
28.5028
knee_angle_r value [deg]
semiten_l 's Normalized F... vs. knee_angle_l Options
0.999290
37.6054
knee_angle_l value [deg]
bfsh_r 's Normalized F... vs. knee_angle_r Options
0.999712
48.4343
knee_angle_r value [deg]
bfsh_l 's Normalized F... vs. knee_angle_l Options
1.000757
48.163
knee_angle_l value [deg]
soleus_r 's Normalized F... vs. ankle_angle_r Options
1.001701
0.0780061
ankle_angle_r value [deg]
soleus_l 's Normalized F... vs. ankle_angle_l Options
0.986503
-0.905477
ankle_angle_l value [deg]

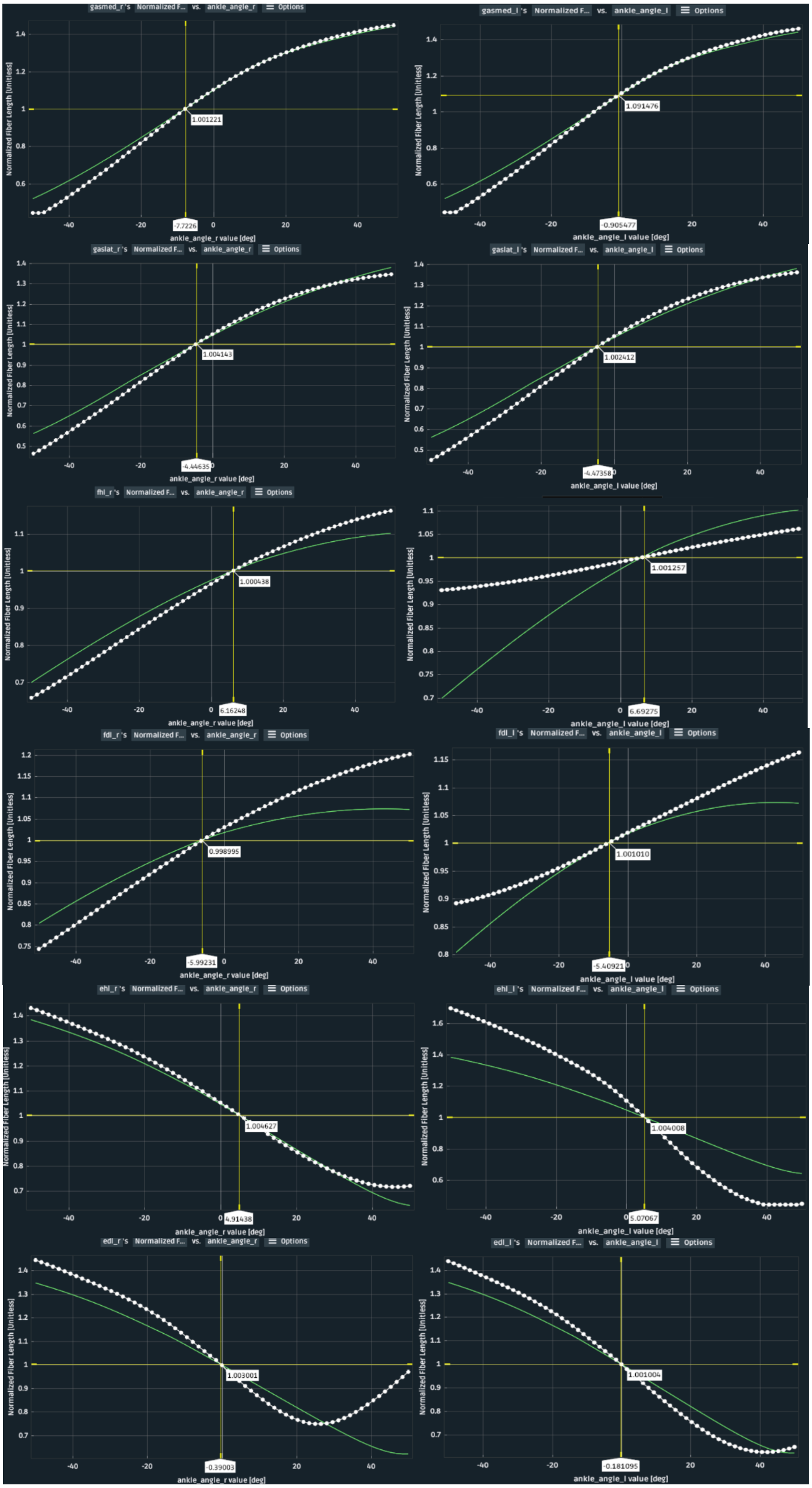
gasmed_r 's Normalized F... vs. ankle_angle_r Options
Normalized Fiber Length [Unitless]
1.001221
-7.7226
ankle_angle_r value [deg]
gasmed_l 's Normalized F... vs. ankle_angle_l Options
1.091476
-0.905477
ankle_angle_l value [deg]
gaslat_r 's Normalized F... vs. ankle_angle_r Options
1.004143
-4.44635
ankle_angle_r value [deg]
gaslat_l 's Normalized F... vs. ankle_angle_l Options
1.002412
-4.47358
ankle_angle_l value [deg]
fhl_r 's Normalized F... vs. ankle_angle_r Options
1.000438
6.16248
ankle_angle_r value [deg]
1.001257
6.69275
ankle_angle_l value [deg]
fdl_r 's Normalized F... vs. ankle_angle_r Options
0.998995
-5.99231
ankle_angle_r value [deg]
fdl_l 's Normalized F... vs. ankle_angle_l Options
1.001010
-5.40921
ankle_angle_l value [deg]
ehl_r 's Normalized F... vs. ankle_angle_r Options
1.004627
4.91438
ankle_angle_r value [deg]
ehl_l 's Normalized F... vs. ankle_angle_l Options
1.004008
5.07067
ankle_angle_l value [deg]
edl_r 's Normalized F... vs. ankle_angle_r Options
1.003001
-0.39003
ankle_angle_r value [deg]
edl_l 's Normalized F... vs. ankle_angle_l Options
1.001004
-0.181095
ankle_angle_l value [deg]

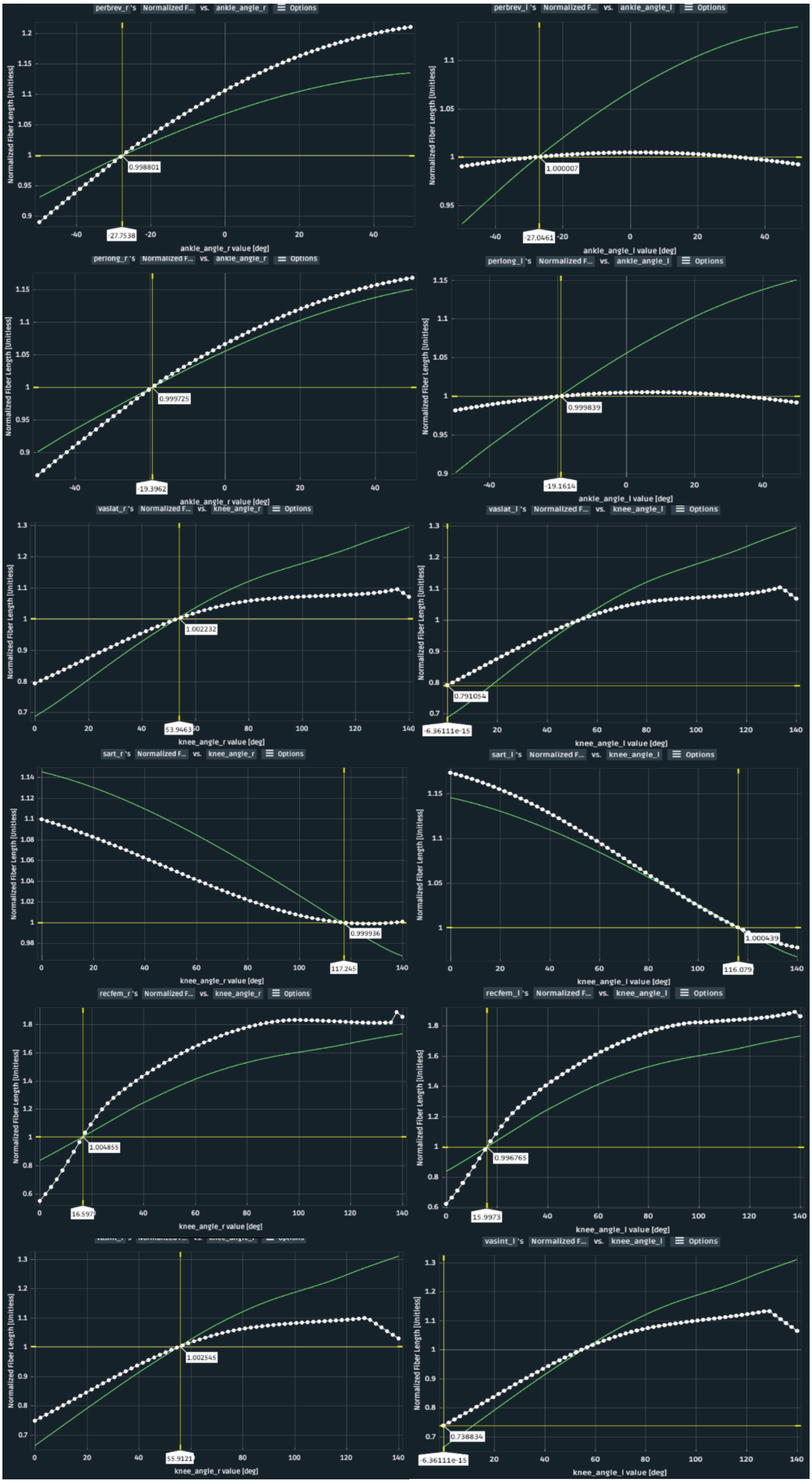

perbrev_r 's Normalized F... vs. ankle_angle_r Options
Normalized Fiber Length [Unitless]
0.998801
-27.7538
ankle_angle_r value [deg]
perbrev_l 's Normalized F... vs. ankle_angle_l Options
1.000007
-27.0461
ankle_angle_l value [deg]
perlong_r 's Normalized F... vs. ankle_angle_r Options
0.999725
-19.3962
perlong_l 's Normalized F... vs. ankle_angle_l Options
0.999839
-19.1614
vaslat_r 's Normalized F... vs. knee_angle_r Options
1.002232
53.9463
knee_angle_r value [deg]
vaslat_l 's Normalized F... vs. knee_angle_l Options
0.791054
-6.36111e-15
knee_angle_l value [deg]
sart_r 's Normalized F... vs. knee_angle_r Options
0.999936
117.245
sart_l 's Normalized F... vs. knee_angle_l Options
1.000439
116.079
recfem_r 's Normalized F... vs. knee_angle_r Options
1.004855
16.5977
recfem_l 's Normalized F... vs. knee_angle_l Options
0.996765
15.9973
vasint_l 's Normalized F... vs. knee_angle_l Options
1.002545
55.9121
0.738834
-6.36111e-15

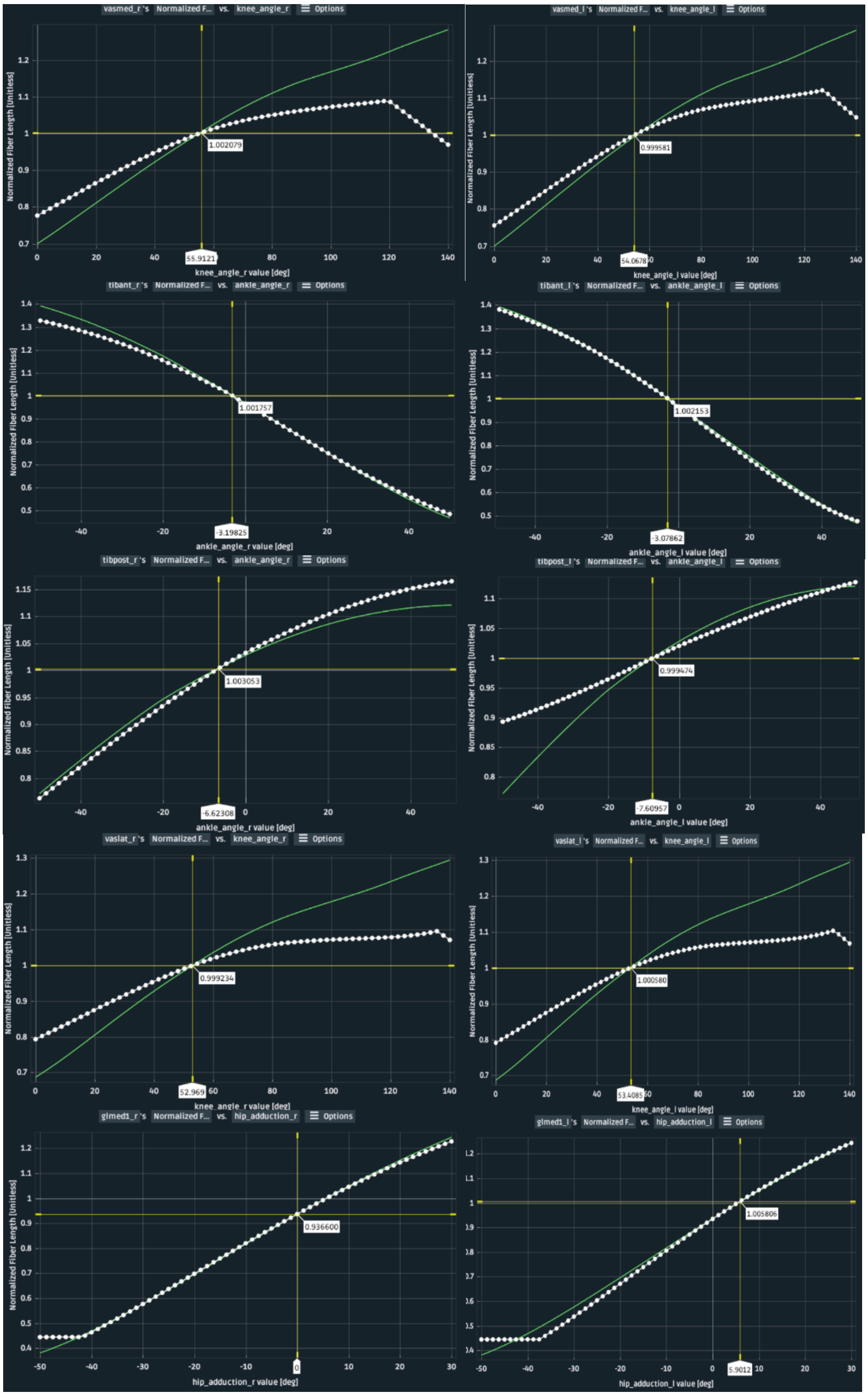
vasmed_r's Normalized F... vs. knee_angle_r Options
Normalized Fiber Length [Unitless]
1.002079
55.9121
knee_angle_r value [deg]
vasmed_l's Normalized F... vs. knee_angle_l Options
0.999581
54.0678
knee_angle_l value [deg]
tibant_r's Normalized F... vs. ankle_angle_r Options
1.001757
-3.19825
ankle_angle_r value [deg]
tibant_l's Normalized F... vs. ankle_angle_l Options
1.002153
-3.07862
ankle_angle_l value [deg]
tibpost_r's Normalized F... vs. ankle_angle_r Options
1.003053
-6.62308
ankle_angle_r value [deg]
tibpost_l's Normalized F... vs. ankle_angle_l Options
0.999474
-7.60957
ankle_angle_l value [deg]
vaslat_r's Normalized F... vs. knee_angle_r Options
0.999234
52.969
knee_angle_r value [deg]
vaslat_l's Normalized F... vs. knee_angle_l Options
1.000580
53.4085
knee_angle_l value [deg]
glmed1_r's Normalized F... vs. hip_adduction_r Options
0.936600
0
hip_adduction_r value [deg]
glmed1_l's Normalized F... vs. hip_adduction_l Options
1.005806
5.9012
hip_adduction_l value [deg]

Appendix G: Markers

Body	Name	Description
Pelvis	LASIS	Left anterior superior iliac spine
	RASIS	Right anterior superior iliac spine
	LPSIS	Left posterior superior iliac spine
	RPSIS	Right posterior superior iliac spine
Femur	LFT	Left femoral trochanter
	RFT	Right femoral trochanter
	LFME	Left femoral medial epicondyle
	LFLE	Left femoral lateral epicondyle
	RFME	Right femoral medial epicondyle
	RFLE	Right femoral lateral epicondyle
Tibia	LTT	Left tibial tuberosity
	LFH	Left fibula head
	RTT	Right tibial tuberosity
	RFH	Right fibula head
Foot	LFM1	Left foot metatarsal 1

LFM5	Left foot metatarsal 5
LC	Left calcaneus
RFM1	Right foot metatarsal 1
RFM5	Right foot metatarsal 5
RC	Right calcaneus

Appendix H: Results

Appendix H.1: Pelvis forces and moments analysis I

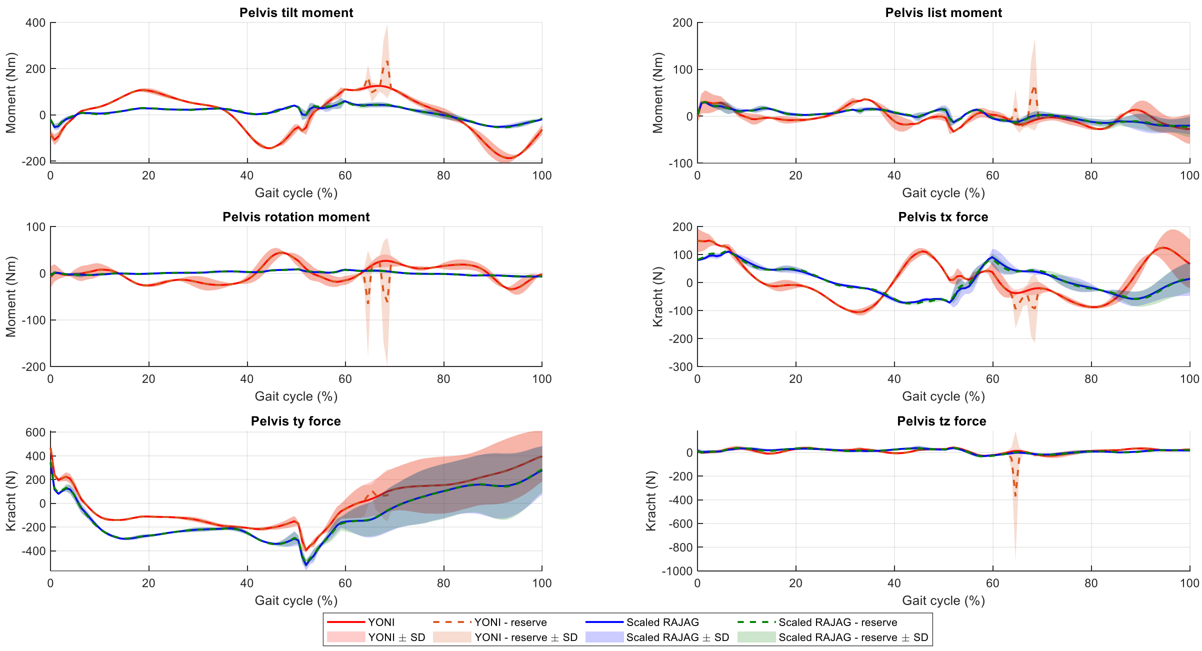

Appendix H.2: Pelvic forces and moments analysis II

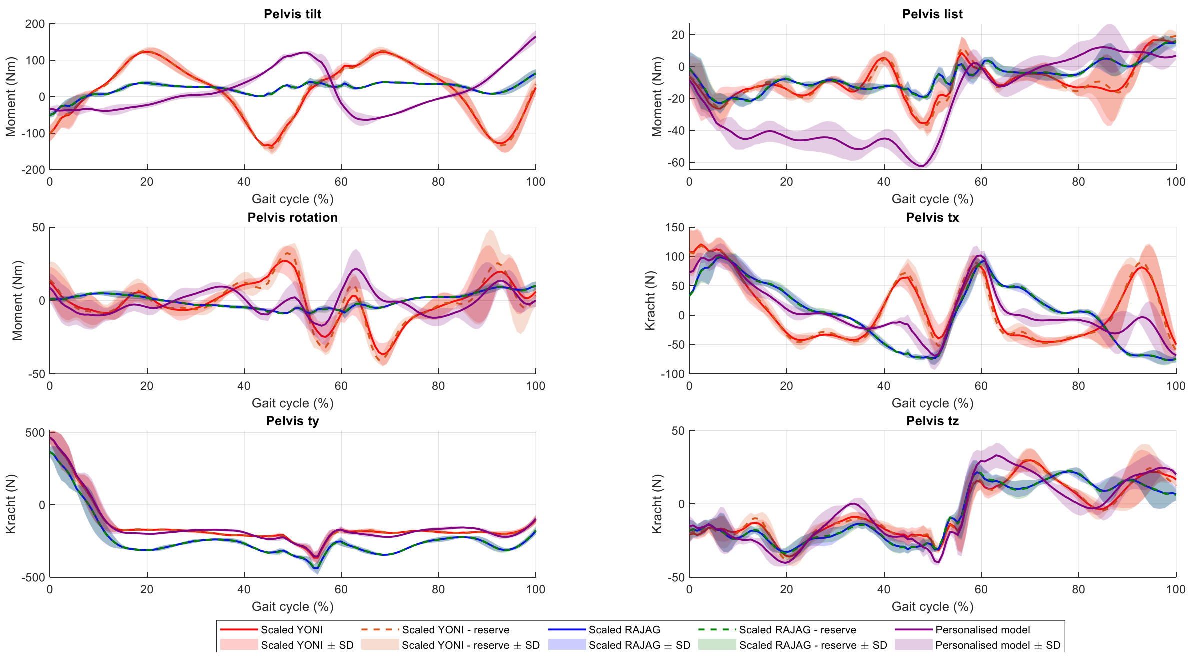

Appendix H.3: Muscle moment arms

Muscle moment arms knee flexion:

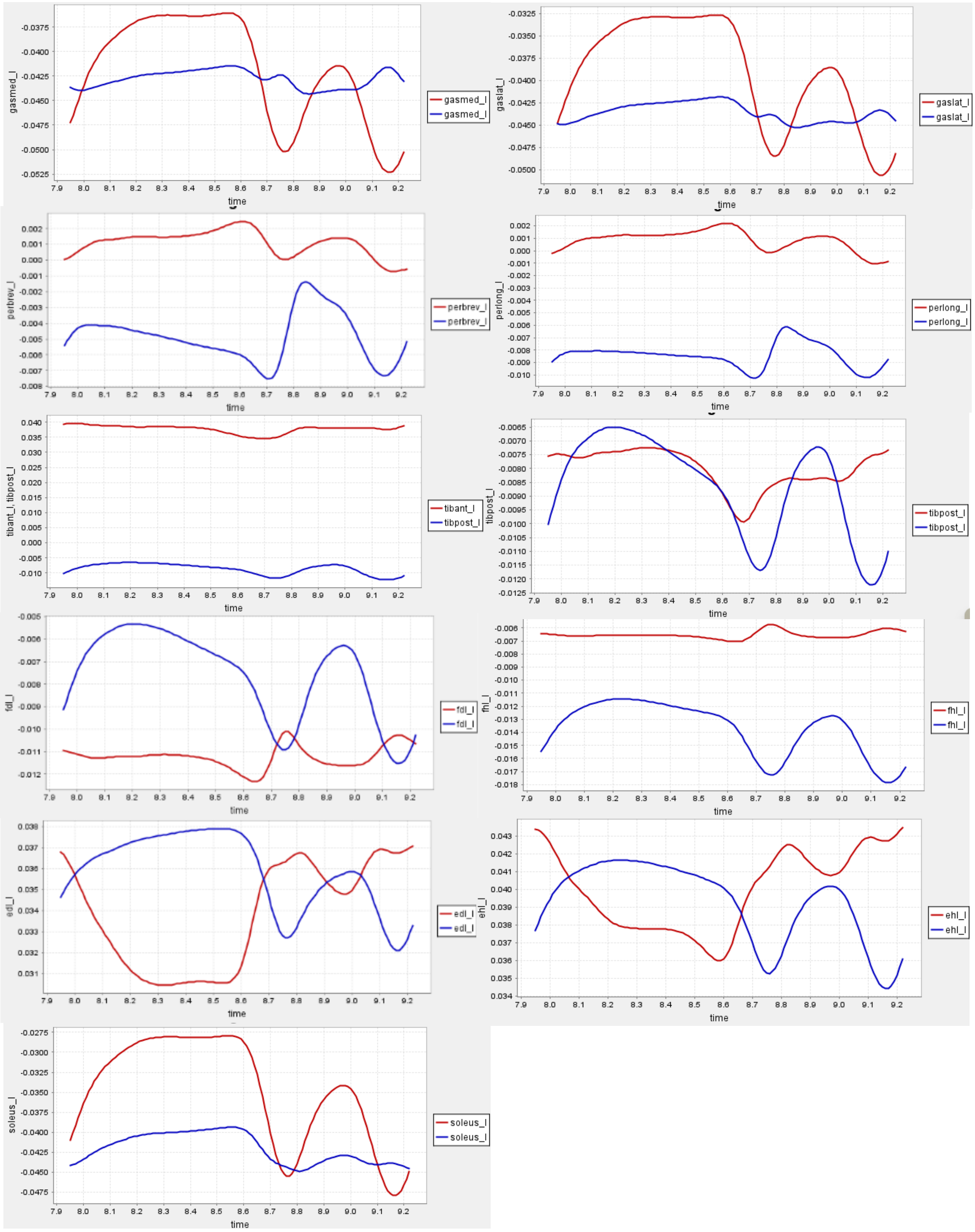

Red: scaled YONI model

Blue: scaled RAJAG model

Shown for 1 gait cycle, other gait cycles were similar.

Muscle moment arms knee flexion:

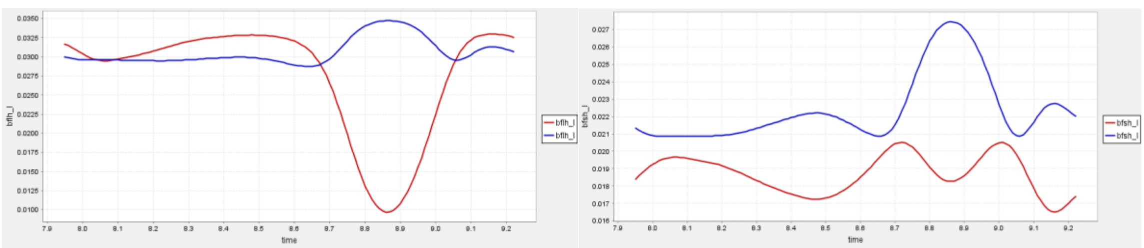

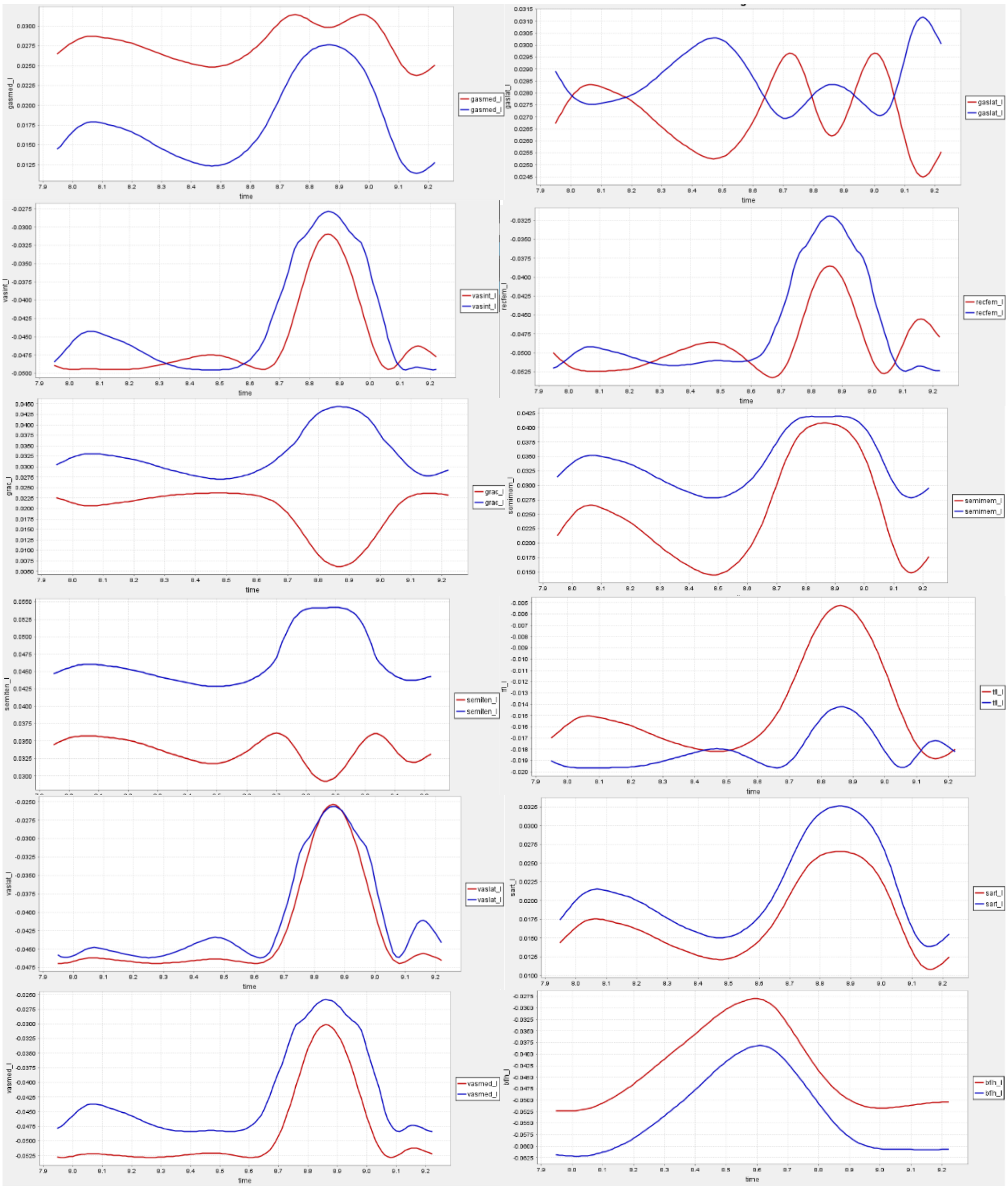

Muscle moment arm hip flexion:

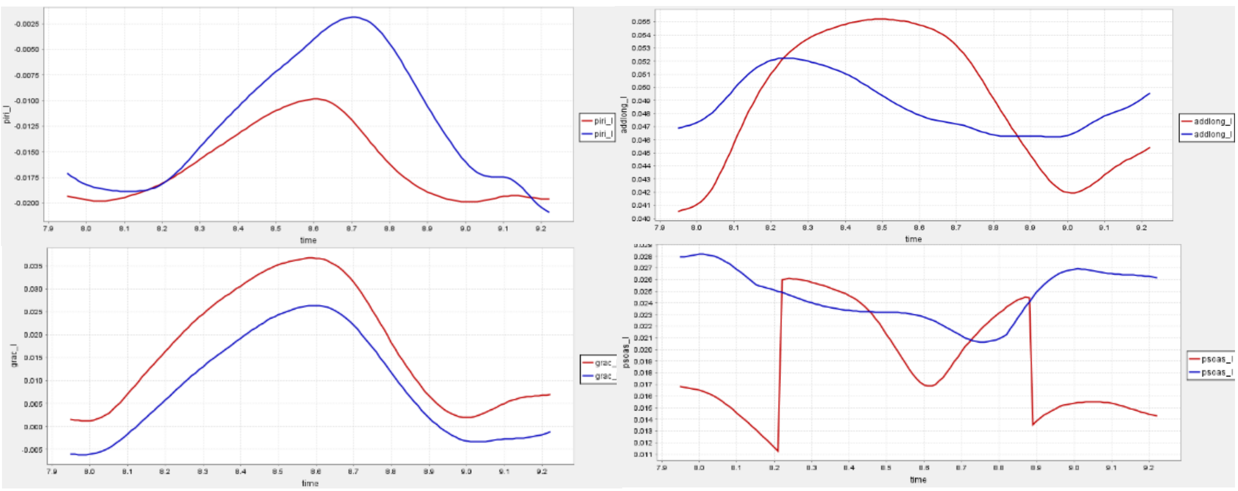

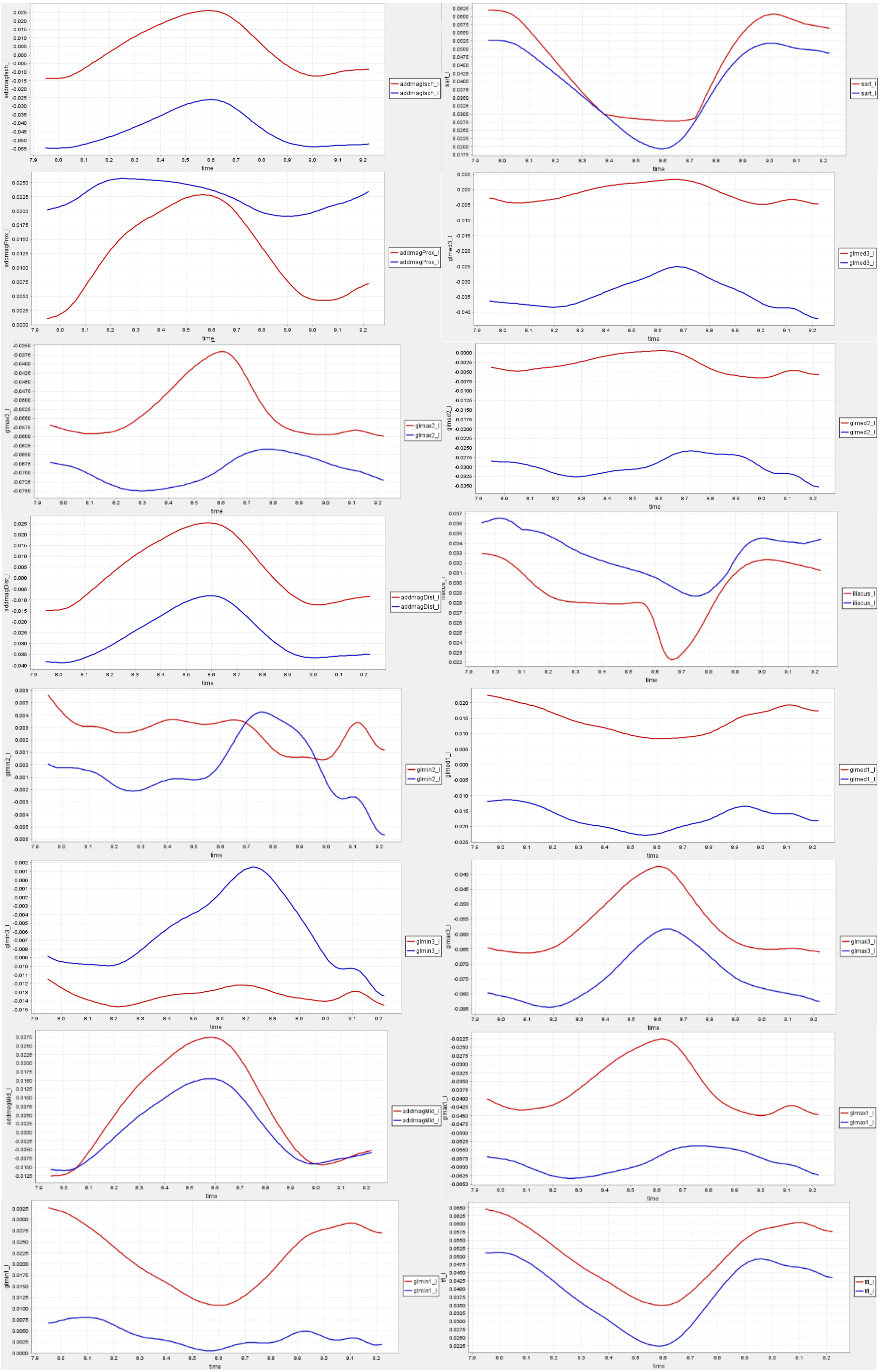
addmagIsch_l
sart_l
addmagProx_l
glmed3_l
glmax2_l
glmed2_l
addmagDist_l
iliacus_l
glmin2_l
glmed1_l
glmin3_l
glmax3_l
addmagMid_l
glmax1_l
glmin1_l
tfl_l
time

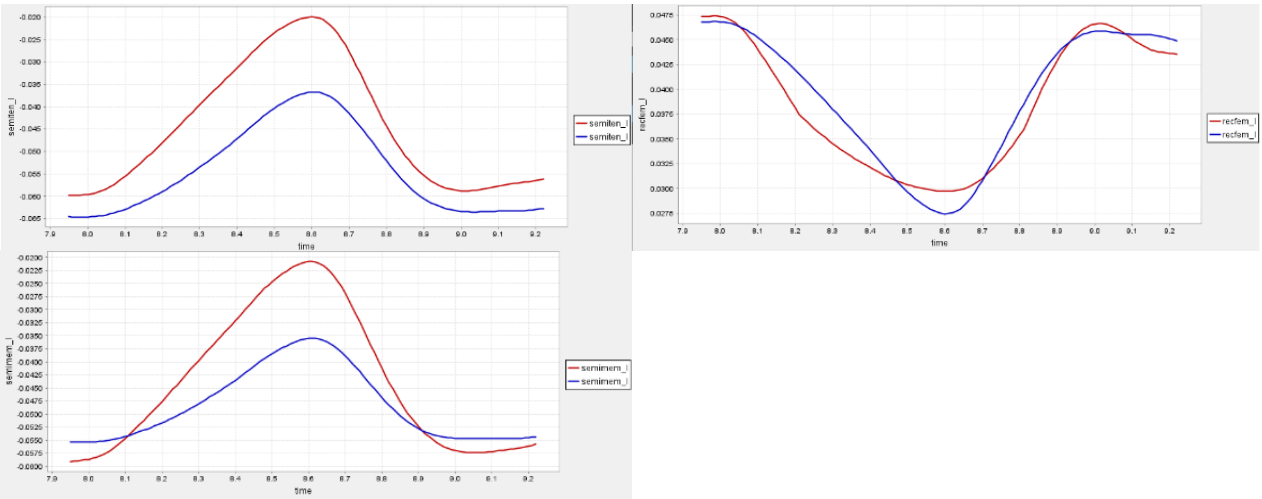

Muscle moment arms hip adduction:

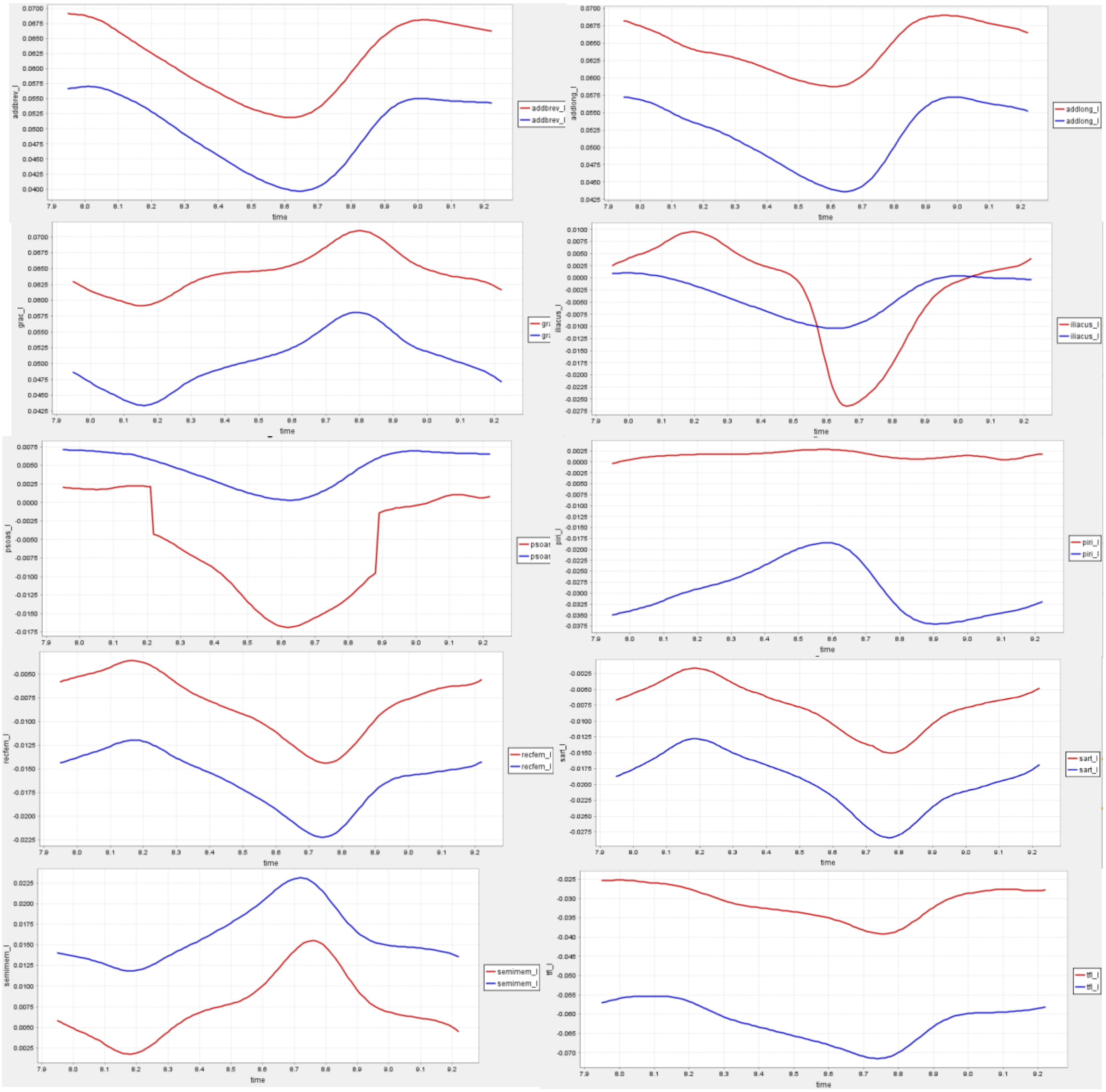

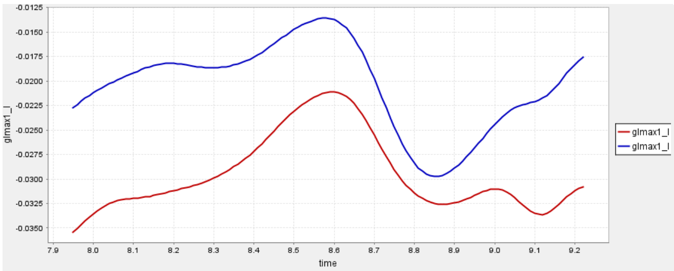
glmax1_l
time
glmax1_l
glmax1_l
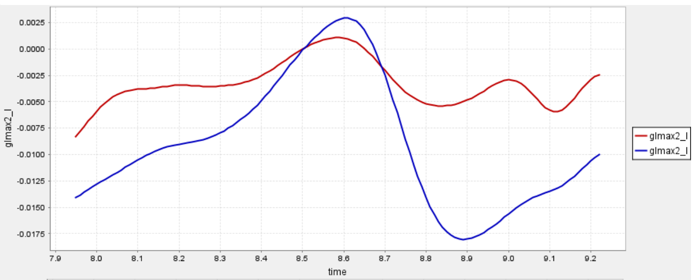
glmax2_l
time
glmax2_l
glmax2_l
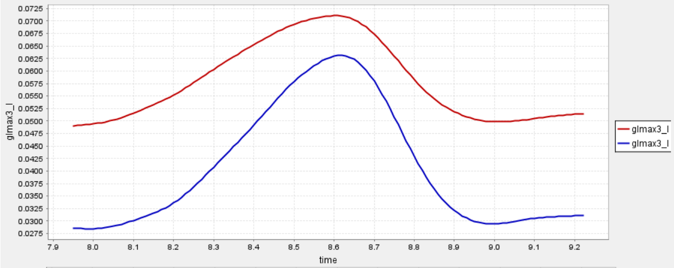
glmax3_l
time
glmax3_l
glmax3_l
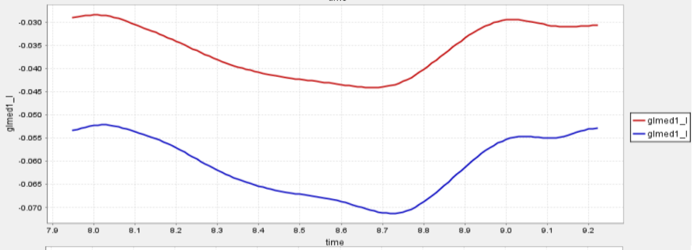
glmed1_l
time
glmed1_l
glmed1_l
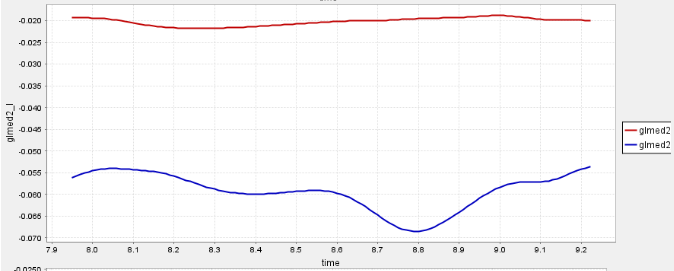
glmed2_l
time
glmed2
glmed2
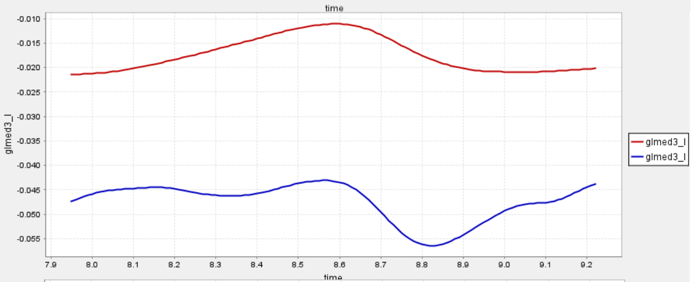
glmed3_l
glmed3_l
glmed3_l
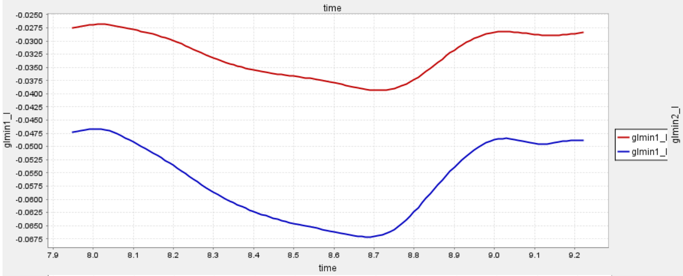
glmin1_l
time
glmin1_l
glmin1_l
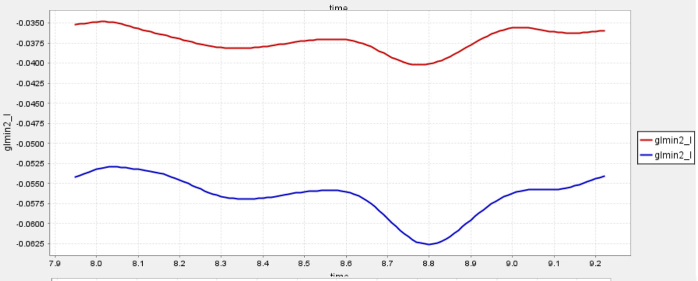
glmin2_l
glmin2_l
glmin2_l
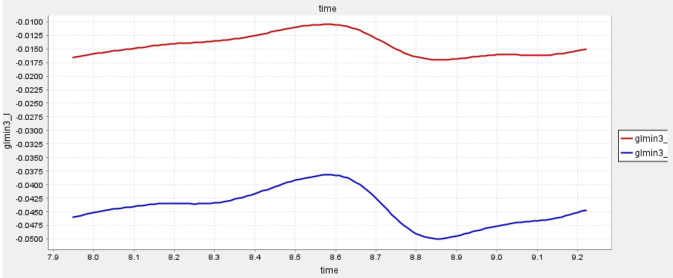
glmin3_l
time
glmin3_
glmin3_
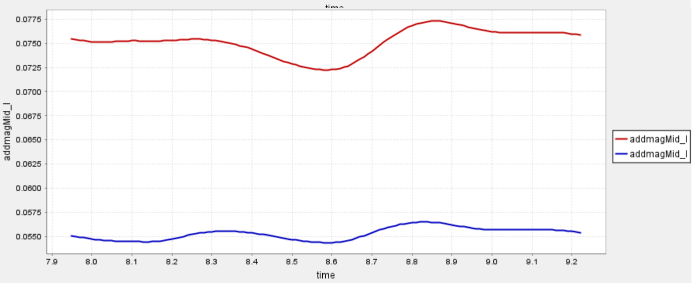
addmagMid_l
time
addmagMid_l
addmagMid_l
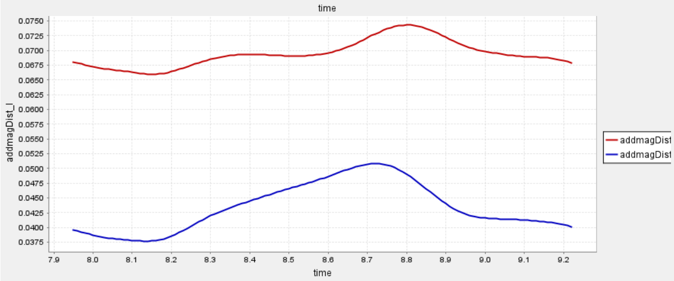
addmagDist_l
time
addmagDist
addmagDist
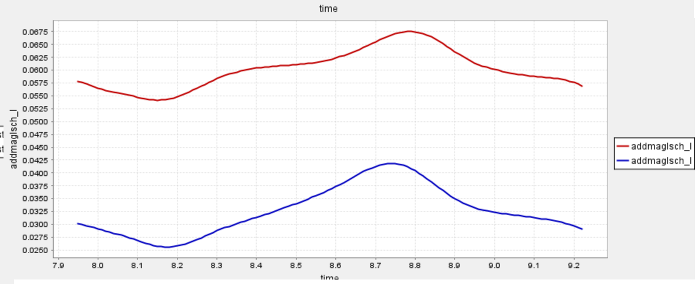
addmagIsch_l
addmagIsch_l
addmagIsch_l
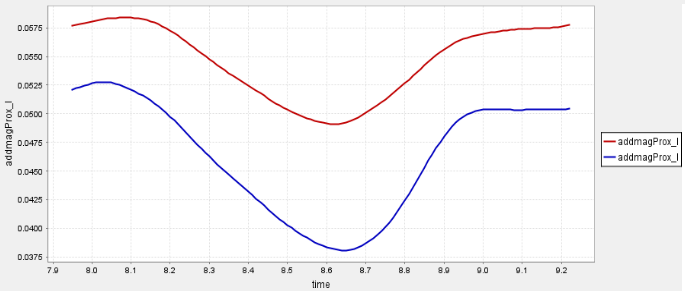
addmagProx_l
time
addmagProx_l
addmagProx_l

Muscle moment arms hip rotation:

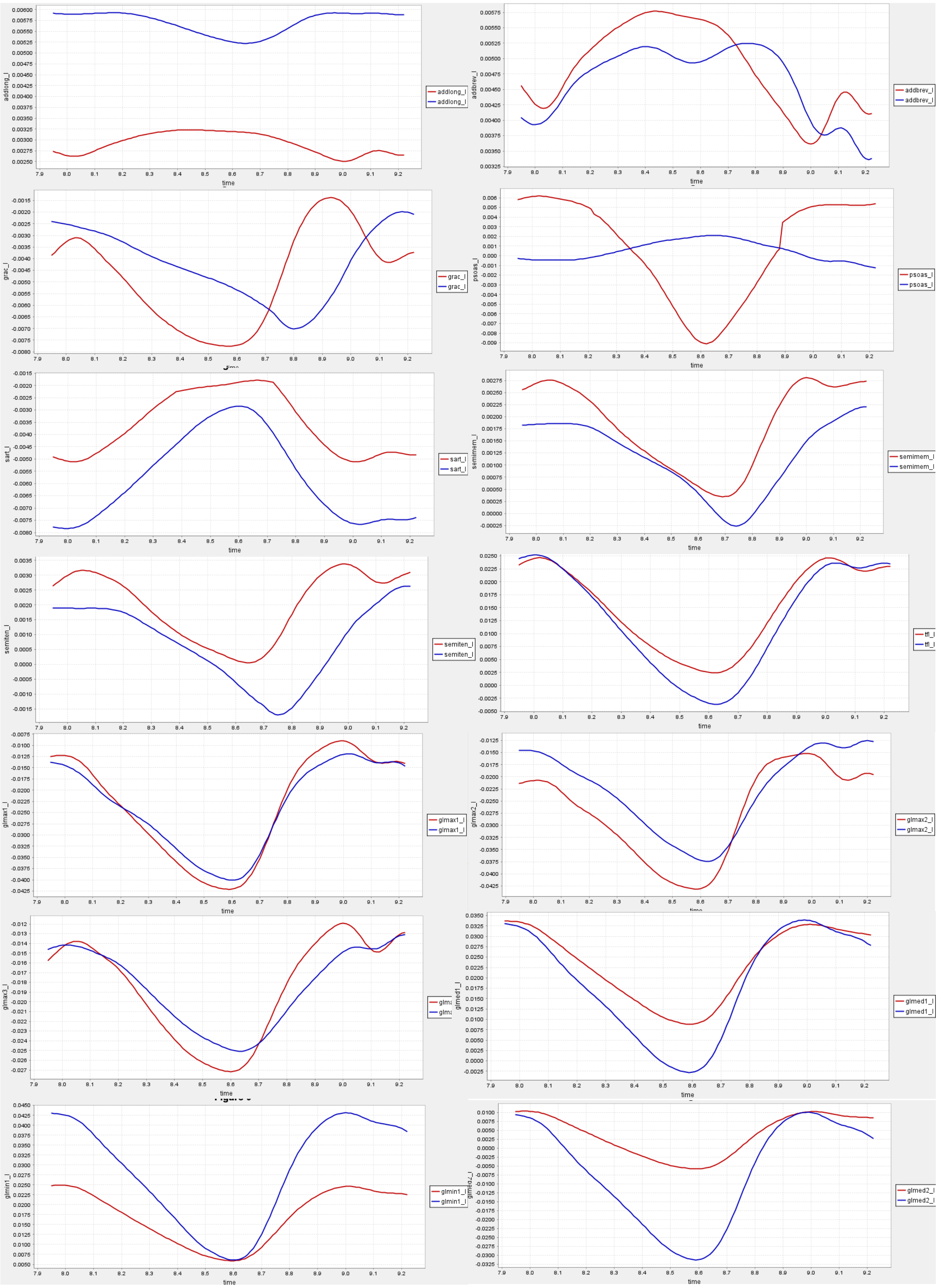

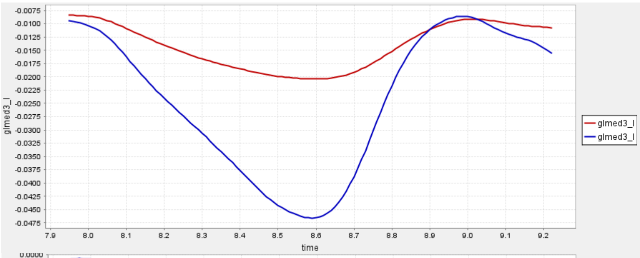
glmed3_l
glmed3_l
glmed3_l
time

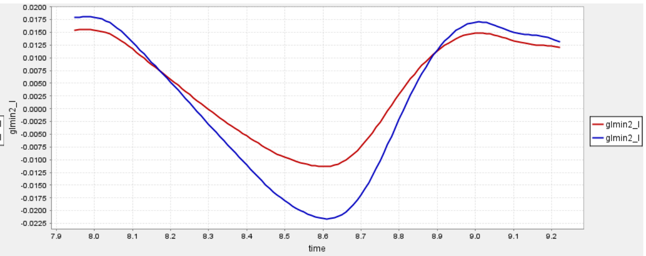
glmin2_l
glmin2_l
glmin2_l
time

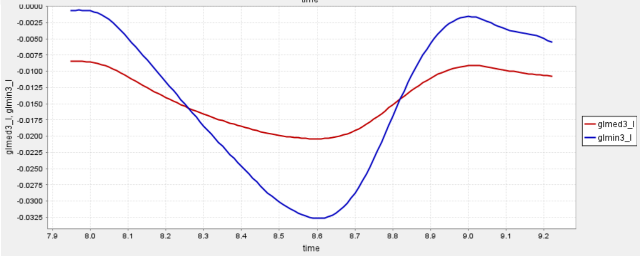
glmed3_l, glmin3_l
glmed3_l
glmin3_l
time

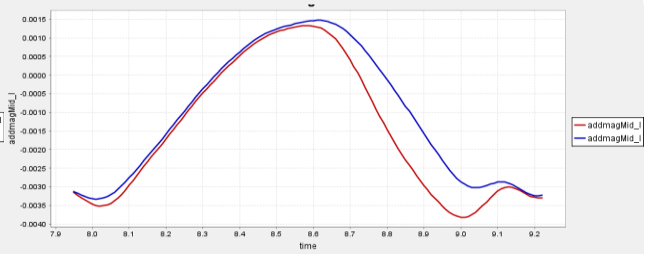
addmagMid_l
addmagMid_l
addmagMid_l
time

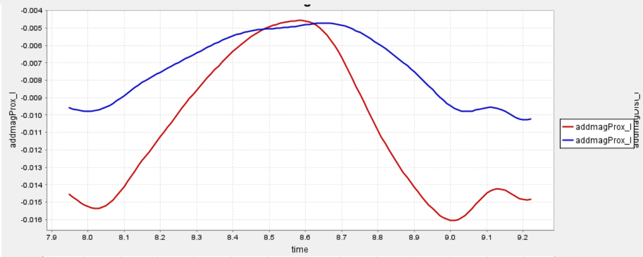
addmagProx_l
addmagProx_l
addmagProx_l
time

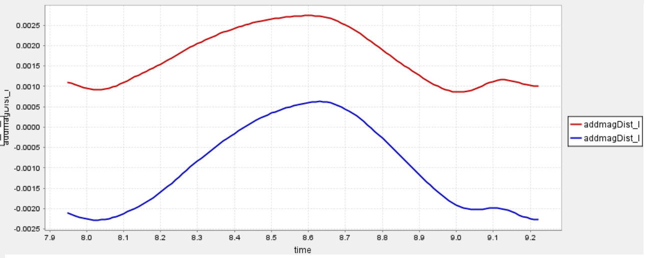
addmagDist_l
addmagDist_l
time

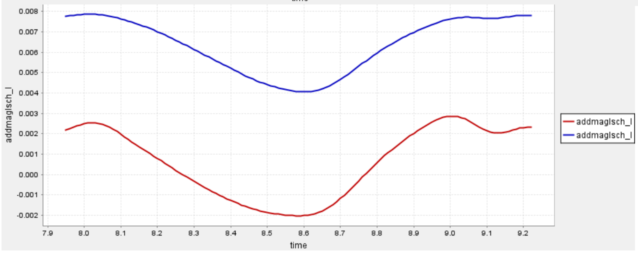
addmagIsch_l
addmagIsch_l
addmagIsch_l
time

Appendix G.4: Muscle forces

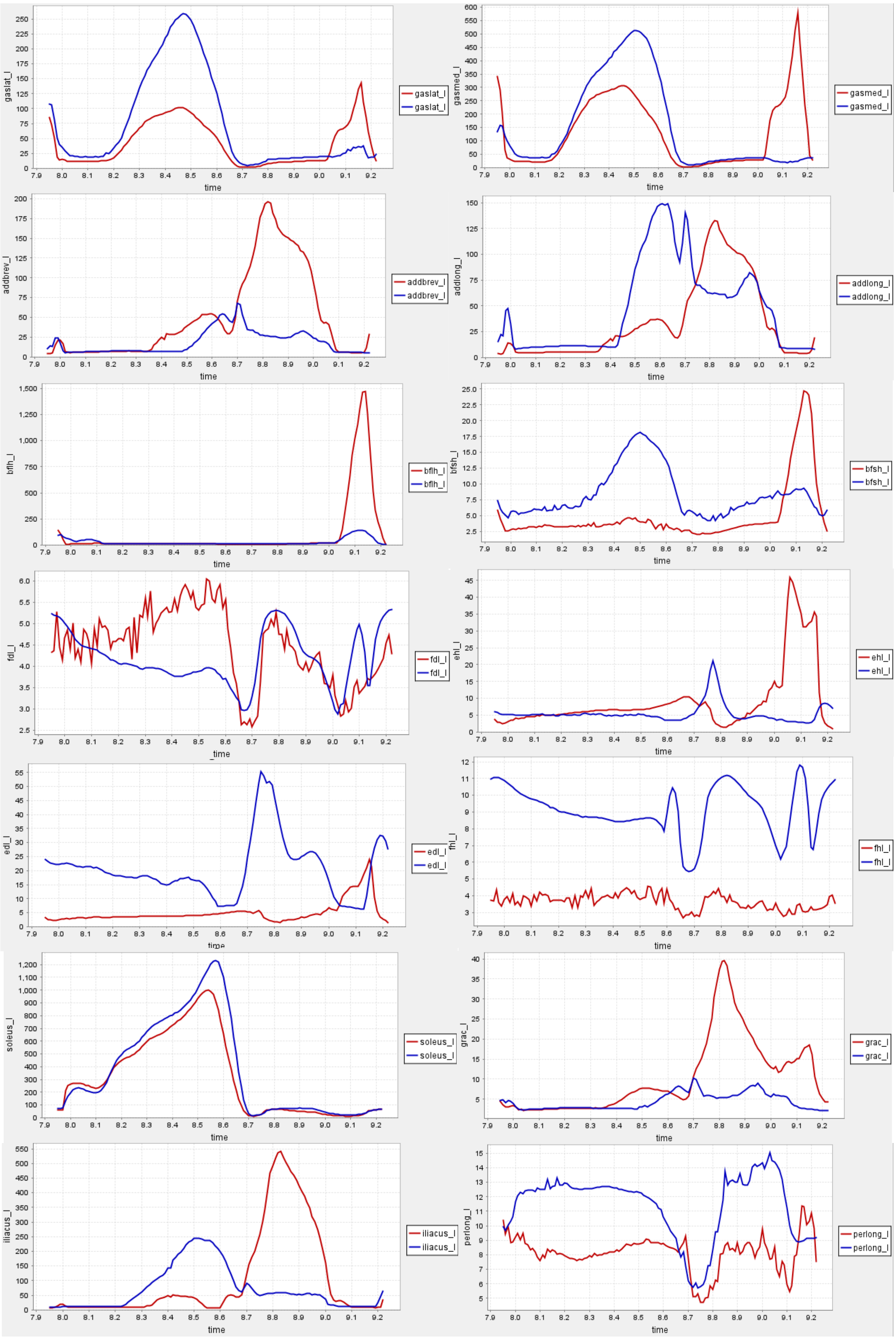

Red: scaled YONI model

Blue: scaled RAJAG model

Shown for 1 gait cycle, other gait cycles were similar.

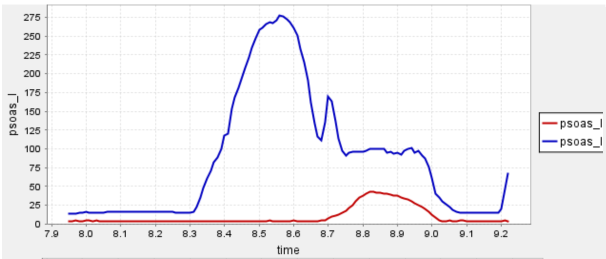
psoas_l
time
psoas_l
psoas_l

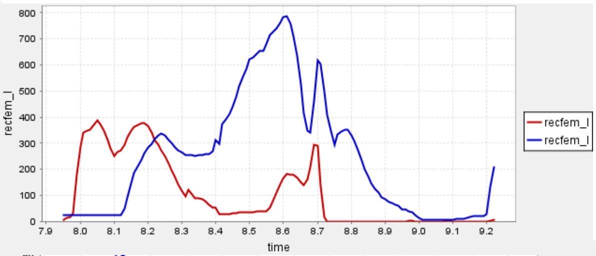
recfem_l
time
recfem_l
recfem_l

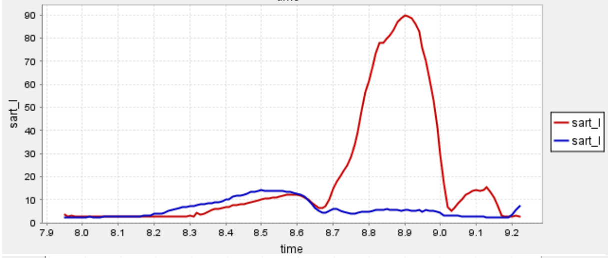
sart_l
time
sart_l
sart_l

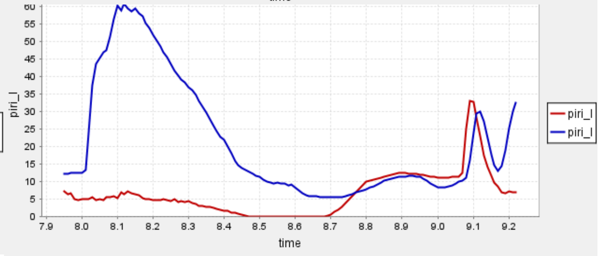
piri_l
time
piri_l
piri_l

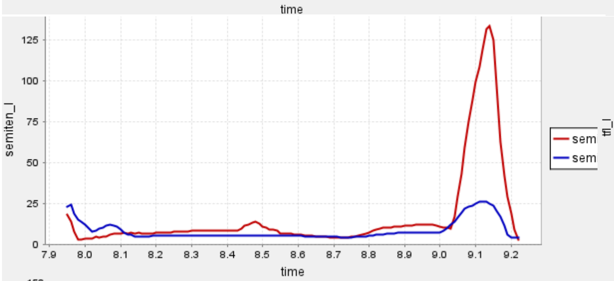
semiten_l
time
sem
sem

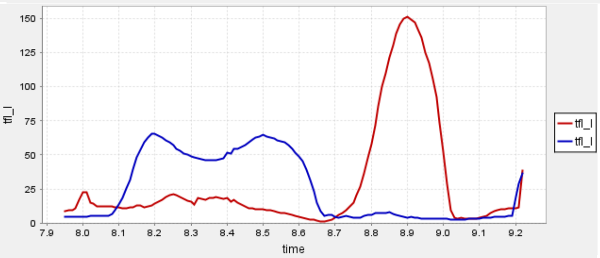
tfl_l
time
tfl_l
tfl_l

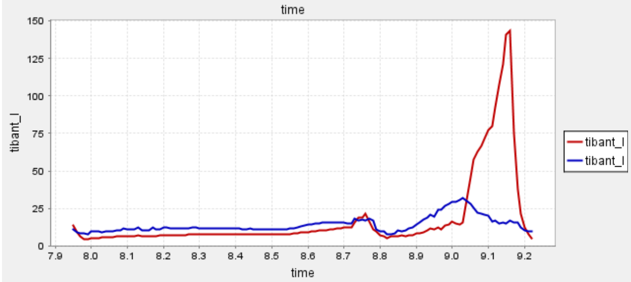
tibant_l
time
tibant_l
tibant_l

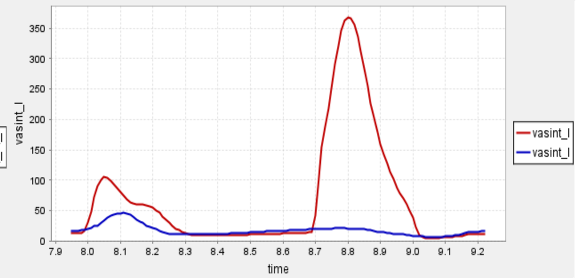
vasint_l
time
vasint_l
vasint_l

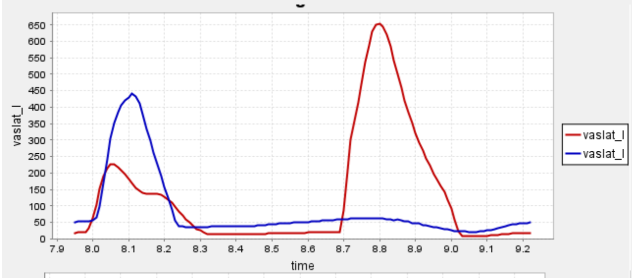
vaslat_l
time
vaslat_l
vaslat_l

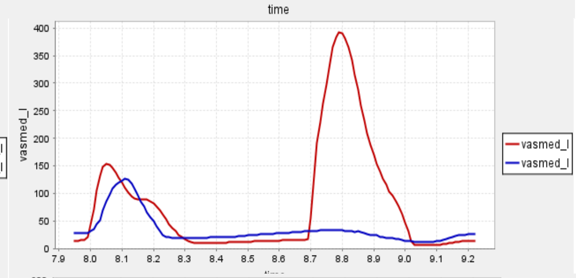
vasmed_l
vasmed_l
vasmed_l

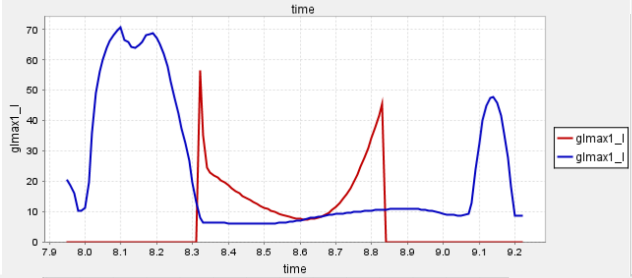
glmax1_l
time
glmax1_l
glmax1_l

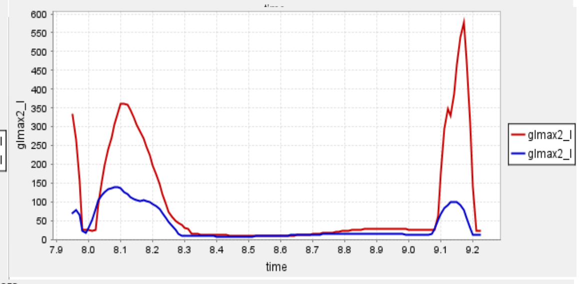
glmax2_l
time
glmax2_l
glmax2_l

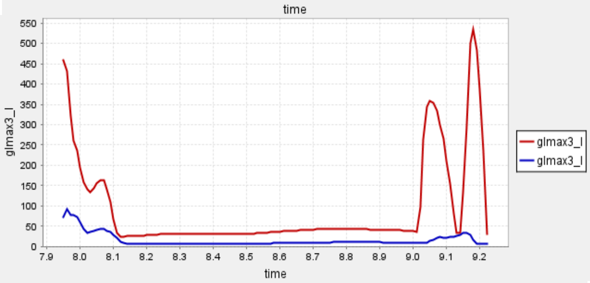
glmax3_l
time
glmax3_l
glmax3_l

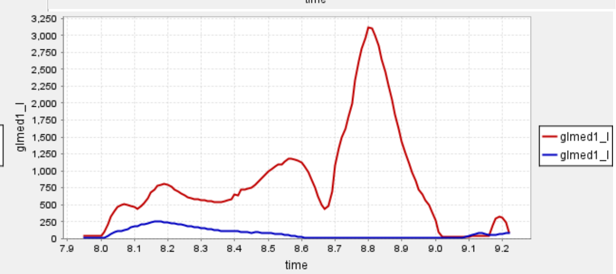
glmed1_l
time
glmed1_l
glmed1_l

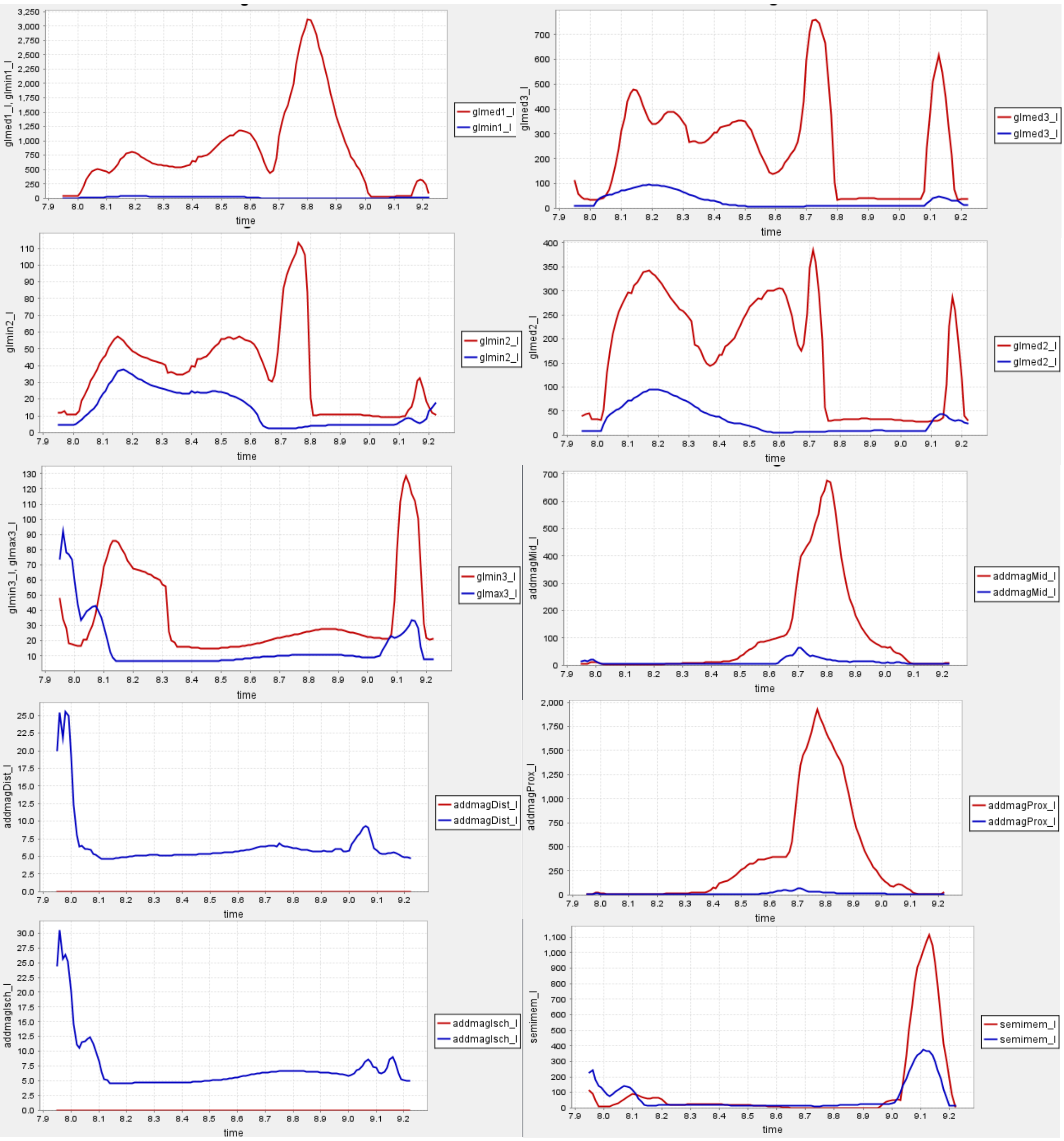
glmed1_l, glmin1_l
glmed1_l
glmin1_l
time
glmed3_l
glmed3_l
glmed3_l
time
glmin2_l
glmin2_l
glmin2_l
time
glmed2_l
glmed2_l
glmed2_l
time
glmin3_l, glmax3_l
glmin3_l
glmax3_l
time
addmagMid_l
addmagMid_l
addmagMid_l
time
addmagDist_l
addmagDist_l
addmagDist_l
time
addmagProx_l
addmagProx_l
addmagProx_l
time
addmagIsch_l
addmagIsch_l
addmagIsch_l
time
semimem_l
semimem_l
semimem_l
time